PONTIFICIA UNIVERSIDAD CATOLICA DE CHILE

SCHOOL OF ENGINEERING

MICROSTRUCTURAL STUDY OF MURINE LUNG PARENCHYMA MECHANICS THROUGH THE ANALYSIS OF THREE-DIMENSIONAL RECONSTRUCTIONS USING THE μ-CT TECHNIQUE.

MAURICIO ALEJANDRO SARABIA VALLEJOS

Thesis submitted to the Office of Graduate Studies in partial fulfillment of the requirements for the Degree of Doctor in Engineering Sciences

Advisor:

DANIEL HURTADO SEPÚLVEDA

Santiago de Chile, January, 2021

PONTIFICIA UNIVERSIDAD CATOLICA DE CHILE

SCHOOL OF ENGINEERING

MICROSTRUCTURAL STUDY OF MURINE LUNG PARENCHYMA MECHANICS THROUGH THE ANALYSIS OF THREE-DIMENSIONAL RECONSTRUCTIONS USING THE μ-CT TECHNIQUE

MAURICIO ALEJANDRO SARABIA VALLEJOS

Members of the Committee:

DANIEL HURTADO DocuSigned by: Daniel Hurtado S. 4AD1C27AD1BB4B6...

DIEGO CELENTANO DocuSigned by: Diego Javier Celentano 91CFB35EC4C442F...

CLAUDIO GARCÍA DocuSigned by: Claudio García H. 86DEF7D92749413...

PABLO CRUCES DocuSigned by: Pablo Cruces Romero FC2C85366D91471...

MONA ESKANDARI DocuSigned by: Mona Eskandari 81CA5E4B1DE74B8...

GUSTAVO LAGOS DocuSigned by: Gustavo Lagos C. B558E6FD3B4641F...

Thesis submitted to the Office Graduate Studies in partial fulfillment of the requirements for the Degree of Doctor in Engineering Sciences

Santiago of Chile, January, 2021

ACKNOWLEDGMENTS

First of all, I would like to thank my family, and especially my wife Carmen Gonzalez, who has been with me all this time, supporting me, not only from a sentimental point of view but also as an academic specialist in the chemical area. I would also like to thank the arrival of our baby, Mauricio Alonso, who has brought us enormous happiness to our lives, despite the difficult times that we have had to live this year 2020.

Similarly, I would like to thank my advisor, Daniel Hurtado, who taught me everything about the topics covered in this thesis and has also been motivated me continuously during these 5 years in developing this thesis. Besides, I would like to acknowledge the entire Computational Medicine group CB2L conformed by Agustin Perez, Agustin Cox, Javiera Jilberto, Felipe Alvarez, Roberto Leon, Carlos Andrade, William Ramirez, David Ortiz, Felipe Concha, Benjamin Villa, Patricio Zavala, Pablo Zurita, Francisco Sahli, and Rodrigo Quezada. Thanks to the Institute of Biological and Medical Engineering (IIBM) group who have accompanied me these last years.

Finally, I would like to acknowledge the PUC's financial support through the scholarships that were awarded to me, in addition to the financial support provided by ANID through the scholarship “Estudios de Doctorado Nacional 2015” N° 21150221, and the supplementary scholarships “Gastos Operacionales 2019” and “Asistencia a Congresos Internacionales 2018” and to the financial support provided by the project FONDECYT Regular N° 1180832, led by Prof. Daniel Hurtado.

LIST OF PAPERS

This thesis is based on the following papers, referred in the text by respective chapters:

Chapter I: Concha F., **Sarabia-Vallejos M.**, Hurtado D.E. (2018) **Micromechanical model of lung parenchyma hyperelasticity**. *Journal of the Mechanics and Physics of Solids*, 112, 126-144.

Chapter II: **Sarabia-Vallejos M.A.**, Zuñiga M., Hurtado D.E. (2019) **The role of three-dimensionality and alveolar pressure in the distribution and amplification of alveolar stresses**. *Scientific Reports*, 9, 8783(1-11).

Chapter III: **Sarabia-Vallejos M.A.**, Ayala-Jeria P., Hurtado D.E. (2020) **Three-dimensional characterization of the regional alveolar morphology in normal lungs**. *Submitted to Acta Biomaterialia*.

Chapter IV: Villa B., **Sarabia-Vallejos M.A.**, Hurtado D.E. (2021) **Implications of collagen and elastin fibers digestion and their effect in the mechanical properties of lung tissue strips.**
Manuscript under preparation.

Besides, during the development of this doctoral thesis, I also contributed to the following published articles:

Cruces P., Erranz B., Lillo F., **Sarabia-Vallejos M.A.**, Iturrieta P., Morales F., Blaha K., Medina T., Diaz F., Hurtado D.E. (2019) **Mapping regional strain in anesthetized healthy subjects during spontaneous ventilation**. *BMJ Open Respiratory Research*, 6, e000423(1-8).

Hurtado D.E., Erranz B., Lillo F., **Sarabia-Vallejos M.**, Iturrieta P., Morales F., Blaha K., Medina T., Diaz F., Cruces P. (2020) **Progression of regional lung strain and heterogeneity in lung injury: Assessing the evolution under spontaneous breathing and mechanical ventilation**. *Annals of Intensive Care*, 10, 107(1-10).

PROCEEDINGS

Parts of this work have also been presented at international congresses under the following references:

Mauricio A. Sarabia-Vallejos, Matias Zuñiga, Daniel E. Hurtado.
Alveolar stress distributions in realistic lung parenchyma geometries obtained from μ-CT.
In: *8th World Congress of Biomechanics* (WCB 2018)
Dublin, Ireland.
July 2018 **(Poster Presentation).**

Mauricio A. Sarabia-Vallejos, Matias Zuñiga, Daniel E. Hurtado.
Stress distributions in real alveolar geometries obtained from μ-ct. How does affect the consideration of three-dimensionality?
In: 6th International Conference on Computational and Mathematical Biomedical Engineering (CMBE 2019).
Sendai, Japan.
June 2019 **(Oral Presentation).**

Mauricio A. Sarabia-Vallejos, Matias Zuñiga, Daniel E. Hurtado.
On the 3D stress distribution in the alveolar walls: A combined μ-CT and computational modeling study.
In: 16th International symposium on computer methods in biomechanics and biomedical engineering and the 4th Conference on imaging and visualization (CMBBE 2019).
New York, USA.
August 2019 **(Poster Presentation).**

FIGURE INDEX

TABLE INDEX

ABBREVIATION INDEX

NIH: National Institute of Health

COPD: Chronic Obstructive Pulmonary Diseases

p-V: Pressure-Volume

FRC: Functional Residual Capacity

TLC: Total Lung Capacity

SEM: Scanning Electron Microscopy

ARDS: Acute Respiratory Distress Syndrome

μ-CT or micro-CT: Micro Computed Tomography

PCLS: Precision-Cut Lung Slices

AFM: Atomic Force Microscopy

ECM: Extracellular Matrix

FE: Finite Element

DECT: Dual-Energy Computed Tomography

EILV: End-Inspiratory Lung Volume

synCT: Synchrotron-Based μ-CT

RVE: Representative Volume Element

TKD: Tetrakaidekahedron

AS: Alveolar Sacs

AD: Alveolar Ducts

VS: Blood Vessels

C: Capillaries

DOFs: Degrees of Freedom

DNS: Direct Numerical Simulation

LAP: Low Alveolar Pressure

HAP: High Alveolar Pressure

$p_{tp:}$ Transpulmonary Pressure

$p_{alv:}$ Alveolar Pressure

AVMA: American Veterinary Medical Association

F-PBS: Formalin Phosphate-Buffered-Saline

A_{tissue}: Area of Tissue

p_{tissue}: Pressure of Tissue

A_{air}: Area of Air

A_{alv}: Alveolar Surface Area

$V_{airspace}$: Volume of Alveolar Airspace

V_{ref}: Reference Volume

ρ: Surface-to-volume Ratio

η: Alveolar Surface Area Density

ϕ: Porosity

SAF: Standard Alcohol Fixation

MAF: Modified Alcohol Fixation

HMDS: Hexamethyldisilazane

ROI: Regions of Interest

HBSS: Hank's Balanced Salt Solution

LIST OF CONTENT

ABSTRACT

PONTIFICIA UNIVERSIDAD CATOLICA DE CHILE
SCHOOL OF ENGINEERING

MICROSTRUCTURAL STUDY OF MURINE LUNG PARENCHYMA MECHANICS THROUGH THE ANALYSIS OF THREE-DIMENSIONAL RECONSTRUCTIONS USING THE μ-CT TECHNIQUE

Thesis submitted to the Office of Graduate Studies in partial fulfillment of the requirements for the Degree of Doctor in Engineering Sciences by

MAURICIO ALEJANDRO SARABIA VALLEJOS

The study of the three-dimensional architecture of the lung parenchyma is a very relevant and exciting topic intended to comprehend and characterize its morphology and understand the close relationship between microarchitecture and the physiological function in the lung parenchyma. However, advances in this area have been restricted due to the small dimensions of the basic structural units of the lung parenchyma, and also due to its extreme fragility, which makes it challenging to handle and to imaging with reasonable and fair spatial resolution. Conveniently, in recent years there has been continuous progress in the development of biomedical imaging technologies. The computerized microtomography (μ-CT) technique stands out, allowing high-resolution tomographic images of small biological tissue sectors in a non-invasive way.

This thesis analyzes several of the utilities and benefits of these three-dimensional images compared to traditional two-dimensional images of lung tissue (histology, confocal microscopy, or scanning electron microscopy, among others). For example, in Chapter II, we report the analysis of small sectors of lung tissue's mechanical behavior using real

representations of the alveolar microstructure of healthy mice. Using these data, we were able to verify that the stress to which the alveolar tissue is subjected in some localized sectors is more than 27 times the initial pressure, which tells us that the microarchitecture of the alveolar tissue has a profound effect on the mechanical behavior of the tissue. We were also able to verify that since the lung parenchyma is a complex three-dimensional tissue that handles stresses in all directions, it is incorrect to analyze its mechanical behavior using two-dimensional representations. This process can lead to significant overestimations of alveolar tissue strains and stresses.

In addition, we present a new tool that allows us to analyze certain key parameters of alveolar morphology by generating a three-dimensional mapping. For this, we took as a basis μ-CT images of the lung parenchyma, and through the application of a series of filters, masks, and morphological image processing, it was possible to generate voxel-to-voxel data of these geometric parameters. With this data, we could assemble a continuous three-dimensional map of some specific characteristics of the lung, in this case, we calculate the porosity, the density of the alveolar surface area of the tissue, and the surface-volume ratio of the lung parenchyma.

Members of the Doctoral Thesis Committee:

Daniel Hurtado
Diego Javier
Claudio García
Pablo Cruces
Mona Eskandari
Gustavo Lagos

Santiago, January, 2021

RESUMEN

PONTIFICIA UNIVERSIDAD CATOLICA DE CHILE
ESCUELA DE INGENIERIA

ESTUDIO MICROESTRUCTURAL DE LA MECÁNICA DEL PARÉNQUIMA PULMONAR MURINO A TRAVÉS DEL ANÁLISIS DE RECONSTRUCCIONES TRIDIMENSIONALES USANDO LA TÉCNICA DE μ-CT.

Tesis enviada a la Dirección de Postgrado en cumplimiento parcial de los requisitos para el grado de Doctor en Ciencias de la Ingeniería.

MAURICIO ALEJANDRO SARABIA VALLEJOS

El estudio de la arquitectura tridimensional del parénquima pulmonar es un tema muy relevante y emocionante destinado a comprender y caracterizar su morfología y comprender la estrecha relación entre la microarquitectura y la función fisiológica en el parénquima pulmonar. Sin embargo, los avances en esta área se han visto restringidos debido a las pequeñas dimensiones de las unidades estructurales básicas del parénquima pulmonar, y también debido a su extrema fragilidad, lo que dificulta su manejo y obtención de imágenes con una resolución espacial razonable y justa. Convenientemente, en los últimos años ha habido un progreso continuo en el desarrollo de tecnologías de imágenes biomédicas. Destaca la técnica de microtomografía computarizada (μ-CT), que permite obtener imágenes tomográficas de alta resolución de pequeños sectores de tejido biológico de forma no invasiva.

Esta tesis analiza varias de las utilidades y beneficios de estas imágenes tridimensionales frente a las tradicionales imágenes bidimensionales de tejido pulmonar (histología, microscopía confocal o microscopía electrónica de barrido, entre otras). Por ejemplo, en el Capítulo II, presentamos el análisis de pequeños sectores del comportamiento mecánico del

tejido pulmonar utilizando representaciones reales de la microestructura alveolar de ratones sanos. Con estos datos pudimos comprobar que el estrés al que está sometido el tejido alveolar en algunos sectores localizados es más de 27 veces superior a la presión inicial, lo que nos dice que la microarquitectura del tejido alveolar tiene un profundo efecto sobre el comportamiento mecánico del tejido. También pudimos comprobar que, dado que el parénquima pulmonar es un tejido tridimensional complejo que maneja tensiones en todas las direcciones, es incorrecto analizar su comportamiento mecánico utilizando representaciones bidimensionales. Este proceso puede dar lugar a sobreestimaciones importantes de las tensiones y tensiones del tejido alveolar.

Además, presentamos una nueva herramienta que nos permite analizar ciertos parámetros clave de la morfología alveolar mediante la generación de un mapeo tridimensional. Para ello, tomamos como base imágenes μ-CT del parénquima pulmonar, y mediante la aplicación de una serie de filtros, máscaras y procesamiento de imágenes morfológicas, fue posible generar datos voxel a voxel de estos parámetros geométricos. Con estos datos, podríamos armar un mapa tridimensional continuo de algunas características específicas del pulmón, en este caso calculamos la porosidad, la densidad de la superficie alveolar del tejido y la relación superficie-volumen del pulmón. parénquima.

Miembros de la Comisión de Tesis Doctoral:

Daniel Hurtado
Diego Javier
Claudio García
Pablo Cruces
Mona Eskandari
Gustavo Lagos

Santiago, Enero, 2021

1. INTRODUCTION

1.1 Motivation

Bronchopulmonary diseases correspond to the second cause of death worldwide (NIH & NHLBI, 2012). According to the NIH (National Institute of Health), 8.9% of all deaths caused by medical reasons are related to bronchopulmonary disorders. Within this disease group, there are several conditions, the most common being the Chronic Obstructive Pulmonary Diseases (COPD, 57.5%), including pulmonary emphysema. These numbers are incredibly worrying since the lungs correspond to the respiratory system's main organ and are fundamental in the human body's oxygenation process.

To further understand the functional consequences that these pathologies can generate, in this thesis, we analyze both from theoretical and experimental perspectives the effect that the lung parenchyma's microarchitecture has on the lung global mechanical behavior during normal breathing cycles. Accordingly, in the following sections, we discuss the mechanical implication that the alveolar geometry of some basic anatomical structures of the lung parenchyma imposes on the whole organ's mechanical response, together with some micromechanical multiscale models for the lung tissue. Finally, novel technological methods to imaging the lung microarchitecture are also presented, and some anatomical or geometrical imaging analysis should improve the lung micromechanical characterization.

1.2 Lung macro and microstructure

The respiratory system is mainly conformed by three types of tissue: muscular tissue (diaphragm and intercostal muscles), conductive tissue (primary and secondary airways), and the lung parenchyma. The airways constitute a fantastic and complex branching tree designed to transport air to the alveoli efficiently. The parenchyma corresponds to the lung's functional tissue, where the gas exchange with blood occurs (terminal bronchioles, acini, alveolar sacs, and alveoli) (Jardins, 2008). In Figure 1-1 (left, extracted from (Ethier & Simmons, 2007)), a resin model of the human airways is depicted. In the image, the trachea (T) divides into two smaller conducts, the bronchi (B), which are, in turn, divided into

bronchioles. If this process is repeated 16 times (in the case of humans), the terminal bronchioles, which are the smallest structures that form the conductive tissue, are reached. From this point onwards (branches from 17 to 23), the so-called transitional and respiratory zones are founded. These zones are formed by the respiratory bronchioles, acini, alveolar ducts, and alveolar sacs. This sector corresponds to almost 90% of the whole-lung volume (2.5 - 3 liters) (Ewald R. Weibel, 2017). Here is where the gas exchange with the bloodstream is carried out through an intricate vascular network surrounding the alveolar sacs. In Figure 1-1 (right, extracted from (Ethier & Simmons, 2007)), it is possible to observe a respiratory airways schematic description of its distribution.

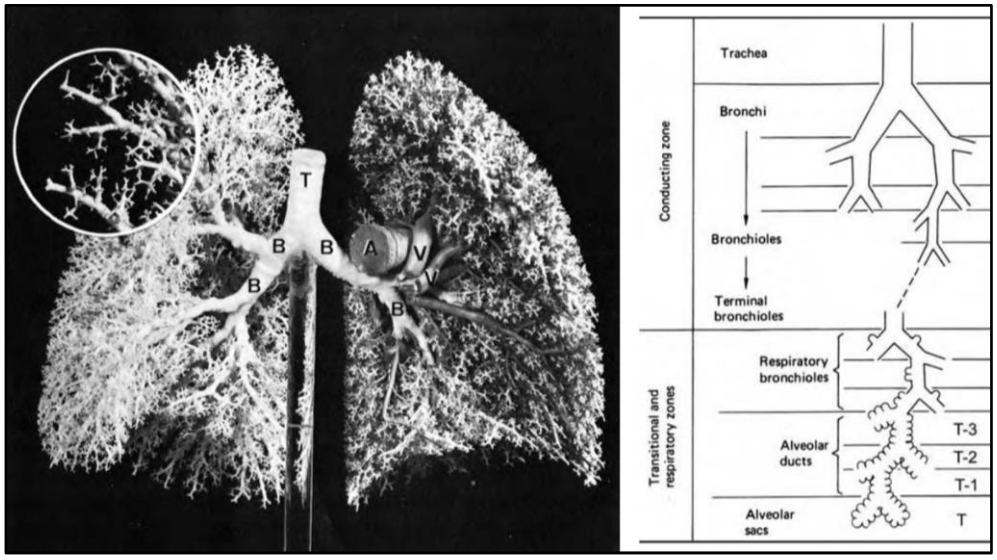

Figure 1-1. Left: Resin model of human airways. Right: Schematic diagram showing the different subdivisions of the lung airway tree. Both images were extracted from (Ethier & Simmons, 2007).

The lung parenchyma comprises three components: a continuous epithelium, an interconnected capillary endothelium network, and connective tissue located in-between these last two, which serves as a support matrix for the alveolar structure (Cook & Nakano, 2015). The connective tissue is conformed by collagen and elastin fibers, both embedded in a soft gel, the proteoglycan matrix. The collagen and elastin network has the mission of bearing the mechanical stresses exerted by transpulmonary pressure during breathing cycles. Within the extracellular matrix, the fibroblast cells maintain the shape and repair of the

connective tissue and its surroundings, influenced by both biochemical and mechanical cues that occur during the breathing cycle (Laurent, Chambers, Hill, & McAnulty, 2007).

The alveolus network must comply with some functional requirements; for example, it must provide a large surface area (in humans is about 140 m^2) to generate an extensive and efficient gas-blood exchange. This diffusion barrier between gas and blood must be thin enough (about 2 µm for humans) to allow air and blood to come in close contact and permeable enough to produce the gas exchange (Gehr, Bachofen, & Weibel, 1978).

1.3 Micromechanics of the lung

The analysis of lung micromechanical behavior becomes extremely difficult due to the large number of parallel processes occurring at different tissue scales. For example, at a microscopic level, gas exchange at the respiratory surfaces depends on an adequate matching of ventilation and perfusion through complex branching structures that are physically tethered to the surrounding extracellular matrix (ECM). On the other hand, at the macroscopic level, the lung parenchymal tissue is required to undergo relatively large strain during normal ventilation cycles (Suki & Stamenović, 2011). The overlapping of these processes generates a mismatch in the lung parenchymal tissue's mechanical response, making it highly non-linear and difficult to model. Indeed, the mechanisms by which alveolar tissue deform are not yet fully clarified, mostly due to its micrometric dimensions, becoming it incredibly challenging to analyze, both in theoretical and experimental terms (E. R. Weibel, 1983).

But the lung mechanical analysis is not a novel topic; it has been tried to be elucidated for various decades by several research groups. One of the first attempts was performed by Hildenbrandt (Hildebrandt, 1970), who carried out p-V curves in cat lungs. These experiments allowed measuring some simple but relevant lung physiology parameters, such as compliance, elasticity, and pneumatic resistance of the tissue, using a simple and straightforward method. However, these curves do not constitute a deep analysis method to understand the respiratory system's complex functioning and even less of the mechanics associated with the alveolar microstructure.

Interestingly, the global mechanical behavior of the lung has been shown to strongly depend on the tissue's underlying microarchitecture (Stamenovic, 1990). In general, the total amount of collagen and elastin fibers and their dimensions have been correlated with their "local" material elastance (Debora S. Faffe et al., 2006). The local elastance is also dependent on the particular geometry of the sector analyzed. For example, on the sectors in which several alveolar septums converge or where the alveolar wall is slightly thinner (structural inhomogeneities), the so-called "stress-raisers" arise. The stress-raisers refer to those zones in which stress concentration at the interfaces could be found. As Gattinoni *et al.* explain (Cressoni et al., 2015, 2017; Gattinoni, Tonetti, & Quintel, 2018), the stress raisers could frequently occur on healthy lungs, not generating any problematic condition. However, when these occur in diseased lungs, it can increase localized stresses and produce critical inflammatory reactions, thus aggravating the patient's condition. Stress raisers demonstrate that the lung microstructure, and their local micromorphology, must need to be taken into consideration when mechanical analyses were conducted.

The application of a simple mechanical model to explain the local behavior and the micromechanics of the lung parenchyma is feasible. For example, by relating the forces applied over the parenchyma tissue surrounding the air spaces to the areas on which they operate, it is possible to derive the effective pressure in the distending air spaces (Mead, Takishima, & Leith, 1970). Mead's group determined the strain and stress in a hexagonal network using the force balance principle, which resembles the lung microarchitecture. This model could be used to explain the effects that produced the lung microstructure and its inhomogeneities in the stress distributions within the alveolar wall network.

Several mechanical models specially designed for lung tissue analysis receive as input geometrical, morphological, and/or compositional data of the material. Accordingly, obtaining reliable and real data from lung microstructure is essential to generate reproducible results. This is the main reason why predictive models based on real alveolar geometries that use mechanical parameters experimentally obtained (with physical meanings) have become popular during recent years.

One of the main problems of obtaining real alveolar geometries is derived from its micrometric dimensions, making it challenging to accurately reconstruct the digital images.

Accordingly, Gefen *et al.* (Gefen, Elad, & Shiner, 1999; Gefen, Halpern, Shiner, Schroter, & Elad, 2001) performed a mechanical analysis using scanning electron microscopy (SEM) images of alveolar tissue sectors. In their study, finite-element meshes were generated using the geometry obtained from high-resolution images of lung parenchyma. Using static equilibrium and different levels of loads (alveolar pressure), the deformed state was obtained together with the strain and stress distribution in the samples analyzed. Interestingly, they found stress concentrations in localized sectors, thus leading to dangerous values in emphysematous lungs. More recently, Perlman *et al.* (Perlman & Bhattacharya, 2007; Perlman & Wu, 2014) used the model proposed by Mead *et al.* to estimate the local elastance of the alveolar wall in different sectors of the lung parenchyma. They calculated the local strain of the alveolar septum by analyzing confocal fluorescence microscopy images of *post mortem* lung slices at a particular alveolar pressure (Figure 1-2, top). With these images, they could segment the alveolar wall and determine the local strain by tracking each alveolar septum movement. Using this data and Mead's mechanical model, they computed the stress distribution in the analyzed sector. The results demonstrated (Figure 1-2, bottom) that while strain values appear to be randomly distributed, stress values concentrate around large alveoli that lack cross bridges or septums, thus supporting the hypothesis of stress raisers generation due to the presence of local geometrical inhomogeneities of the lung parenchyma.

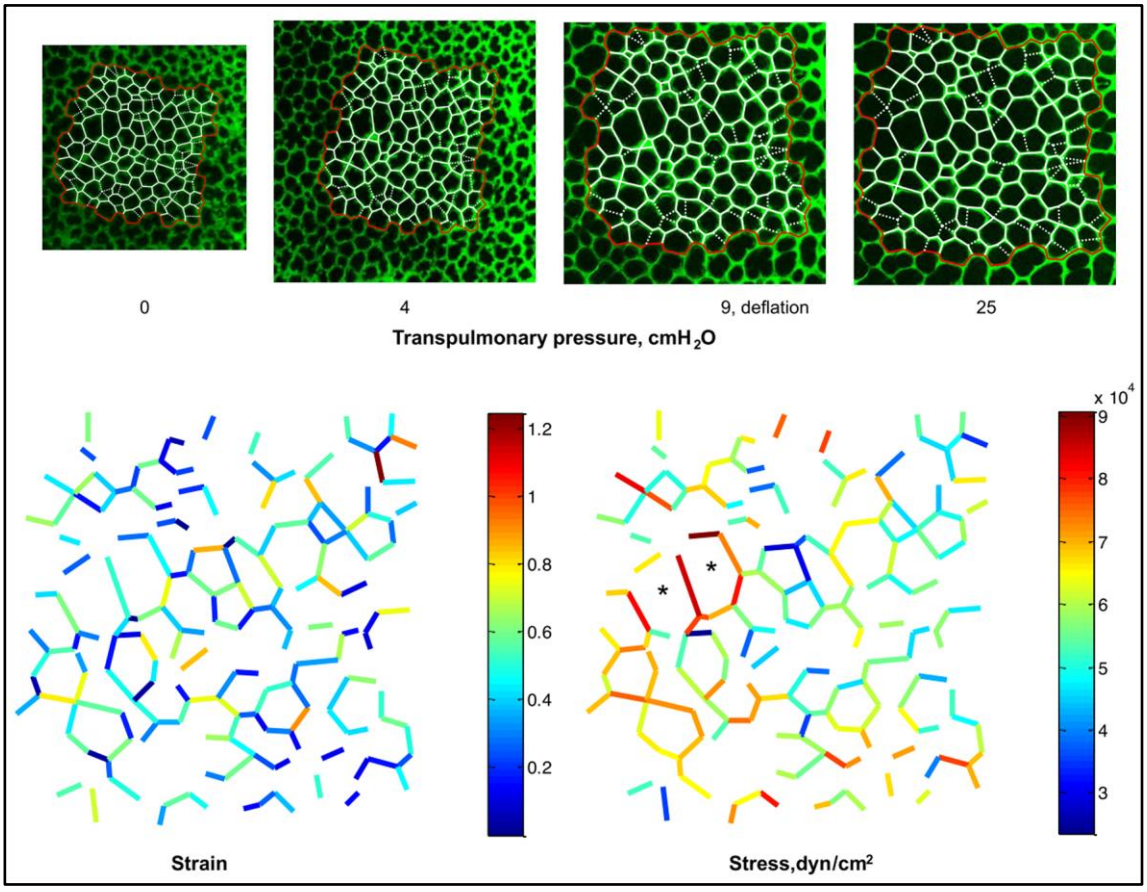

Figure 1-2. Top: Confocal microscopy images of fluorescently labeled vasculature in subpleural alveoli at variable transpulmonary pressure with an overlay of alveolar element model used for material analysis (red lines: the periphery of the region, white lines: cross-bridge structures used in the mechanical model). Bottom: Alveolar septal strain and stress of the cross-bridges analyzed. Images extracted from (Perlman & Wu, 2014).

All these studies have one crucial common issue that remains unsolved, and it is associated with the lack of out-of-plane mechanical analysis. None of these assumptions are genuinely representative of lung parenchyma stress distribution. As this tissue has a complex three-dimensional structure, the stresses are distributed evenly in all directions, not only on a plane, as it was proposed from the analysis of two-dimensional images.

Accordingly, some research groups (S. M K Rausch, Haberthür, et al., 2011) studied the strain distribution of alveolar tissue in a real three-dimensional model to resolve this issue. These geometries were obtained via μ-CT, which allows detecting the three-dimensional

structure of complex samples with a micrometric resolution using non-invasive X-ray tomographies. Small cubes of murine lung parenchyma were analyzed through the development of mechanical models based on finite-element simulations. Two different kinds of displacements (uniaxial elongation and simple shear, see Figure 1-3, bottom) were tested to determine, in a continuum fashion, the strain distribution in the alveolar tissue. The conclusions obtained were similar to those reported by Perlman *et al.*; local strain concentrations more than four times higher than the average global strain were obtained (but in 3D instead of 2D, Figure 1-3, top). While these findings provide in-depth knowledge about the 3D deformation of lung parenchyma under idealized boundary conditions, an accurate and complete study of the strain and stress distribution in the alveolar walls of acinus under realistic loading conditions remains understudied.

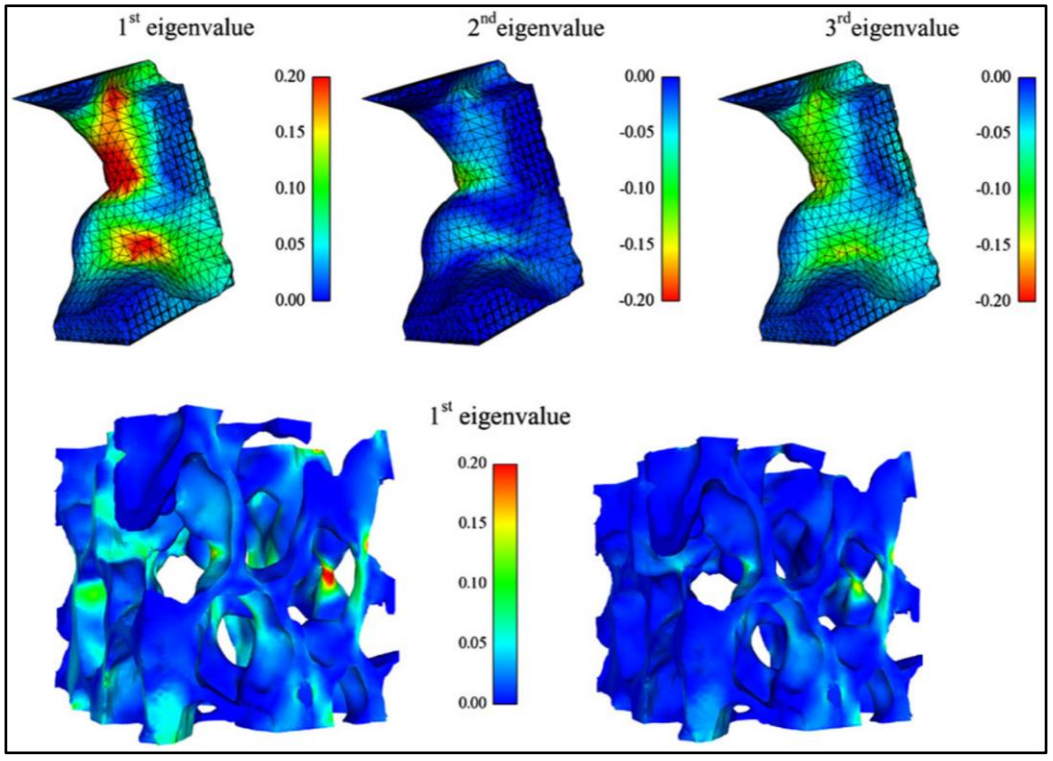

Figure 1-3. Top: 1st, 2nd, and 3rd strain eigenvalues of a sector of the lung parenchyma with increasing strain values ("stress raiser") with an arrow indicating the direction of the uniaxial stretch. Bottom: Comparison between uniaxial tension and shear deformation of the small cube for the 1st strain eigenvalue. Images extracted from (S. M K Rausch, Haberthür, et al., 2011).

1.4 Micro-CT imaging and tissue fixation methods

The use of the μ-CT technique has been steadily growing in the last years, particularly in biomedical research, due to its wide range of applications in studying microstructural features in biological tissues/organs. In general, CT is a three-dimensional imaging method involving X-ray radiation to obtain projection images at different angles of view around the object axis. A tomographic reconstruction algorithm based on the inverse Radon transform generates a stack of thin tomographic images of contiguous transaxial slices. A specimen is usually scanned by rotating it around a vertical axis within a system comprising a stationary X-ray source and a detector (Ritman, 2011) (see Figure 1-4).

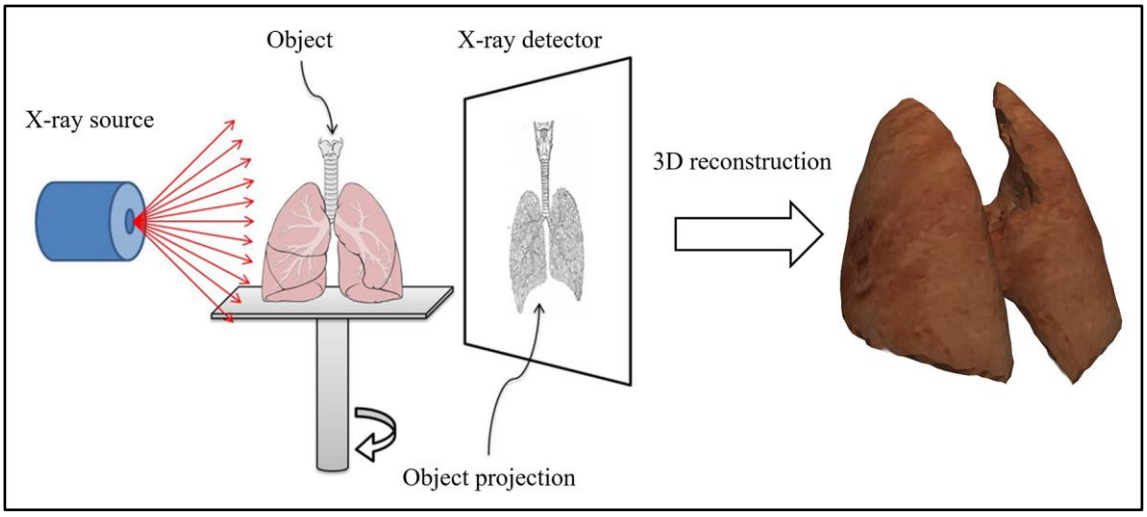

Figure 1-4. Schematic representation of an *ex vivo* μ-CT equipment.

The μ-CT technique is similar in concept to a standard CT, with the main difference that the resolution of the first one is several orders of magnitude higher than the second. As the name indicates, micrometric CT or μ-CT can resolve objects with dimensions of few microns, making it possible to detect the microstructure of several materials, including skeletal, soft tissues, and organs (Ehling et al., 2014; Rajapakse et al., 2015). The μ-CT technique could be used to analyze the respiratory patterns in free-breathing and mechanically ventilated rats (Ford et al., 2014, 2017), which could be highly useful for lung physiologists to understand further the lung microstructure behavior and the effect of changes in the microstructure on

respiratory diseases like emphysema or ARDS (Langheinrich et al., 2004). However, there are some remaining issues should be solved. The μ-CT has several advantages against other imaging techniques, such as the obtention of three-dimensional reconstructions with high resolution using a non-invasive approach. Nevertheless, this technique also presents some disadvantages, such as long acquisition times. Besides, sample fixation is needed in biological tissues to avoid image artifacts due to sample deformation during the image acquisition, like shrinking due to tissue deswelling.

The lung has become one of the favorite organs to be analyzed with μ-CT because it is a suitable technique to characterize its porous and intricate microarchitecture. One of the first studies that used μ-CT to analyze lung microstructure was published in 2001 (Kriete, Breithecker, & Rau, 2001). Later, Watz *et al.* (Watz, Breithecker, Rau, & Kriete, 2005) studied the physiological and morphometrical appearance of two left human lungs, one normal and one with centrilobular emphysema. From this point onwards, several clinical studies related to lung diseases were analyzed using the μ-CT technology, like fibrosis (Ask et al., 2008; Ruscitti et al., 2017; Scotton et al., 2013), adenocarcinoma (Deng, Xiao, Qiang, Li, & Zhang, 2017), or interstitial lung disease (Bell, Rudmann, Wood, Schwarz, & Rahimi, 2018), among others.

Some studies were focused on characterizing the lung's microarchitecture and comparing the μ-CT images and histological cut images of porcine lungs leading to the conclusions that the dimensions of alveolar spaces and alveolar septa are almost the same for both methodologies (Litzlbauer et al., 2006). However, some histological cuts sections seem slightly deformed, meaning that the procedure used to create the lung slices could affect the alveolar network structure.

Similarly, Vasilescu *et al.* performed a series of experiments related to μ-CT measurements in murine lungs. In these studies, they optimized the parameters and the methodology used for lung preparation (Dragos M Vasilescu, Knudsen, Ochs, Weibel, & Hoffman, 2012). In particular, they employed a two-stage perfusion set-up with fixative solutions connected to a manometer to control the lung inflation pressure. Their methodology allows for maintaining the whole lung volume during at least 70 days after fixation. Some morphometric analysis of the lung microarchitecture was also performed to corroborate

possible deformations due to fixation. These analyses delivered important morphological values of the alveolar network, such as alveolar radius, alveolar surface, surface-to-volume ratio, airway diameter, among others (D. M. Vasilescu et al., 2012; Dragoş M. Vasilescu et al., 2013).

Other research groups also performed μ-CT scanning procedures on lung parenchyma to analyze its microstructure. One of the most relevant is reported by Parameswaran *et al.* (Parameswaran et al., 2009). They performed a three-dimensional measurement of the alveolar airspaces volumes in normal and emphysematous patients, obtaining probability density functions of the alveolar diameter distribution and highly acute values of alveolar radius and surface area. By analyzing the data, they concluded that quantifying the heterogeneity in alveolar microstructure makes it possible to provide new insight into emphysema's pathogenesis and disease progression.

Finally, one of the most recent and exciting advances in lung microstructure acquisition was the development of an innovative method for *in vivo* microtomographic imaging (Lovric et al., 2017). Using a synchrotron-based CT and an innovative design for heartbeat/respiratory-triggered gating system, Lovric *et al.* acquired images of the lung microarchitecture with high-resolution and high signal-to-noise ratio (Figure 1-5, top). This advance is crucial to understand the structural deformation (strain) and the mechanical forces (stress) involved in the respiratory cycle. In Figure 1-5 (bottom) is possible to observe the same sector of the lung microarchitecture under different transpulmonary pressures (5, 10, and 15 cm of H_2O). The red outlined section shows that it is possible by using this technology to determine the lung parenchyma deformation locally and to track, in three-dimensions, the movements of the alveolar wall during breathing cycles on *in vivo* subjects.

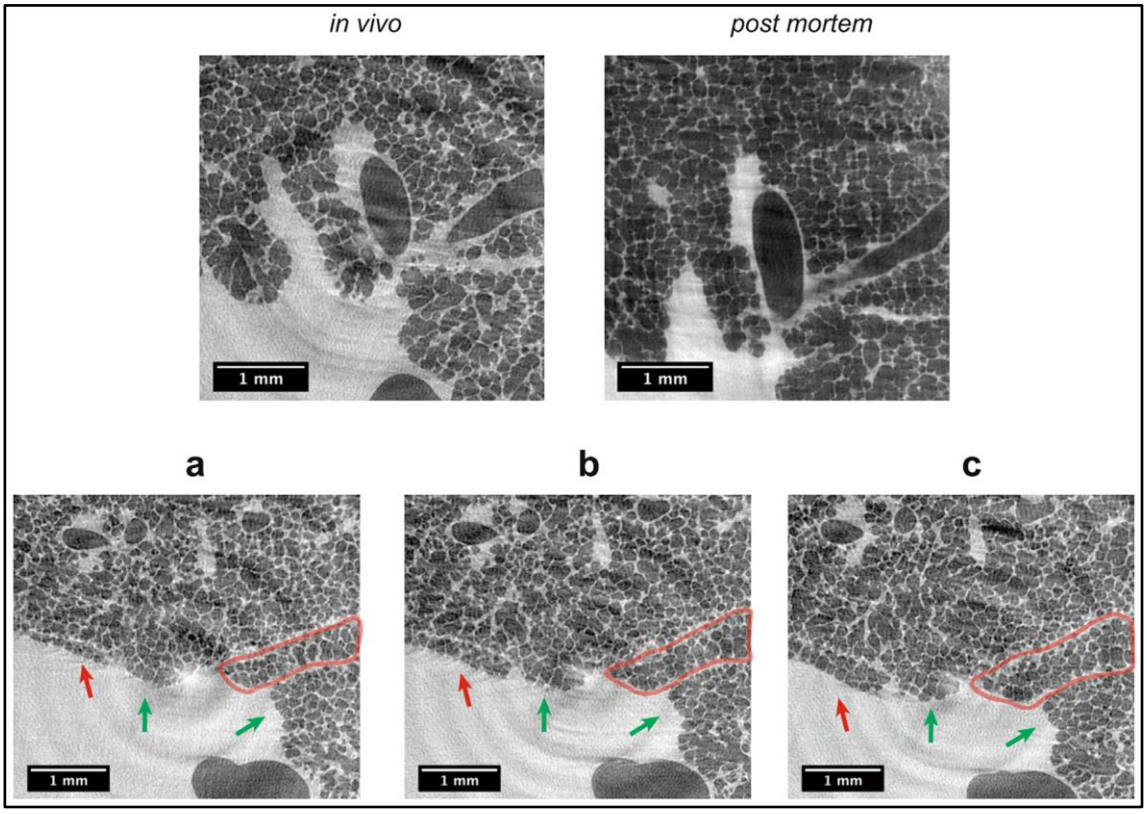

Figure 1-5. Top: Comparison of the image quality of *in vivo* and *post mortem* tomographic slices of the lungs. Bottom: Lungs different grades of inflation at three different pressures: (a) 5 cm H_2O, (b) 10 cm H_2O and (c) 15 cm H_2O. Images extracted from (Lovric et al., 2017).

1.5 Mechanical tests on lung tissue

Despite all these advances in medical imaging technology, it is critical to understand the micromechanics of the lung parenchyma to carry out uni- or bi-axial tensile tests as precise experiments to characterize lung tissue behavior either dynamically or statically. One of the first studies on this topic was performed on feline lungs (Fukaya, Martin, Young, & Katsura, 1968). In their report, Fukaya *et al.* demonstrate that the lung parenchyma exhibited a nonlinear trend (stress-strain) when subjected to a uniform and controlled load (close to 60-80% in a normal breathing cycle). Furthermore, its deformation curves show severe and marked hysteresis signals when it is not tested under controlled saline liquid environments,

mainly due to viscoelastic effects generated by the loss of internal energy in the material due to tissue deswelling (Mortola, 2013).

Several similar studies have been performed in the past years. For example, the group of Suki *et al.* (Kononov et al., 2001; H. Yuan et al., 2000) designed mechanical experiments using lung tissue strips from healthy and emphysematous patients. These strips were subject to an enzymatic procedure based on collagenase and elastase digestion. The strain-stress curves were compared before and after the enzymatic procedure, concluding that the fraction of intact fibers, either collagen or elastin, after digestion decreases, which, at the same mean strain, leads to a decrease in elastic moduli. On the other hand, at the same mean stress, collagen fibers operate at a higher portion of their stress-strain curve, which increases its moduli. Further, they discussed how mechanical forces, via collagen and elastin stress redistribution, can contribute to emphysema disease progression at various length scales, either in parenchyma microstructure or in lung macrostructure (Suki et al., 2012).

Other similar studies were performed using healthy lung slices (Bel-Brunon, Kehl, Martin, Uhlig, & Wall, 2014; Birzle, Hobrack, Martin, Uhlig, & Wall, 2019). The analysis of these results leads to analogous conclusions, but with some interesting new findings. For example, they demonstrate that as collagen and elastin fibers are morphologically interconnected, a mechanical interaction between these fibers occurs, and it has to be taken into consideration for mechanical studies of lung parenchyma (S. M K Rausch, Martin, Bornemann, Uhlig, & Wall, 2011).

These studies demonstrate that the geometrical and structural information about the lung microarchitecture is fundamental to carrying out the tissue's numerical mechanical analysis. However, the compositional information about the material, like collagen or elastin content, is also crucial to clarify its behavior under particular conditions or diseases. The integration of compositional, geometrical, and structural data of the lung parenchyma, together with the acquisition of high-resolution three-dimensional real structures of the lung tissue, could be the key to develop a multiscale predictive model of the lung under normal or pathological conditions.

1.6 Hypothesis and Objectives

In this work, we hypothesize that the three-dimensional micromechanics and morphology of the lung parenchyma can be better described through advanced imaging techniques and numerical simulations.

General Objective

The general objective of this thesis is to develop protocols and methodologies that allow for the systematical study, both experimentally and theoretically, of the lung parenchyma micromechanical behavior using advanced imaging techniques (μ-CT).

The specific objectives are:

1. Construct three-dimensional finite-element models of the alveolar microarchitecture from μ-CT images of normal lung parenchyma samples.
2. Perform numerical simulations based on finite element analysis to determine the effect of alveolar pressure on the stress distribution in alveolar microstructures.
3. Develop new tissue fixation protocols that reduce the sample shrinkage and improve the quality of μ-CT images of the lung parenchyma, later to use them in the morphological study of the lung.
4. Characterize the mechanical behavior of *ex vivo* lung tissue treated with collagenase and elastase from uniaxial tests.

1.7 Approach of this thesis

In this work, the central theme is to develop experimental and computational tools to analyze the micromechanical behavior of lung parenchyma. This thesis is structured as follows:

- Chapter 1 presents the protocol used to obtain real geometrical models of lung parenchyma from μ-CT images. It is also presented a novel micromechanical model based on homogenization methods, which use a tetrakaidecahedron unit cell with incompressible Neo-Hookean structural elements, for account the alveolar wall tissue elastic response.
- Chapter 2 focuses on studying the three-dimensional stress distribution in the alveolar walls of healthy lungs by combining *ex vivo* μ-CT and 3D finite-element analysis. Using this methodology, we proved that the alveolar walls are subject to a fully three-dimensional state of stresses rather than to a pure axial stress state, as was stated by several previous studies performed via two-dimensional approaches.
- Chapter 3 discusses three lung fixation methods based on different dehydration protocols. This chapter also analyzes the method effectivity by comparing anatomical and geometrical parameters of the lung parenchyma like alveolar radius, surface-to-volume ratio, and global porosity, with values in the literature. Finally, a novel methodology is presented to obtain two-dimensional representations of 3D local porosity and alveolar surface area density of the lung based on μ-CT imaging.
- Chapter 4 presents the protocol employed to obtain thin lung slices, which should be used to measure lung parenchyma's mechanical properties. Together with this, different proteases (collagen and elastin) were used to digest the fibers of the parenchymal tissue with the finality to detect the mechanical effects derived from these alterations.

2. CHAPTER I: MICROMECHANICAL MODEL OF LUNG PARENCHYMA HYPERELASTICITY.

2.1 INTRODUCTION

The lung is the main and largest organ of the respiratory system and is essential for the process of respiration, *i.e.*, the exchange of oxygen and carbon dioxide through the blood-air barrier. To accomplish such vital function, the lung must cyclically deform to accommodate and discharge considerable volumes of air during ventilation, a life-long process that fundamentally depends on the mechanics of the lung tissue, understood as its ability to deform and bear stresses within physiological limits (John B. West, 2012). Mechanics also plays a crucial role in the development of the respiratory diseases, as excessive stretching of the alveolar tissue may result in inflammation and ultimately in lung injury in patients undergoing mechanical ventilation, where large air volumes or high airway pressures may be necessary to recruit alveolar units (ARDS Network, 2000). The importance of mechanics in lung physiology has led clinicians and physiologists to develop mathematical models of the mechanical behavior of the lung, as they allow for *in-silico* experimentation with a fine-level resolution that is otherwise difficult, if not impossible, to perform in the wet laboratory. Some notable applications are the study of how airway bronchoconstriction controls the deposit of aerosols in the airway tree (Amin, Majumdar, Frey, & Suki, 2010) and the simulation of the alveolar recruitment/derecruitment process during mechanical ventilation (Ma & Bates, 2010). Recently, biomechanical analysis of CT images of the lung has allowed for the construction of three-dimensional maps of continuum-based deformation measures (Hurtado, Villarroel, Retamal, Bugedo, & Bruhn, 2016), demonstrating that deformation mechanisms at the tissue level can be studied *in-vivo* in human lungs (Amelon et al., 2011), and can be correlated to the severity of disease in asthmatic patients (Choi et al., 2013). Such findings cannot but stress the importance of further understanding the deformation mechanisms of lung tissue at several lengths scales both in health and disease, as well as motivate the development of novel predictive continuum models for multiscale simulations.

Throughout this work, we will concentrate on the hyperelastic response of lung parenchyma. In the following, by parenchyma, we imply the biological tissue where gas exchange occurs, mainly composed by alveoli and respiratory bronchioles having alveoli budding from the walls. Lung parenchyma features an open-foam-like architecture that can be observed through microscopy and histology, see Figure 2-2(a). The alveolar wall contains large amounts of elastin and collagen fibers embedded in a hydrated gel (Suki & Stamenović, 2011), which provide most of the elastic structural stability and strength of the tissue while displaying a marked non-linear constitutive behavior (Setnikar, 1955; Zeng, Yager, & Fung, 1987). Elastin and collagen fibers are typically aligned parallel to the alveolar wall (Toshima, Ohtani, & Ohtani, 2004), but when an aggregate of alveoli is considered, fibers show no predominant orientation for the ensemble. The random nature of fiber orientation has been the main argument for assuming lung parenchyma as an isotropic material at the tissue level, an assumption that has long been supported by experiments of human and rat tissue samples under tri-axial loading (Hoppin, Lee, & Dawson, 1975). Several attempts have been made in the past to characterize the constitutive behavior of lung parenchyma at the tissue level. Linear elastic models have been the most popular (see (Suki & Stamenović, 2011) for a thorough review), although the non-linear elastic behavior of lung parenchyma has long been deemed fundamental to explain the organ-level mechanical response (J. B. West & Matthews, 1972). The consideration of large deformations into constitutive modeling has been undertaken by many groups, where lung parenchyma response has been modeled using a Fung-like exponential strain energy function (Adil Al-Mayah, Moseley, Velec, & Brock, 2011; Zeng et al., 1987) to reflect the stiffening effect observed from experiments. A thorough analysis of how phenomenological hyperelastic models capture lung response was pursued by Rausch and co-workers (S. M K Rausch, Martin, et al., 2011), where an inverse analysis using data from uniaxial tests on murine lung samples was performed to select the best model among a set of classical strain-energy density functions, including the Mooney-Rivlin, Yeoh, and Blatz-Ko models. While phenomenological models have proved very useful in modeling the mechanical response at the organ level (Adil Al-Mayah et al., 2011), they share the limitation of having a poor connection with the underlying microstructural features of lung tissue, such as tissue porosity and alveolar-level structure and material properties, which ultimately dictate the lung parenchyma elastic response.

In order to explicitly consider the parenchymal microstructure into lung tissue modeling, some micromechanical models have been developed in the past. Early attempts date back to the seminal work of Mead (Mead et al., 1970), where alveolar tissue is idealized by a two-dimensional hexagonal array. By stating equilibrium at the intersection of alveolar walls with idealized surfaces representing lung boundaries such as the pleura, they arrive at analytical expressions for the alveolar pressure as a function of volume changes that can explain important features of the macroscopic lung mechanical behavior. The work of Mead and co-workers motivated a series of 3D micromechanical models of lung parenchyma based on polygonal ducts (Karakaplan, Bieniek, & Skalak, 1980), as well as a truncated octahedral (Dale, Matthews, & Schroter, 1980; Kowe, Schroter, Matthews, & Hitchings, 1986) and dodecahedral (Budiansky & Kimmel, 1987; Kimmel & Budiansky, 1990) geometries to represent a single alveolus. By employing strut elements at the edges and triangular elements filling out the surfaces of the chosen polyhedra, a mechanical FE structural model is constructed, where phenomenological exponential-like elastic constitutive relations are assumed for the strut elements. Then, by stating the equilibrium of the structure via the virtual work principle, non-linear stress-strain relations in the isotropic expansion are numerically simulated, which reproduced with good accuracy the p-V experimental data found in the literature. Approaches focussing on structural biofibers of the connective tissue have also been pursued (Bates, 1998; Stamenovic & Wilson, 1985), where isotropic orientation distribution, rather than an idealized alveolar geometry, is employed to determine the mechanical contribution of structural proteins to the overall response of lung parenchyma. More recently, μ-CT images of murine lungs have been employed to create an FE model of a representative volume element (RVE) of lung parenchyma with micrometer dimensions where alveolated tissue is discretized using millions of tetrahedral elements (S. M K Rausch, Martin, et al., 2011; Wiechert, Comerford, Rausch, & Wall, 2011). Once the non-linear FE problem is solved, the overall response of the RVE is obtained by volumetric averaging of the resulting stress fields. Despite their ability to reproduce experimental p-V relations, most micromechanical models of lung parenchyma proposed to date suffer from important limitations. First, material parameters of exponential constitutive laws for strut uniaxial elements are highly phenomenological and are not directly related to alveolar septum mechanical properties like the elastic modulus or the Poisson ratio, making the

physical multiscale connection difficult to interpret. Second, models considering an idealized microstructural geometry or distributed fibers are not associated to the parenchymal tissue porosity, a fundamental parameter that controls the mechanical behavior of foam-like solids (Ashby & Medalist, 1983). Third, the validation of most models against experimental data has only considered the isotropic expansion case (i.e., p-V curves), largely neglecting the fact that lung parenchyma undergoes highly anisotropic deformation states *in-vivo* (Hurtado et al., 2017), which questions the validity of such models to represent a more general state of deformation. Finally, micromechanical models that use FE discretizations of idealized geometries or numerical simulations of lung parenchyma RVEs are computationally involved, as well as subject to convergence issues typically found in non-linear FE simulations.

A well-established framework to develop constitutive models that account for the underlying microstructure is homogenization theory (Suquet, 1987), where by calculating the overall properties of heterogeneous materials, one can represent the material as homogeneous with an effective response valid for larger scales. Homogenization theory has at least two key advantages over numerical multiscale models based on RVE simulations: (i) it can deliver analytical expressions for the effective constitutive response of heterogeneous solids for idealized microstructural geometry, thus making them amenable to analysis, and (ii) the resulting effective response can be evaluated by performing low-cost calculations, rendering large-scale multiscale simulations feasible without the need of supercomputers. In the case of cell foams, the homogenization approach has been pursued by several researchers to derive analytical expressions of the effective mechanical properties of linear elastic foams (Ashby & Medalist, 1983; L. J. Gibson & Ashby, 1982; T. Zhang, 2008), driven by applications in thermal insulation, packaging, structural use and buoyancy (Lorna J. Gibson & Ashby, 1999). In particular, micromechanical models based on polyhedral unit cells have been proposed in the past to understand the elastic behavior of metallic open-foam cells (Sullivan, Ghosn, & Lerch, 2008; Warren & Kraynik, 1997; Zhu, Knott, & Mills, 1997). Non-linear micromechanical models of low-density open-cell foams have also been proposed in the literature, where the underlying unit cell takes a tetrahedral shape with edges represented by strut elements (Warren & Kraynik, 1991). A general non-linear framework for modeling open-cell foams that can be generated from a unit cell using lattice vectors was

proposed by (Wang & Cuitiño, 2000), where deformation mechanisms consider not only axial deformation but also bending of uniaxial elements. A micromechanical constitutive model of a tetrahedral unit cell is developed within this framework, assuming an elasto-plastic material behavior of the unit-cell subelements. The model is demonstrated through triaxial, true shear and uniaxial loading tests, where geometrical instabilities are found in the latter case for compressive regimes, showing the suitability of the model to capture non-linear large-deformation mechanisms.

In this chapter, we hypothesize that a predictive and efficient non-linear micromechanical model of lung parenchyma suitable for large deformations can be developed based on a suitable polyhedral unit cell that adequately represents the parenchymal tissue. A micromechanical model can potentially reduce the computational effort associated with direct numerical simulations of RVEs, thus enabling predictive multiscale simulations of the whole lung. To accomplish our goal, we follow a general finite-deformation homogenization theory (Fish & Fan, 2008) based on asymptotic expansions, and consider a representative unit cell at the microscopic level with fully nonlinear constitutive behavior of its elements. We validate our model by comparison of the predictive nonlinear mechanical response with direct numerical simulations of lung parenchyma RVE constructed from μ-CT images of murine lungs under different representative loading conditions.

2.2 MICROMECHANICAL MODEL

2.2.1 Nonlinear homogenization theory

In the following, we summarize the main aspects of the finite-deformation homogenization theory based on asymptotic expansions (Fish & Fan, 2008), which is the starting point of our micromechanical model. Let Ω^{ξ} be the domain of a composite material that can be separated into coarse and fine scales, where superscript ξ indicates the existence of fine-scale features. Let Ω_X and Ω_x be the coarse-scale reference and current configurations, respectively. We denote reference coordinates by $\mathbf{X} \in \Omega_X$ and current coordinates by $\mathbf{x} \in \Omega_x$. Similarly, we denote Θ_Y and Θ_y as the reference and current fine-scale (unit-cell) configurations, respectively, with reference coordinates denoted by $\mathbf{Y} \in \Theta_Y$ and current coordinates denoted by $\mathbf{y} \in \Theta_y$, see Figure 2-1 for a schematic. We further assume that Θ_Y, Θ_y are locally periodic

domains. Fine and coarse-scale material coordinates are related by $\boldsymbol{Y} = \frac{1}{\xi}(\boldsymbol{X} - \widehat{\boldsymbol{X}})$, where $0 < \xi \ll 1$ and $\widehat{\boldsymbol{X}}$ denotes the unit cell centroid location. Following a coarse-fine two-scale scale continuum description, we write for an arbitrary tensor field $\boldsymbol{A}^{\xi}(\boldsymbol{X}) = \boldsymbol{A}(\widehat{\boldsymbol{X}}, \boldsymbol{Y})$. Then, the displacement field in the composite domain u^{ξ} can be approximated by an asymptotic expansion over $\Omega_X \times \Theta_Y$ as follows:

$$\begin{aligned} \boldsymbol{u}^{\xi}(\boldsymbol{X}) &= \boldsymbol{u}(\widehat{\boldsymbol{X}}, \boldsymbol{Y}) \\ &= \widehat{\boldsymbol{u}}^{(0)}(\widehat{\boldsymbol{X}}) + \xi\, \widehat{\boldsymbol{u}}^{(1)}(\widehat{\boldsymbol{X}}, \boldsymbol{Y}) + \xi^2 \widehat{\boldsymbol{u}}^{(2)}(\widehat{\boldsymbol{X}}, \boldsymbol{Y}) + \mathcal{O}(\xi^3) \end{aligned} \tag{2.1}$$

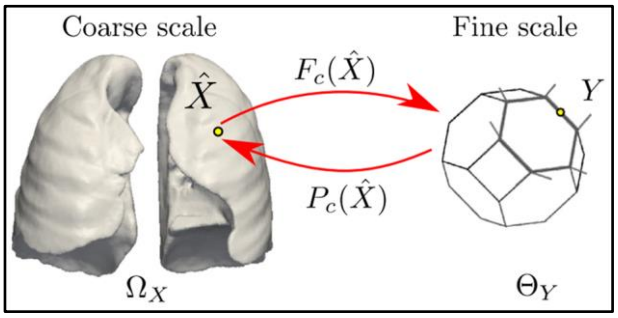

Figure 2-1. Schematic of the two-scale homogenization approach for multiscale modeling of the lung tissue.

We define the coarse-scale displacement field $\boldsymbol{u}^{c}(\widehat{\boldsymbol{X}}) := \widehat{\boldsymbol{u}}^{(0)}(\widehat{\boldsymbol{X}})$, and note from Eq. (2.1) that it corresponds to a rigid body translation on the unit cell. Matching asymptotic terms, we obtain the following expressions for the coarse-scale ($\mathbf{F}^{c}$) and fine-scale ($\mathbf{F}^{f}$) deformation gradients,

$$\boldsymbol{F}^{C}(\widehat{\boldsymbol{X}}) = \frac{\partial \boldsymbol{u}^{C}(\widehat{\boldsymbol{X}})}{\partial \boldsymbol{X}} + \boldsymbol{I} \tag{2.2}$$

$$\begin{aligned} \boldsymbol{F}^{f}(\widehat{\boldsymbol{X}}, \boldsymbol{Y}) &= \boldsymbol{F}^{C}(\widehat{\boldsymbol{X}}) \\ &+ \boldsymbol{F}^{*}(\widehat{\boldsymbol{X}}, \boldsymbol{Y}) \end{aligned} \tag{2.3}$$

Where $\mathbf{I}$ is the unit tensor, and $\mathbf{F}^{*}$ corresponds to a fluctuation tensor field. Assuming Y-periodicity, it follows that

$$\boldsymbol{F}^{C}(\widehat{\boldsymbol{X}}) = \frac{1}{|\Theta_Y|} \int_{\Theta_Y} \boldsymbol{F}^{f}(\widehat{\boldsymbol{X}}, \boldsymbol{Y})\, d\Theta_Y \tag{2.4}$$

Further, by matching terms in the asymptotic expansion of the composite equilibrium equation, the fine-scale equilibrium equation takes the form

$$\frac{\partial \boldsymbol{P}^C(\widehat{\boldsymbol{X}},\boldsymbol{Y})}{\partial \boldsymbol{Y}} = \mathbf{0} \tag{2.5}$$

where $\mathbf{P}^{\mathrm{f}}$ is the fine-scale first Piola-Kirchhoff stress tensor field, and it can be shown that the coarse-scale Piola-Kirchhoff stress tensor field can be obtained in terms of $\mathbf{P}^{\mathrm{f}}$ as

$$\boldsymbol{P}^C(\widehat{\boldsymbol{X}}) = \frac{1}{|\Theta_Y|}\int_{\Theta_Y} \boldsymbol{P}^f(\widehat{\boldsymbol{X}},\boldsymbol{Y})\, d\Theta_Y \tag{2.6}$$

Using similar arguments, one shows that the coarse-scale Cauchy stress tensor field takes the form

$$\boldsymbol{\sigma}^C = \frac{1}{|\Theta_Y|}\int_{\Theta_Y} \boldsymbol{\sigma}^f\, d\Theta_Y = \frac{1}{|\Theta_Y|}\int_{\Theta_Y} \boldsymbol{F}^f\boldsymbol{P}^f\, d\Theta_Y \tag{2.7}$$

where $\Theta_y = \varphi^{\mathrm{f}}(\Theta_Y)$, with $\varphi^{\mathrm{f}} := \mathbf{Y} + \mathbf{u}^{\mathrm{f}}(\mathbf{Y})$ the fine-scale deformation mapping. Finally, for a point $\widehat{\boldsymbol{X}} \in \Omega_X$, we define the fine-scale displacement field as $\boldsymbol{u}^f(\boldsymbol{Y}) := \widehat{\boldsymbol{u}}^{(1)}(\widehat{\boldsymbol{X}},\boldsymbol{Y})$, and focus on solving the unit cell equilibrium to the first-order term $\mathcal{O}(\xi)$. Then, the strong form of the fine-scale boundary value problem can be stated as follows: Given $\mathbf{F}^{\mathrm{C}}$, find $\mathbf{u}^{\mathrm{f}}$ on Θ_Y such that

$$\frac{\partial \boldsymbol{P}^f(\widehat{\boldsymbol{X}},\boldsymbol{Y})}{\partial \boldsymbol{Y}} = \mathbf{0}\ in\ \Theta_Y \tag{2.8}$$

$$\boldsymbol{P}^f = \boldsymbol{P}^f(\boldsymbol{F}^f)\ in\ \Theta_Y \tag{2.9}$$

$$\boldsymbol{F}^f = \boldsymbol{I} + \frac{\partial \boldsymbol{u}^f}{\partial \boldsymbol{Y}}\ in\ \Theta_Y \tag{2.10}$$

$$\boldsymbol{u}^f = (\boldsymbol{F}^c - \boldsymbol{I})\,\boldsymbol{Y}\ on\ \partial\Theta_Y \tag{2.11}$$

In the following, we will omit the superscript f for the sake of simplicity when addressing the fine-scale problem.

2.2.2 Tetrakaidecahedron (TKD) model for lung parenchyma hyperelasticity

Based on the two-scale homogenization framework presented in the previous section, here we develop a non-linear micromechanical model for the lung parenchyma hyperelastic behavior. Motivated by the alveolar microstructure observed from SEM micrographics, see Figure 2-2(a), we consider Kelvin's tetrakaidecahedron (TKD), see Figure 2-2(b), as the

predominant microstructure geometry in alveolated tissue. The study of the three-dimensional structural geometry of alveoli and alveolar ducts was carried out by (Fung, 1988), where the TKD was found to be a suitable structural model for the acinar structures, as thoroughly confirmed from histological studies. Based on this assumption, we further consider a representative TKD region, denote by TKDr, as proposed by (Warren & Kraynik, 1997), marked in gray in Figure 2-2(b). TKDr represents a basic unit of a periodic arrangement, with lattice vectors defined as (Warren & Kraynik, 1997).

$$\boldsymbol{b}_x = 2\sqrt{2}\,\delta \begin{bmatrix} -1 \\ 1 \\ 1 \end{bmatrix}, \quad \boldsymbol{b}_y = 2\sqrt{2}\,\delta \begin{bmatrix} 1 \\ -1 \\ 1 \end{bmatrix}, \quad \boldsymbol{b}_z = 2\sqrt{2}\,\delta \begin{bmatrix} 1 \\ 1 \\ -1 \end{bmatrix} \tag{2.12}$$

Where δ is the initial strut half-length, see Figure 2-2(c). With these lattice vectors defined, the corresponding Bravais lattice for a periodic TKD arrangement takes the form

$$\boldsymbol{r}_B = n_x\boldsymbol{b}_x + n_y\boldsymbol{b}_y + n_z\boldsymbol{b}_z \tag{2.13}$$

With $n_x, n_y, n_z \in \mathbb{Z}$.

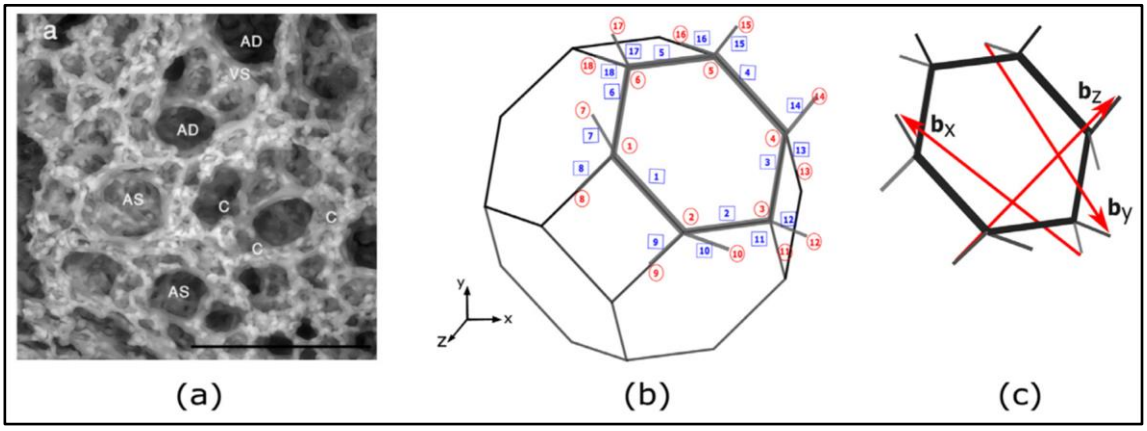

Figure 2-2. (a) Alveolar tissue microstructure is composed of alveolar sacs (AS), alveolar ducts (AD), blood vessels (VS), and capillaries (C), as shown. SEM micrography taken from (Solomonov et al., 2015) with the publisher's permission; the scale bar is 100 µm. (b) Kelvin's tetrakaidecahedron geometry. In gray, the representative region of Kelvin's tetrakaidecahedron used (TKDr) (Warren & Kraynik, 1997). Nodal and element numbers are shown into blue circles and blue rectangles, respectively. (c) Lattice vectors (in red) plotted over the unit cell. Origin is located at the center of the TKD. (For interpretation of

the references to color in this figure legend, the reader is referred to the web version of this article.).

From a structural viewpoint, alveolar septa can be idealized as a composite material with elastin and collagen fibers embedded in a hydrated gel matrix (Suki & Stamenović, 2011). To account for the elastic response and high water content of alveolar tissue, we assume an incompressible Neo-Hookean material model, whose energy density function takes the form

$$W(\boldsymbol{F}) = \frac{\mu}{2}\{tr(\boldsymbol{F}^T\boldsymbol{F}) - 3\} - p(\det \boldsymbol{F} - 1) \tag{2.14}$$

Where μ is the Lamé parameter and p is a Lagrange multiplier field, also referred to as the pressure field, needed to enforce incompressibility. We further note that the kinematic incompressibility constraint is stated as

$$\det \boldsymbol{F} = 1 \; in \; \Theta_{Y_S} \tag{2.15}$$

where $\Theta_{Y_S} \subset \Theta_Y$ is the solid phase (alveolar walls) of the unit cell. We reformulate the fine-scale problem defined by Eq. (2.8) – (2.11) with constitutive law Eq. (2.14) and the incompressibility constraint Eq. (2.15) as the saddle-point mixed variational principle

$$\min_{\boldsymbol{F} \in \boldsymbol{F}_{adm}} \max_{p \in L^2(\Theta_Y)} \int_{\Theta_Y} \left[\frac{\mu}{2}\{tr(\boldsymbol{F}^T\boldsymbol{F}) - 3\} - p(\det \boldsymbol{F} - 1)\right] d\Theta_Y \tag{2.16}$$

where

$$\boldsymbol{F}_{adm} \coloneqq \{\boldsymbol{F} : \Theta_Y \rightarrow \mathbb{R}^{n \times n} : \det \boldsymbol{F} > 0 \; in \; \Theta_Y \; and \; \boldsymbol{F} = \boldsymbol{F}^C \; on \; \partial\Theta_Y\} \tag{2.17}$$

To solve Eq. (2.16) we consider the struts of the TKDr as one-dimensional structural elements, which are interconnected at nodes. This simplification results in a 3D truss structure with elements, see Figure 2-2. Displacement vectors at the nodes will serve as degrees of freedom (DOFs) for the structure, where we denote by $\mathbf{u}_i$ the nodal displacement vector for the i−th node. We further assume axial symmetry for the struts, as well as a constant pressure throughout each element, and axial deformation defined by the difference of displacement of the boundary nodes. These assumptions are justified by the slender and predominantly axial geometry of the TKDr struts, and the fact that deformation energy due to axial deformation will dominate over bending energy (Kowe et al., 1986; Warren &

Kraynik, 1991). Under these assumptions, one shows that the deformation gradient of the e-th element takes the form

$$\boldsymbol{F}_e = \begin{bmatrix} \lambda_e & 0 & 0 \\ 0 & \lambda_e^T & 0 \\ 0 & 0 & \lambda_e^T \end{bmatrix} \tag{2.18}$$

where λ_e, λ_e^T are the axial and transverse stretch ratios, respectively. In particular, the axial stretch ratio is defined as

$$\lambda_e := \frac{\|\boldsymbol{q}_e\|}{L_{e0}} \tag{2.19}$$

Where $\mathbf{q}_e$ is the difference between end-node coordinates in the current configuration for the e-th element, see Supplementary material (S 2-1). Similarly, we define $\mathbf{Q}_e$ as the difference between end-node coordinates in the reference configuration and note that $L_{e0} = \|\boldsymbol{Q}_e\|$. Then, the element deformation energy takes the form

$$\begin{aligned} \prod_e^{axial}(\boldsymbol{q}_e, \lambda_e^T, p_e) &= \int_0^{L_{e0}} \int_{A_0} \left\{ \frac{\mu}{2}\left(\lambda_e^2 + 2\lambda_e^{T^2} - 3\right) - p_e(\lambda_i(\lambda_e^T)^2 - 1) \right\} dA\, dL \\ &= A_0 L_{e0} \left\{ \frac{\mu}{2}\left(\lambda_e^2 + 2\lambda_e^{T^2} - 3\right) - p_e(\lambda_e(\lambda_e^T)^2 - 1) \right\} \end{aligned} \tag{2.20}$$

Where p_e is the element's pressure, A_0 is the reference cross-sectional area, assumed to be the same for all elements, and L_{e0} is the initial length of the element. Since the pin-jointed TKDr structure represents a mechanism, *i.e.*, it allows for non-zero displacements at no energy cost, we consider the addition of rotational energy terms to Eq. (2.20) to stabilize the system. To this end, we consider a rotation as the difference between the initial and final angle subtended between two elements connected to the same joint, identified by a pair $j = (j_1, j_2)$ from the pair set $\mathcal{J}$ listed in Supplementary material (S 2-1). We note that for the TKDr there are 36 possible rotations. Then, the energy contribution associated with the j-th rotation is assumed to take the form

$$\prod_j^{rotational}(\boldsymbol{q}_{j1},\boldsymbol{q}_{j2}) = \frac{1}{2}k_\theta\left\{\frac{\boldsymbol{q}_{j1}\cdot\boldsymbol{q}_{j2}}{\|\boldsymbol{q}_{j1}\|\,\|\boldsymbol{q}_{j2}\|}-\frac{\boldsymbol{Q}_{j1}\cdot\boldsymbol{Q}_{j2}}{\|\boldsymbol{Q}_{j1}\|\,\|\boldsymbol{Q}_{j2}\|}\right\}^2 \quad (2.21)$$

Where k_θ is a rotational stiffness assumed to take the same value for all possible rotations in the TKDr. Adding all energy contributions, the potential energy for the TKDr reads

$$\prod = \sum_{e=1}^{18}\prod_e^{axial} + \sum_{j\in J}\prod_j^{rotational} 1 \quad (2.22)$$

Relations between nodal displacements will arise from kinematic and symmetry considerations for the TKD. Supplementary material (S 2-1) contains the complete development of the mathematical expressions associated with these kinematic constraints.

In particular, we will assume symmetry with respect to planes defined by X = 0 , Y = 0 , and Z = 0 . Additionally, we will assume that the edges of the rhomboid faces of TKD will lie on a common plane after deformation. We further consider that $\mathbf{F}^C$ represents a principal deformation state, and therefore it takes the diagonal form

$$\boldsymbol{F}^C = \begin{bmatrix}\lambda_1^C & 0 & 0\\ 0 & \lambda_2^C & 0\\ 0 & 0 & \lambda_3^C\end{bmatrix} \quad (2.23)$$

Where $\lambda_1^c,\lambda_2^c,\lambda_3^c$ are the coarse-scale principal stretches. For the case of an arbitrary deformation gradient tensor, a principal-direction constitutive modeling approach can be employed, where the principal stretches of the deformation gradient tensor are considered in Eq. (2.23), and the resulting stresses are aligned with the principal directions. Lattice vectors defined in Eq. (2.12) and boundary conditions Eq. (2.11) deliver additional relations between nodal displacements. Altogether, these assumptions allow us to express nodal displacements in the TKDr in terms of a reduced set of DOFs and $\mathbf{F}^C$, which we write $\boldsymbol{u}_i = \boldsymbol{u}_i(r,\boldsymbol{F}^C), i = 1,18$, where

$$\boldsymbol{r} = \begin{bmatrix}u_{1y}\\ u_{2x}\\ u_{3z}\end{bmatrix} \quad (2.24)$$

is a vector with unknown DOFs, whose entries coincide with displacements of a reduced set of selected nodes, see Supplementary material (S 2-1). Let $p = [p_1,\dots,p_{18}]^T, l =$

$[\lambda_1^T, \dots, \lambda_{18}^T]^T$. Then, using simplifications above, the variational principle Eq. (2.16) can be rewritten as the optimization problem

$$\min_{\boldsymbol{r} \in \mathbb{R}^3, \boldsymbol{l} \in \mathbb{R}^{18}} \max_{\boldsymbol{p} \in \mathbb{R}^{18}} \prod(\boldsymbol{r}, \boldsymbol{l}, \boldsymbol{p};\ \boldsymbol{F}^C) \tag{2.25}$$

where the extended Lagrangian function takes the form

$$\begin{aligned}\prod(\boldsymbol{r}, \boldsymbol{l}, \boldsymbol{p};\ \boldsymbol{F}^C) := \sum_{e=1}^{18} \left\{\frac{\mu}{2}[\lambda_e^2 + 2(\lambda_e^T)^2 - 3] - p_e[\lambda_e(\lambda_e^T)^2 - 1]\right\} A_0 L_{e0} \\ + \sum_{j \in \mathcal{J}} \frac{1}{2} k_\theta \left\{\frac{\boldsymbol{q}_{j1} \cdot \boldsymbol{q}_{j2}}{\|\boldsymbol{q}_{j1}\| \|\boldsymbol{q}_{j2}\|} - \frac{\boldsymbol{Q}_{j1} \cdot \boldsymbol{Q}_{j2}}{\|\boldsymbol{Q}_{j1}\| \|\boldsymbol{Q}_{j2}\|}\right\}^2\end{aligned} \tag{2.26}$$

From stating stationary conditions $\frac{\partial \Pi}{\partial \boldsymbol{l}} = \boldsymbol{0}$ and $\frac{\partial \Pi}{\partial \boldsymbol{p}} = \boldsymbol{0}$ it follows that

$$\lambda_e^T = \lambda_e^{\frac{-1}{2}}, \qquad e = 1, 18 \tag{2.27}$$

$$p_e = \frac{\mu}{\lambda_e}, \qquad e = 1, 18 \tag{2.28}$$

which implies that transverse stretch and pressure can be solved at the element level in terms of displacements **r**, a dependence we express as $\boldsymbol{l} = \boldsymbol{l}(\boldsymbol{r};\ \boldsymbol{F^C})$ and $\boldsymbol{p} = \boldsymbol{p}(\boldsymbol{r};\ \boldsymbol{F^C})$. Substituting Eq. (2.27) and Eq. (2.28) into Eq. (2.25) leads to the effective minimization problem

$$\min_{r \in \mathbb{R}^3} \prod^{eff}(\boldsymbol{r};\ \boldsymbol{F^C}) \tag{2.29}$$

where

$$\begin{aligned}\prod^{eff}(\boldsymbol{r};\ \boldsymbol{F^C}) = \sum_{e=1}^{18} \frac{\mu}{2} A_0 L_{e0} \left\{\lambda_e^2 + \frac{2}{\lambda_e} - 3\right\} \\ + \sum_{j \in \mathcal{J}} \frac{1}{2} k_\theta \left\{\frac{\boldsymbol{q}_{j1} \cdot \boldsymbol{q}_{j2}}{\|\boldsymbol{q}_{j1}\| \|\boldsymbol{q}_{j2}\|}\right. \\ \left. - \frac{\boldsymbol{Q}_{j1} \cdot \boldsymbol{Q}_{j2}}{\|\boldsymbol{Q}_{j1}\| \|\boldsymbol{Q}_{j2}\|}\right\}^2\end{aligned} \tag{2.30}$$

We will be interested in relating A_0 with physical parameters of lung parenchyma. Let $|\Theta_Y|$ be the total volume of the unit cell in the reference configuration, and $|\Theta_{Y_S}|$ be the solid phase volume, such that the TKD porosity is defined by

$$f_0 := 1 - \frac{|\Theta_{Y_S}|}{|\Theta_Y|} \tag{2.31}$$

Following (Warren & Kraynik, 1997), in the sequel, we will consider that $|\Theta_Y| = 64\sqrt{2}\delta^3$, which is based on the fact that our micromechanical model is scale-invariant. Assuming that all elements have the same the initial cross-section A_0, we write

$$|\Theta_{Y_S}| = (1 - f_0)|\Theta_Y| = A_0 L_T \tag{2.32}$$

Where L_T is the total effective length of the TKDr in the reference configuration. Noting that the TKDr has 6 elements with $L_{e0} = 2\delta$ and 12 elements with $L_{e0} = \delta$, it follows that

$$L_T = 24\delta - L_{OL} \tag{2.33}$$

Where L_{OL} is the total element overlap length (Wang & Cuitiño, 2000), which is subtracted to avoid volume duplication, from the lung microstructure, elastin, and collagen fibers are disposed in a network such that alveolar walls are assumed to have a rod-like shape in the central region and a tapered portion towards the junction with other walls. Noting that there are 6 element joints for the TKDr, and that at each joint there are 4 connecting element, we write

$$\begin{aligned} L_{OL} &= 6 \times 3\delta \times d \\ &= 18\delta d \end{aligned} \tag{2.34}$$

Where the ratio d represents the fraction of the strut that is duplicated by overlapping, combining Eq. (2.32) –(2.34), the cross-sectional area takes the form

$$A_0 = \frac{32\sqrt{2}(1 - f_0)\delta^2}{12 - 9d} \tag{2.35}$$

For the case of bending energy, we will assume that $k_\theta = \alpha\frac{EI}{2\delta}$, where E = 3μ is the elastic modulus, I is the inertia of a solid circular section with area A_0, and α is a coefficient to be fixed.

The effective minimization problem Eq. (2.29) was numerically solved using the `fsolve` function of the `scipy` library (version 0.14.0) (Jones, Oliphant, & Peterson, 2001), which implements Powell's hybrid method (Powell, 1964). Once the TKDr model is solved, we will be concerned with the stress averaging in the unit cell to determine the macroscopic stress tensor σ^c, as defined in Eq. (2.7). We note that

$$\boldsymbol{\sigma}^C = \frac{1}{|\Theta_y|}\int_{\Theta_y} \boldsymbol{\sigma}^f d\Theta_y$$
$$= \frac{1}{|\Theta_y|}\int_{\partial\Theta_y} \boldsymbol{t}^f \otimes \boldsymbol{y}\, d\partial\Theta_y \quad (2.36)$$

Where $\mathbf{t}^f$ is the fine-scale traction vector acting on the unit-cell boundary. In the case of the TKDr, it can be shown that Eq. (2.36) reduces to

$$\boldsymbol{\sigma}^C = \frac{1}{|\Theta_y|}\sum_{e=7}^{18} \boldsymbol{f}_e \otimes \boldsymbol{y}_e \quad (2.37)$$

Where $\mathbf{y}_e$ is the current position of node e and $|\Theta_Y|$ is the current configuration volume of the TKDr unit cell computed as $|\Theta_Y| = J^C|\Theta_Y|$, with $J^C := \det \boldsymbol{F}^C$. Eq. (2.37) can be further reduced by the periodicity of the TKD (Warren & Kraynik, 1997), which leads to the expression

$$\boldsymbol{\sigma}^C = \frac{2}{|\Theta_Y|}\big(\boldsymbol{f}_7 \otimes \boldsymbol{F}^C\boldsymbol{b}_x + \boldsymbol{f}_{10} \otimes \boldsymbol{F}^C\boldsymbol{b}_y + \boldsymbol{f}_{15} \otimes \boldsymbol{F}^C\boldsymbol{b}_z\big) \quad (2.38)$$

Finally, we note that axial force in TKDr elements can be computed as

$$\|\boldsymbol{f}_e\| = \mu A_0\big(\lambda_e - \lambda_e{}^{-2}\big) \quad (2.39)$$

with direction of the axial elements given by $\mathbf{q}_e$.

2.3 DIRECT NUMERICAL SIMULATION (DNS) OF RVEs

μ-CT reconstructions of murine lungs were acquired to construct the geometry of an RVE of the lung parenchyma. To this end, adult male Sprague-Dawley rats in healthy condition (≈ 300 gr.) under a conventional diet were sacrificed following the international guidelines given by the American Veterinary Medical Association (Leary, Underwood, Anthony, & Cartner, 2013). Lungs were carefully excised from the thorax, and then fixed using a formalin buffered saline solution, and later kept into the fixation solution for at least 7 days (Parameswaran et al., 2009). To study an expiration and inspiration condition, samples with inflation pressures of 10 cm H_2O and 20 cm H_2O were prepared, respectively. To dry the organs and maintain their morphology for following measurements, a desiccating process was performed based on graduating ethanol baths. The lung was immersed into a 50% ethanol and 50% phosphate-buffered saline solution and maintained for one hour. Then the

ethanol concentration was gradually increased in hourly steps (60%, 70%, 80%, and 90%), using the same procedure just described, until the solution reached a 100% ethanol concentration, which was maintained overnight (Dudak et al., 2016; Scotton et al., 2013). Before μ-CT image acquisition, the lungs were left drying in atmospheric conditions for 24 h in order to evaporate the remaining ethanol. The samples were placed in a sample holder and were scanned using the commercial μ-CT scanner SkyScan 1272 from Bruker. The X-ray source was set to operate at 45 kV and 225 μA. Whole-lung tomographic images were acquired using an isotropic voxel resolution of 2.72 μm, with every scan taking approximately 4 h. Using the software NRecon, from Bruker, we reconstructed the 3D geometry of selected cuboid regions in the lung parenchyma, with an edge size of 0.5 mm. A three-dimensional view of the image reconstruction can be seen in Figure 2-3.

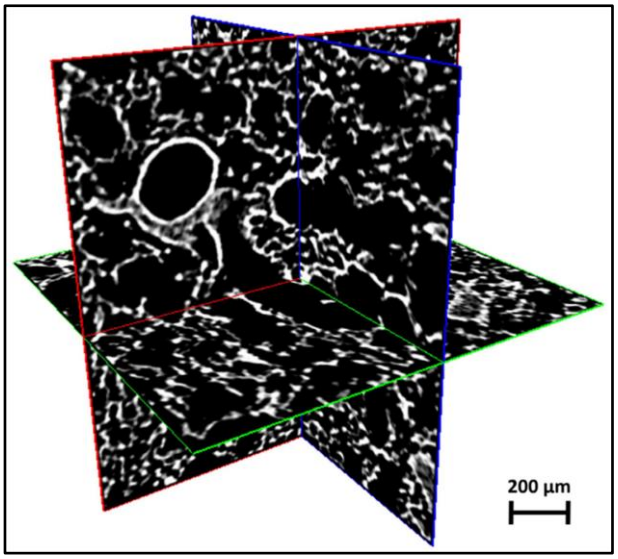

Figure 2-3. Three-dimensional reconstruction of lung parenchyma from μ-CT images.

Cuboid RVEs with an edge size ranging from 150 to 200 μm were selected from the whole-lung μ-CT images, considering regions that did not include portions of the main airways or large bronchi. Six samples were selected for the lung fixed at 10 cm H_2O, and another six samples were defined for the lung inflated at 20 cm H_2O. Reconstructed images of lung parenchyma RVEs were discretized with 10-node tetrahedral elements using the software ABAQUS version 6.14 to create a FE model of each RVE, see Figure 2-4(a) for a representative RVE mesh view. Since different RVEs displayed different microstructure, the

porosity, defined as the ratio between the volume of voids over the total volume, was determined for each sample. Tables 2-1 and 2-2 report the porosity, RVE size, and the number of tetrahedral elements in the RVE mesh for samples in the 10 cm H_2O and 20 cm H_2O cases, respectively.

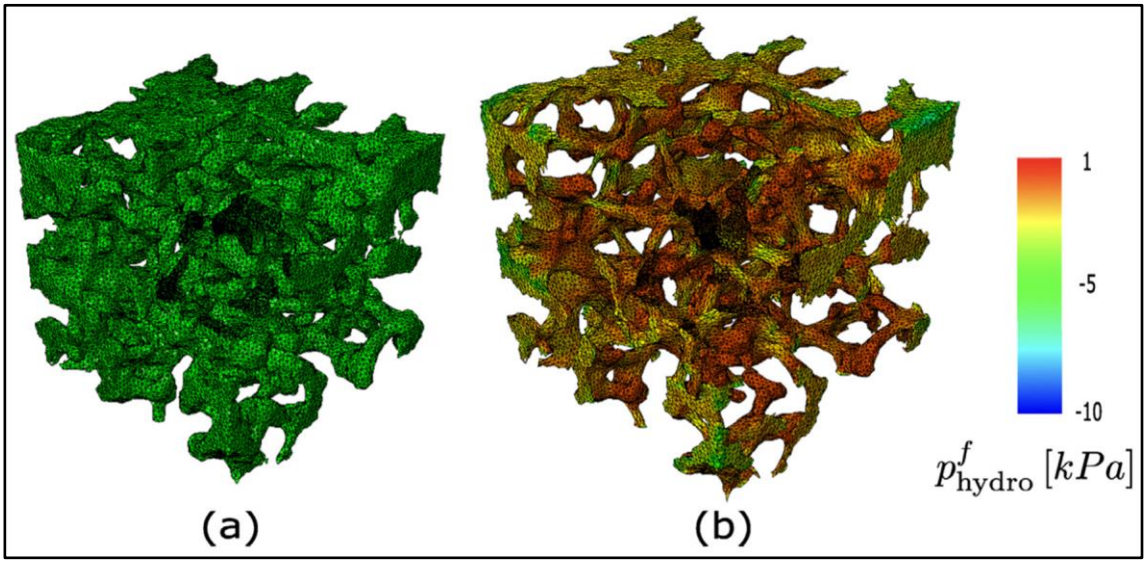

Figure 2-4. RVE FE model. (a) Tetrahedral mesh for sample S07 in the reference configuration. (b) Hydrostatic pressure distribution for S07, plotted in the current configuration.

An incompressible Neo-Hookean material model was assumed for all RVE models, with a Lamé constant set equal to μ = 1.66 kPa according to the experimental values reported in (Cavalcante et al., 2005). A mixed displacement-pressure (u−p) formulation was considered for all simulations using P2-P0 tetrahedral elements, to avoid volumetric locking. Displacement boundary conditions were prescribed at the boundary of RVEs, with displacement values determined from the imposed coarse-scale deformation-gradient tensor as dictated by Eq. (2.11). The coarse-scale deformation gradient $\mathbf{F}^C$ was assumed to take the principal stretch (diagonal) form of Eq. (2.23). Four different loading conditions were analyzed: isotropic expansion, anisotropic expansion, equibiaxial stretching, and uniaxial stretching. In all cases, simulations using a monotonically increasing loading pattern were performed. Table 2-3 reports the values for the maximum principal stretch values reached in simulations. The isotropic expansion case corresponds to a volumetric dilation of 250%,

which can be observed in normal human lungs under forced inspiration (Hurtado et al., 2017). The anisotropic expansion case also corresponds to deformation levels observed in normal human lungs under forced inspiration, where anisotropic deformation has been quantified in terms of anisotropic indices (Amelon et al., 2011).

Table 2-1. RVE geometry and mesh information for lungs fixed at 10 cm H_2O.

	S01	**S02**	**S03**	**S04**	**S05**	**S06**
Porosity	0.64	0.65	0.65	0.64	0.65	0.65
RVE size [μm]	198.6	198.6	198.6	198.6	198.6	198.6
Number of elements	411,943	402,321	401,283	404,339	399,307	396,643

Table 2-2. RVE geometry and mesh information for lungs fixed at 20 cm H_2O.

	S07	**S08**	**S09**	**S10**	**S11**	**S12**
Porosity	0.72	0.72	0.71	0.73	0.71	0.72
RVE size [μm]	149.6	149.6	198.6	198.6	198.6	198.6
Number of elements	379,919	378,181	456,927	449,088	483,943	466,671

Table 2-3. Maximum stretch values for the different loading cases considered in RVE simulations.

Loading case	$\boldsymbol{\lambda_1^C}$	$\boldsymbol{\lambda_2^C}$	$\boldsymbol{\lambda_3^C}$
Isotropic expansion	1.35	1.35	1.35
Anisotropic expansion	1.70	1.30	1.00
Equibiaxial stretching	1.50	1.50	1.00
Uniaxial stretching	1.80	1.00	1.00

Non-linear finite-element analyses were performed for all combinations of RVEs and loading cases driven by $\mathbf{F}^C$, from which we determined the coarse-scale Cauchy stress tensor $\boldsymbol{\sigma}^C$ from the volumetric average of the fine-scale Cauchy stress tensor field, *i.e.*, Eq. (7). An example of the hydrostatic pressure distribution obtained in RVE simulations is shown in Figure 2-4(b), where stresses are shown in the current configuration for RVE sample S07 under isotropic expansion. Fine-scale hydrostatic pressure is defined as

$$p_{hydro}^{f} = -\frac{1}{3} tr(\boldsymbol{\sigma}^{f}) \tag{2.40}$$

2.4 VALIDATION AND SENSITIVITY OF THE MICROMECHANICAL MODEL

To validate the TKD micromechanical model proposed in Section 2.2, we first constructed averaged stress-stretch curves using Eq. (2.7), based on the numerical simulations of all the combinations of RVEs described in Tables 2-1 and 2-2 and loading conditions described in Table 2-3. For the micromechanical model, stress-stretch curves were computed for all combinations of inflation pressure and loading conditions. The value for the Lamé constant μ was taken to be the same as that employed in RVE simulations. The porosity f_0 was set equal to the average porosity of the RVE samples with the same inflation pressure. The bending stiffness parameter α and the overlap coefficient d were manually fitted to the RVE curves, where we allowed d to take on different values for the two levels of inflation pressure considered in this study. Table 2-4 reports the numerical values adopted for all the material and geometry constants needed for the micromechanical model. Figure 2-5(a) and Figure 2-5(b) shows the hydrostatic pressure vs. stretch curves under isotropic expansion for the 10 cm H_2O and 20 cm H_2O cases, respectively. Hydrostatic pressure is defined as

$$p^c_{hydro} = -\frac{1}{3} tr(\boldsymbol{\sigma}^c) \tag{2.41}$$

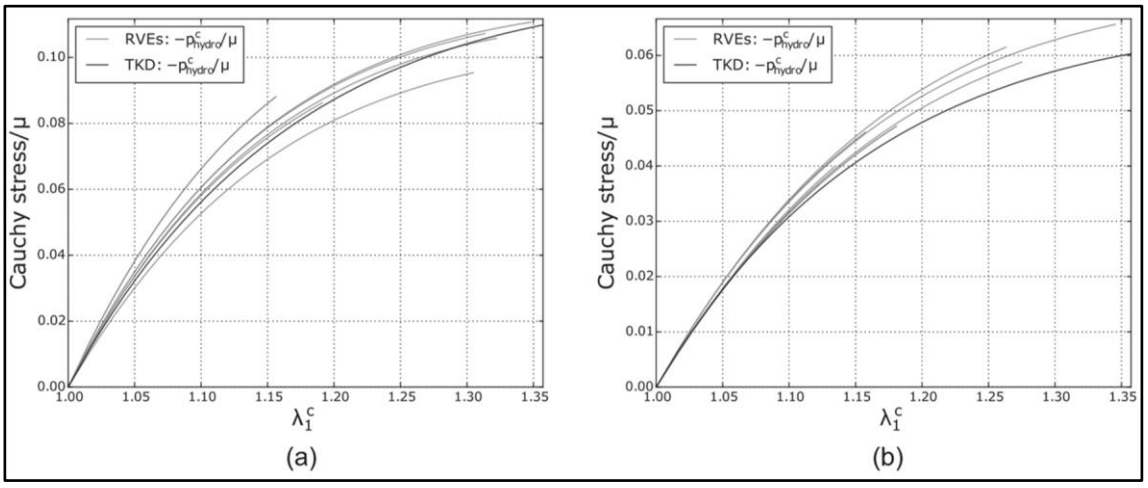

Figure 2-5. Normalized hydrostatic pressure versus stretch curves for the isotropic stretching case for inflation pressures of (a) 10 cm H_2O and (b) 20 cm H_2O. TKD micromechanical model response in solid lines, RVE response in markers, and shaded lines.

Table 2-4. Micromechanical model parameter values.

Parameter	Description	10 cm H_2O		20 cm H_2O
$\boldsymbol{\mu}$	Lamé constant		1.66 kPa	
$\boldsymbol{f_0}$	Reference porosity	0.65		0.72
$\boldsymbol{\alpha}$	Bending stiffness coefficient		6.0	
d	Overlap coefficient	0.70		0.42

Stress values are normalized by the Lamé constant, for the sake of comparison. For both cases of inflation pressure, we observe an excellent agreement between the TKD micromechanical model and the averaged RVE responses, with a small degree of variation observed between different RVE samples. In particular, the TKD micromechanical model can capture the non-linear behavior of the RVE model correctly. We note here that not all numerical simulations of RVEs were able to reach the final stage of deformation, as some were not able to converge despite the load-step adaptive refinement used in all RVE simulations.

The principal stress-stretch curves for the anisotropic expansion case are shown in Figure 2-6. For a fixed stretch level, we observe that principal Cauchy stresses take on different levels of stress magnitude, always following the ordering of the associated principal stretches. Good overall agreement is observed between the RVE average response and the micromechanical model, which can correctly capture the nonlinear response as well as the softening behavior observed as the stretch magnitude is increased. A similar situation is observed for the case of equibiaxial stretching, see Figure 2-7, and for the case of uniaxial stretching, see Figure 2-8. In the latter, we observe a less accentuated softening effect for the axial stress component $\boldsymbol{\sigma}_{11}^{C}$.

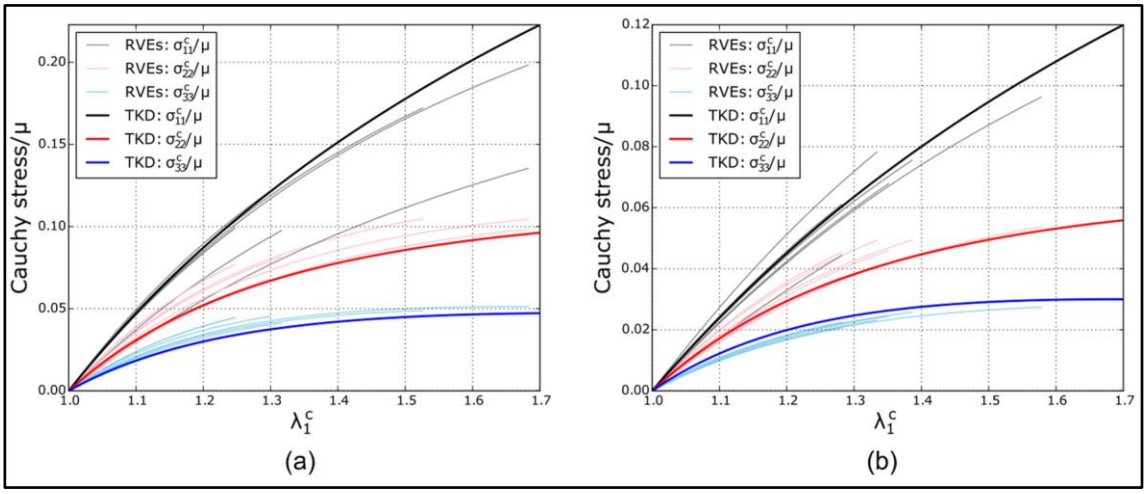

Figure 2-6. Normalized stress versus stretch curves for the anisotropic stretching case for inflation pressures of (a) 10 cm H_2O and (b) 20 cm H_2O. TKD micromechanical model response in solid lines, RVE response in markers, and shaded lines.

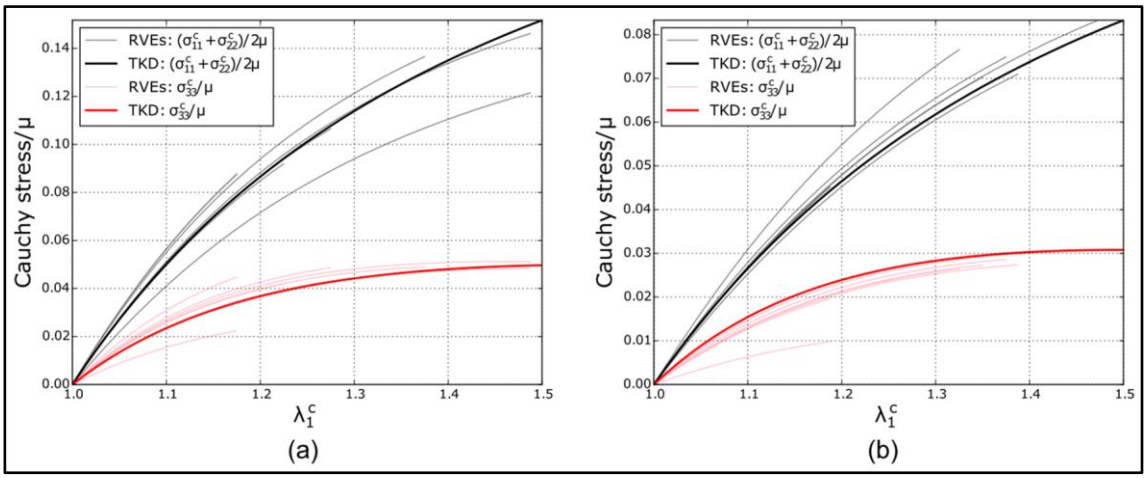

Figure 2-7. Normalized stress versus stretch curves for the biaxial stretch case for inflation pressures of (a) 10 cm H_2O and (b) 20 cm H_2O. TKD micromechanical model response in solid lines, RVE response in markers, and shaded lines.

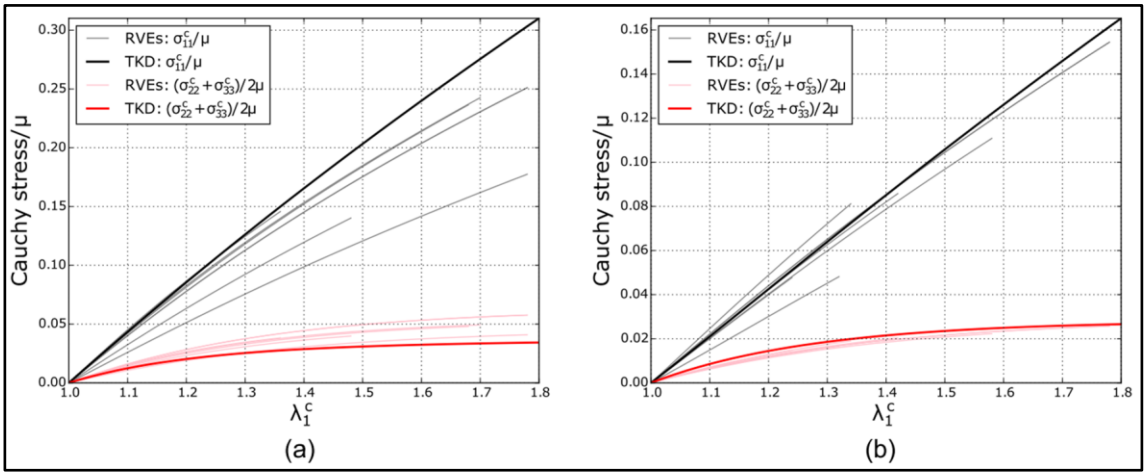

Figure 2-8. Normalized stress versus stretch curves for the uniaxial stretch case for inflation pressures of (a) 10 cm H_2O and (b) 20 cm H_2O. TKD micromechanical model response in solid lines, RVE response in markers, and shaded lines.

To validate the TKD micromechanical model against experimental data in murine lung tissue, we considered the stress-strain curves obtained from uniaxial loading tests reported by Cavalcante and co-workers (Cavalcante et al., 2005). Since the porosity of the lung tissue samples was not reported, we fitted this parameter to the data available, obtaining $f_0 = 0.66$, and considered the associated overlap coefficient $d = 0.70$ for that porosity level (Table 2-4). Figure 2-9(a) shows the experimental and predicted stress-stretch curves, where an excellent agreement is readily observed. In particular, the TKD model captures the slight stiffening observed in the mechanical response of the lung sample for the range of stretch reported. Figure 2-9(b) shows the evolution of the transverse stretch versus the axial stretch, as predicted by the TKD model, showing the Poisson effect is typically observed in uniaxial experiments of biological tissue. From our results, we estimate the average Poisson ratio to be $\nu = 0.22$. In order to assess the impact of the structural parameters μ, f_0, α, and d on the response of the TKD micromechanical model, we carried out a parameter sensitivity analysis. To this end, we focused on the isotropic stretching case and performed calculations for a set of parameter values that included variations of ± 5% and ± 25% around one parameter at the time, using as a baseline the parameters in Table 2-4 for the 20 cm H_2O case. The resulting stress-stretch curves are reported in Figure 2-10. We observe that the most influential parameter on the stress-stretch response is the reference porosity, with

higher values of f_0, resulting in a markedly softer response of the TKD model. The second most influential parameter is the Lamé constant, for which a stiffer TKD response is obtained as μis increased. In contrast, we note from Figure 2-10(c) that the TKD response is insensitive to variations of the bending coefficient parameter α for variations around the baseline up to 25%.

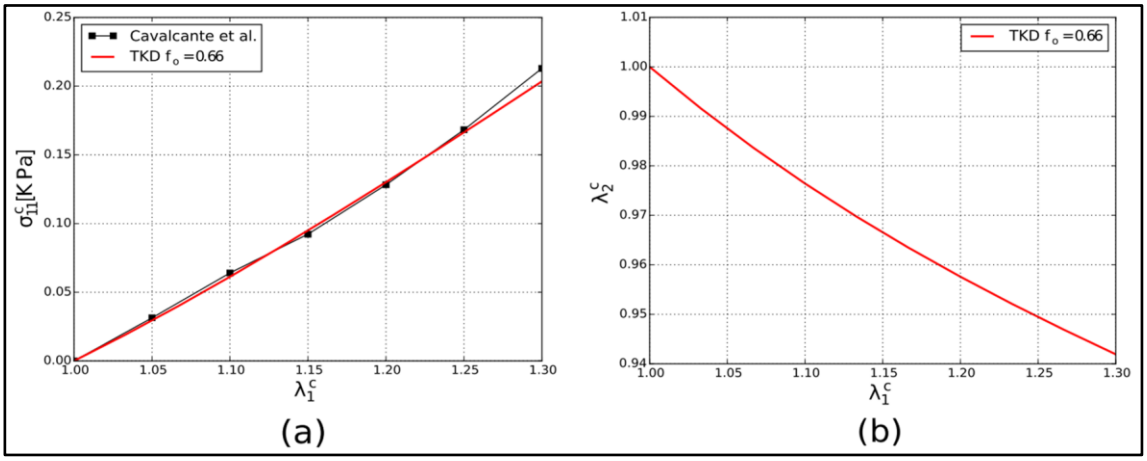

Figure 2-9. Uniaxial loading test (stress-free in the transverse direction) in murine lung tissue: (a) Uniaxial Cauchy stress versus stretch ratio curve from experiments (Cavalcante et al., 2005) and TKD model predictions. (b) Lateral stretch ratio versus uniaxial stretch ratio curve, displaying the Poisson effect, as reported by the TKD model.

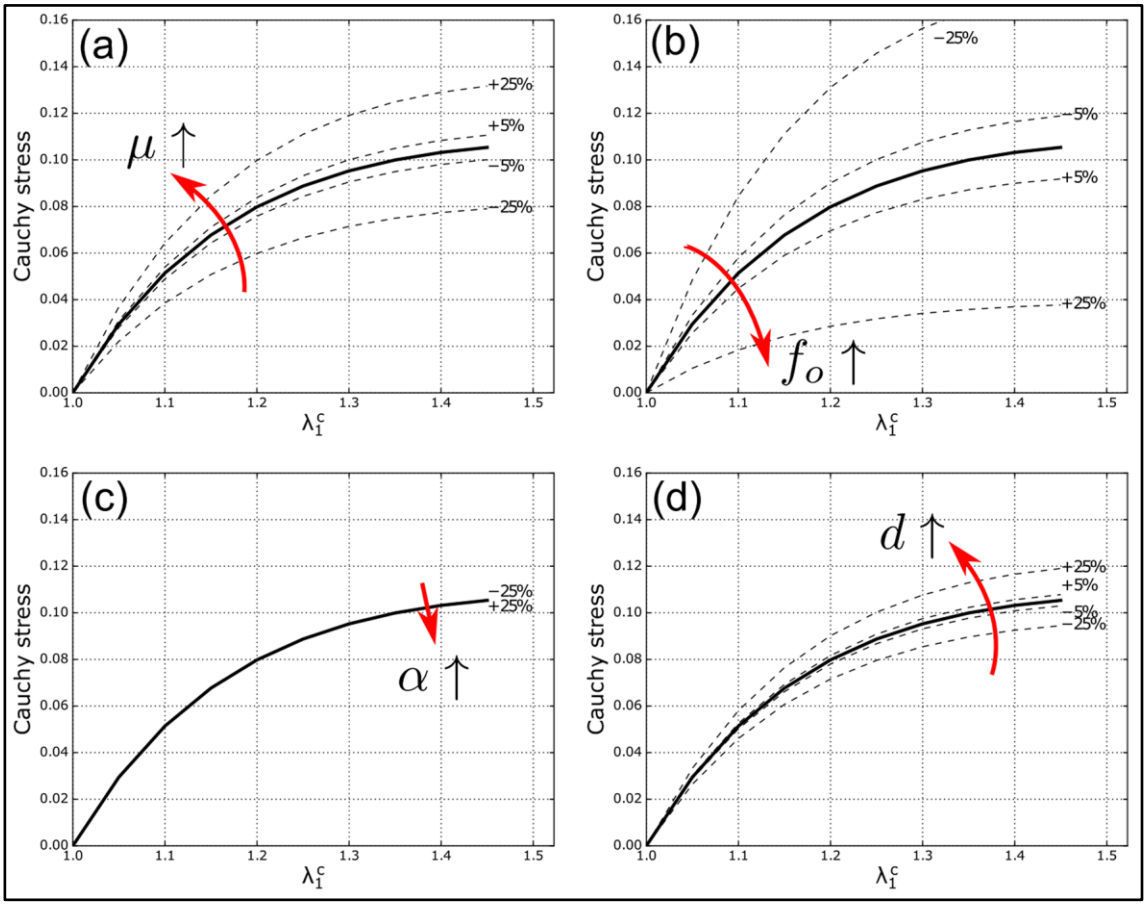

Figure 2-10. Parameter sensitivity analysis: Normalized stress-stretch curves for the isotropic stretching case varying (a) the Lamé elasticity constant μ, (b) the reference porosity f_0, (c) the bending stiffness coefficient α, and (d) the overlap coefficient d.

2.5 DISCUSSION

Our results confirm that the proposed TKD micromechanical model successfully captures the hyperelastic mechanical response, as predicted by RVE direct numerical simulations of the lung parenchyma, in isotropic, anisotropic, equibiaxial, and uniaxial stretching, in the range of moderate-to-large deformations, see Figure 2-5, Figure 2-6, Figure 2-7, and Figure 2-8. In particular, the TKD model was able to reproduce important mechanical features such as the marked non-linear constitutive response predicted by RVE simulations, including the evolution of tissue softening. While dispersion is observed in the response of different RVEs, the TKD model can deliver stress-stretch curves that are representative of the average behavior of all RVEs. We believe that a key ingredient of our micromechanical model is the consideration of the TKD geometry as the underlying unit cell, which despite being an

idealized geometry, adequately represents, in an overall sense, the three-dimensional microstructure of lung parenchyma, as suggested by Fung almost 30 years ago (Fung, 1988). The proposed TKD model involves only four parameters, two of which are directly related to measurable physical and mechanical properties of the alveolated tissue, *i.e.*, porosity and alveolar wall elasticity, and therefore they are not subject to parameter fitting. A compelling result of the parameter sensitivity analysis is that porosity and alveolar wall elasticity, in terms of the Lamé constant, are, in fact, the two most influential parameters in the mechanical response of the TKD model. These observations highlight the potential of the TKD model to enable truly multiscale simulations, as key microstructural mechanisms and structural parameters identified in the TKD model can be directly informed from micromechanical measurements. It is worth mentioning that such a sensitivity study is prohibitively expensive to perform based on the DNS of RVEs. The remaining two structural parameters were determined from fitting, but can also be related to microstructural features of the lung parenchyma, namely the bending stiffness coefficient and geometrical features of the alveolar wall. Remarkably, with only two free parameters we were able to capture the response of all three principal stresses under four different loading cases for moderate-to-large deformation levels, which highlights the potential of the TKD model to predict lung parenchyma elastic response under different loading conditions.

The TKD model is also able to reproduce the experimental data reported by Cavalcante and co-workers (Cavalcante et al., 2005) in murine lung samples under uniaxial loading with great accuracy, see Figure 2-9. This observation includes the slight stiffening observed for uniaxial stretch values up to 1.3. An analysis of the associated transversal deformation predicted by our TKD model delivers an average Poisson ratio of $\nu = 0.22$. While the Poisson ratio was not reported in (Cavalcante et al., 2005), we note that other authors have reported Poisson ratio values in the range of $0.2 - 0.4$ for murine and canine lung samples (Sophie M K Rausch, 2012; J. B. West & Matthews, 1972). It is worth remarking that, in many cases, the estimation of the Poisson ratio has relied mostly on parameter fitting of isotropic phenomenological models through inverse analysis of images, which delivers a wide range of markedly different values (A. Al-Mayah, Moseley, Velec, & Brock, 2009). It is also important to remark that our estimate for the Poisson ratio is based on experimental fitting rather than an image-based procedure, and assumes a micromechanical model that accounts

for the alveolar microstructure and its non-linear behavior.

We have previously mentioned that one advantage of micromechanical models based on homogenization theory was their ability to predict the effective mechanical response at a coarse level at a fraction of the computing effort of DNS. This work has not been the exception: the average computation time involved in the determination of coarse-scale stress-stretch curves using the RVE model and the TKD model was 12 h and 0.03 s, respectively, that is, seven orders of magnitude apart. These results can be explained by the number of DOFs each model considers: while RVE models have over two million DOFs, the proposed TKD model has only three. Clearly, this advantage can only be stated when it comes to coarse-scale properties and response, but it remains key when it comes to whole-organ multiscale simulations (Wiechert et al., 2011). In cases where the microstructure does not follow an idealized geometry, the DNS remains the only feasible approach. However, here we show that the TKD geometry idealization is sufficient for representing the lung parenchyma microstructure in overall terms. Another advantage we have observed in the course of this investigation concerns the stability of computations. In several cases, RVE simulations could not converge for moderate levels of deformation for numerical reasons. Typically, such failure to converge was associated with a few elements that underwent very large deformations. While remeshing was adopted in such cases, which allowed for larger stretching levels, stability issues still arose as the load was increased. Such stability issues were not found in solving the TKD model under the loading conditions reported here. We did, however, observe stability issues for compressive loading conditions in both the RVE and TKD models, which are the focus of current investigations.

An important contribution of our work is the simulation of twelve realistic lung parenchyma RVEs with micrometer dimensions under four different loading cases. For the particular loading case of isotropic stretching, we were able to study the evolution of coarse-scale stresses $\sigma_{11}^{C}, \sigma_{22}^{C}, \sigma_{33}^{C}$ for two levels of inflation pressure, see Figure 2-11. Our results reveal that the stress response of RVEs to isotropic deformation is not necessarily isotropic and that stresses along the principal directions of deformation can differ by up to twofold in magnitude in some cases, independently of the porosity. These findings question the validity of the isotropy assumption long accepted by the community, which is also an underlying assumption of the TKD model presented here, thus representing a limitation of virtually all

constitute models of lung parenchyma not based on DNS presented to date. Further, the anisotropic response of RVEs observed in our numerical studies strongly justifies the need for validating constitutive models using not only isotropic expansion tests (*e.g.*, pressure-volume curves) but necessarily for anisotropic loading conditions, as we have done for the TKD model. Future studies should assess the relevance of the anisotropy of lung parenchyma in multiscale simulations when predicting macroscopic lung behavior, which may justify the characterization of microstructural features that are responsible for such anisotropic nature.

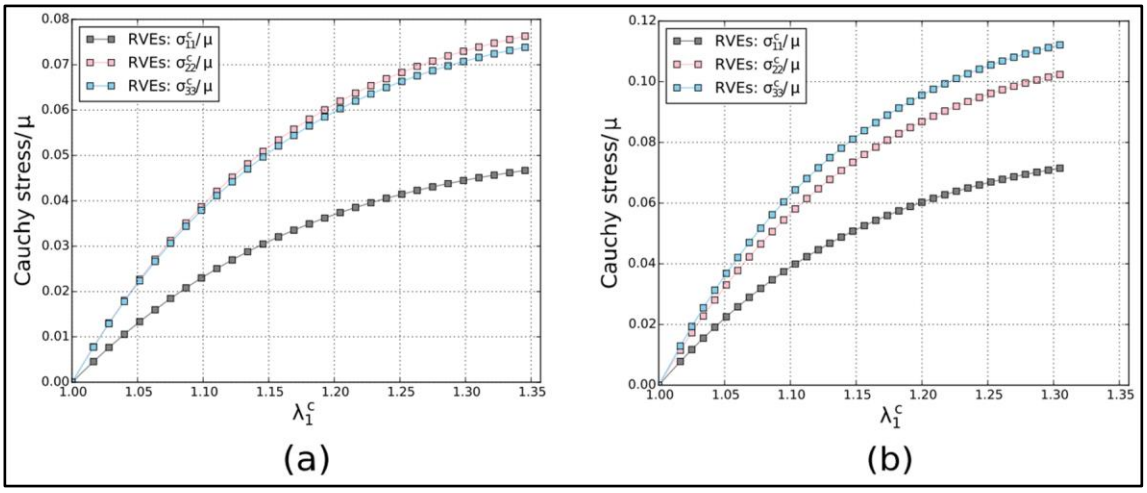

Figure 2-11. Normalized stress versus stretch curves for the isotropic stretching case in RVE models for inflation pressures of (a) 10 cm H_2O (S04) and (b) 20 cm H_2O (S09).

The TKD model presented in this chapter suffers from certain limitations. In this work, we have focused on the hyperelastic response of lung parenchyma. However, the mechanical response of the lung under physiological conditions also displays an inelastic rate-dependent response due to the hysteretic nature of the surfactant lining the alveolar walls, as well as the viscoelastic behavior of connective tissue and alveolar cells (John B. West, 2012). Future studies building upon the micromechanical framework presented here should include hysteresis and viscoelasticity, two phenomena that have been accounted for non-linear homogenization schemes in the past (Lahellec & Suquet, 2007). Another significant limitation of this work is the absence of prestress in modeling alveolated tissue. It is currently well established that prestress in the alveolar wall is responsible for the stability of the lung parenchyma in physiological conditions and particularly when subject to compression, as it balances out the collapsing effect due to surface tension (Mead et al., 1970). Future studies

should focus on estimating the alveolar wall prestress, which can be incorporated in the TKD model by considering a pre-stress term in the constitutive model for the rod elements. Another limitation of this study concerns the use of an incompressible Neo-Hookean model for the alveolar wall, which does not capture the exponential hardening observed in the parenchymal lung tissue for significant levels of deformation (Zeng et al., 1987). We note, however, that the main advantage of an incompressible Neo-Hookean model is the fact that it only needs one material parameter, namely the shear modulus μ, which is easily related in the limit of small deformations to standard material parameters measured from mechanical experiments. Further, the assumption of a Neo-Hookean material model proved to be very good in capturing the homogenized response at the coarse-scale for the moderate levels of deformation reported in this study.

In conclusion, we have introduced a novel micromechanical model for the hyperelastic response of the lung parenchyma that captures the tissue-level response in an efficient manner. The direct consideration of microstructural parameters in the model, such as the porosity and the alveolar wall elastic modulus, may have significant consequences in understanding the function of the lung in healthy and diseased conditions. For example, in the lungs with pulmonary emphysema, the alveolar wall is destroyed, which results in a reduction of the elastance of the lung parenchyma (John B. West, 2012), in terms of stiffness and stress levels. From a modeling perspective, the alveolar wall destruction can be interpreted as an increase in the lung tissue porosity, for which the TKD model does predict a softer response, as revealed by our sensitivity analysis for f_0 reported in Figure 2-10(b), which is in complete agreement with the reduction of elastance in emphysematous patients. Future extensions of this work should focus on exploiting the predictive capabilities of the TKD model in understanding other lung diseases that fundamentally affect the mechanics of alveoli.

3. CHAPTER II: THE ROLE OF THREE-DIMENSIONALITY AND ALVEOLAR PRESSURE IN THE DISTRIBUTION AND AMPLIFICATION OF ALVEOLAR STRESSES

3.1 INTRODUCTION

The biomechanical behavior of pulmonary alveoli, the basic ventilatory unit of the lung, plays a fundamental role in the respiratory physiology of mammalians. Comprising over 70% of the lung volume, alveoli are constantly stretched by parenchymal internal stresses to accommodate the inspired air, to later expel air out of the lung by elastic recoil during deflation (John B. West, 2012). During such ventilatory cycle, alveoli undergo dynamic states of stress, defined as the force acting on a unit area of tissue, as well as strain, which is a measurement of local deformation of the tissue. These mechanical changes at the level of the extracellular matrix have long intrigued lung physiologists and pulmonologists, as they dictate the overall lung mechanical behavior (Suki & Stamenović, 2011). More recently, the determination of stresses in the alveolar septal wall has gained great relevance due to the mechanobiological role of stresses in lung remodeling and pathogenesis, particularly in the case of pulmonary emphysema (Suki et al., 2013). A pioneering study in the field of lung mechanics is the work by Mead and collaborators (Mead et al., 1970), where fundamental mechanical principles are enforced in a simplified representation of the lung parenchymal tissue to analytically explain how alveolar volume and stresses are related to transpulmonary pressure and tidal volume. An important conclusion was that lung inhomogeneity, interpreted as abrupt changes in the configuration and internal pressure of one alveolar unit embedded in an otherwise uniform parenchymal structure, leads to a stress amplification in the walls of the neighboring units. The concepts of lung inhomogeneity and the associated local stress amplification have recently attracted great attention by the intensive-care medicine community, as the existence of highly localized levels of stress in alveoli is currently considered as one of the main determinants of ventilator-induced lung injury (Cressoni et al., 2013; Slutsky & Ranieri, 2013). Further, there is wide clinical consensus that organ-level deformation measures are not discriminant enough to detect the early-stage

onset of harmful pulmonary conditions during mechanical ventilation therapy (Dreyfuss & Hubmayr, 2016), which has motivated the development of novel regional tissue biomarkers that can better represent the effect of mechanical ventilation on the strains and stresses acting on lung tissue (Hurtado et al., 2016; Retamal et al., 2018).

The determination of stresses in alveolar walls remains an outstanding technological challenge. Current methods rely on the mechanical analysis of *ex-vivo* images of the lung parenchyma. Based on scanning electron microscopy images, Gefen *et al.* (Gefen et al., 1999, 2001) developed a finite-element model of a sample of murine lung tissue, whose underlying geometry was constructed from micrographs of alveolar sacs with enough resolution to resolve key histological features. By imposing static equilibrium in the continuum domain representing the alveolar sac under different levels of alveolar pressure, they were able to resolve the deformed state and the stress distribution in the sample, concluding that local stresses can concentrate in localized regions of the parenchyma, a phenomenon that is amplified in emphysematous lungs. Dynamic images of isolated perfused rat lungs have also been used to study the relation between transpulmonary pressure and alveolar perimeter distension by using confocal fluorescence microscopy (Perlman & Bhattacharya, 2007; Wu & Perlman, 2012). Based on a similar imaging technique, estimates of septal stress, strain, and elastic modulus were obtained for subpleural regions of the lung (Perlman, 2014). To this end, the alveolar sacs were idealized as a network of non-linear springs representing the alveolar septum. One important limitation shared by most investigations to date is the two-dimensional (2D) nature of the acquired images, which neglects the out-of-plane geometry and mechanics of the alveolar sacs. As a consequence, the associated mechanical analysis requires the assumption of out-of-plane conditions, either of the plain-stress or plain-strain type, neither of which are truly representative of the stress state in the lung parenchyma, which is inherently three-dimensional (3D). Another key shortcoming is the use of spring (axial) elements to model the alveolar septa. By definition, spring elements can only carry uniform uniaxial stresses, neglecting cross-section gradients in the normal stresses, as well as the transversal stress arising from the application of the alveolar pressure on the surface of alveolar walls, thus limiting the accuracy of the stress analysis.

μ-CT has enabled the morphological study and volumetric reconstruction of the acinar architecture with high fidelity in a less invasive way than traditional histological techniques (Langheinrich et al., 2004; Dragos M Vasilescu et al., 2012). The possibility of reconstructing 3D images of the lung with micrometer resolution has motivated several morphometric studies, where the lung parenchyma of rodents has been characterized in terms of airspace volume, equivalent diameter and surface-to-volume ratio, enhancing and correcting the previous knowledge purely based on 2D histological analyses (Parameswaran et al., 2009; D. M. Vasilescu et al., 2012). Spatial 3D representations of the pulmonary acinus constructed from μ-CT have also been reported in the literature, where tetrahedral meshes have been constructed from μ-CT images to visualize and study the intricate alveolated 3D architecture of acini (Tsuda et al., 2008). Such geometrical representation of the acinus has motivated the development of structural models of the lung parenchyma through 3D continuum FE simulations (Concha, Sarabia-Vallejos, & Hurtado, 2018; S. M K Rausch, Haberthür, et al., 2011; Roth, Yoshihara, & Wall, 2017), which have allowed for a detailed account of the distribution of local strains in the alveolar walls of a rat acinus sample. These *in-silico* experiments prescribed a uniform displacement field on the system boundary that was associated with arbitrary uniaxial elongation and simple shear deformation applied to the domain boundary, to determine, in a continuum fashion, the strain distribution in the alveolar walls of the sample under simplified loading conditions. One key conclusion from these 3D numerical simulations is that local strain can be highly heterogeneous in the alveolar-wall sector, which confirms the conclusions reached by previous 2D *in-silico* studies. In particular, strain concentrations with amplitudes up to four times the average strain were found in the analyzed samples (S. M K Rausch, Haberthür, et al., 2011). While these findings provide key insights on the 3D deformation of acinus under idealized boundary conditions, an accurate and complete study of the 3D stress distribution in the alveolar walls of acinus under realistic loading conditions remains open.

In this chapter, we thoroughly assess the fully 3D stress distribution in the alveolar walls of normal rat acini by determining the stress tensor field. We hypothesize that the consideration of 3D alveolar geometries and the use of continuum stress analysis on deformed configurations deliver 3D distributions of stresses that will enhance our current knowledge of the distribution and amplification of alveolar stresses, established predominantly from

previous 2D studies. To this end, we develop a combined experimental-computational technique to assess the 3D stress distribution in the alveolar walls of rat acini. We then characterize our results in statistical terms and contrast them to current alveolar stress states reported in the literature.

3.2 RESULTS

Morphometric analysis resulted in a surface-to-volume ratio of 94.48 ± 6.98 mm^{-1} for Low Alveolar Pressure (LAP) group, and 76.42 ± 6.24 mm^{-1} for the High Alveolar Pressure (HAP) group the porosity was 0.63 ± 0.02 and 0.7 ± 0.01 for the LAP and HAP groups, respectively (Supplementary material, Tables S 3-1 and S 3-2). The distribution of normalized stress components σ_{XX}, σ_{YY}, and σ_{ZZ} for a plane section of a representative sample of the HAP group is shown in Figure 3-1 for the linear and non-linear analyses. No appreciable differences are found between the stress distributions arising from linear and non-linear analysis. In all stress components, the spatial distribution is highly heterogeneous, and stress concentrations are found in localized regions of the alveolar domain. Interestingly, the σ_{XX} field shows positive values, which are associated with tension in the X−direction, in elongated regions that are aligned with the X−direction. Further, negative values of σ_{XX} are found in elongated regions aligned with the Y−direction, *i.e.*, orthogonal to the stress-component direction. An analogous trend is observed for the σ_{YY} field.

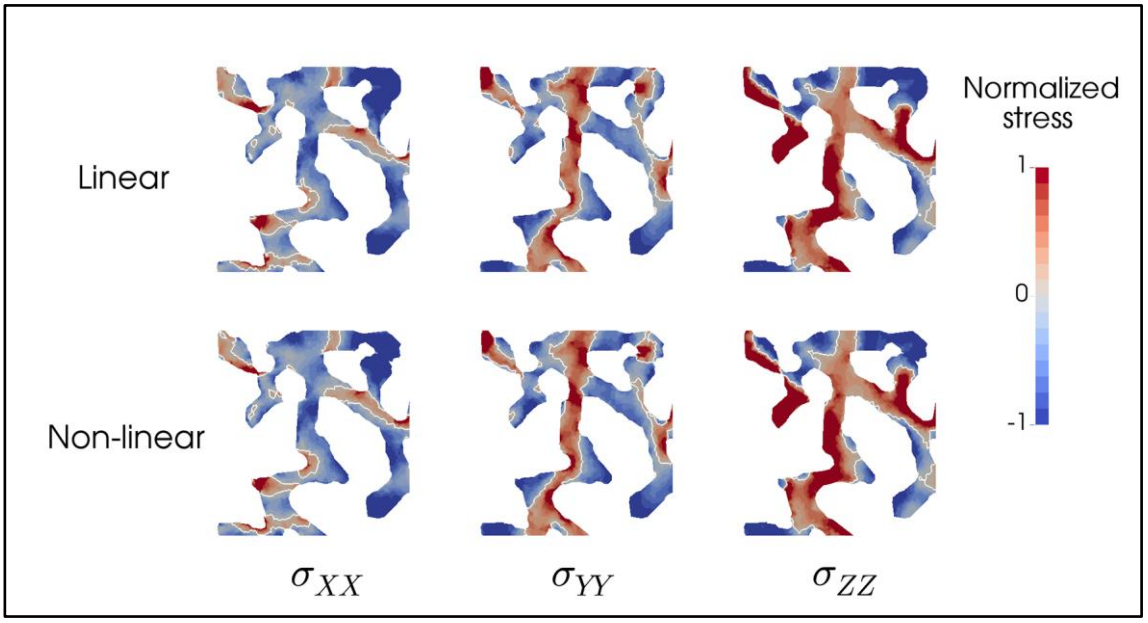

Figure 3-1. Normalized stress component fields in a section of a representative HAP sample (20 cm H_2O) for the linear and non-linear analyses. Regions of stress concentrations are observed throughout the samples, showing the high dispersion of stress levels.

The mesh-quality analysis showed that in all the meshes generated, 99% of the elements had a Joe-Liu parameter greater than 0.51 (Supplementary material, S 3-3(a)). The accuracy of the computational stress analysis was assessed through a numerical convergence study, which showed no appreciable differences in the von Mises stress distribution for meshes with approximately 750,000 elements when compared to a baseline fine-mesh simulation with 1,200,000 elements (Supplementary material, S 3-3(b)).

The stress distribution was found to be highly independent of the value of the elastic constants, as the von Mises stress frequency distribution did not change when increasing the Lamé constant by a factor of ten (Supplementary material, S 3-3(c)). Changes in the disposition of boundary conditions did not significantly affect the stress distribution (Supplementary material, S 3-3(d)). Three RVE sizes were tested, edge size L = 100, 250, and 500 μm, resulting in normalized von Mises distributions with mean values of 6.89, 7.08 and 8.87, respectively. No appreciable differences were found between the cases L = 100 μm and L = 250 μm. The case with L = 500 μm displayed a marked positive shift of the

mean value, which also resulted in a longer tail when compared to the smaller edge-size cases. The 95th percentile values were 16.18, 16.23 and 27.51 for the L = 100, 250, and 500 μm cases, respectively, which supports the observation of a larger tail in the distribution of the largest RVE.

The frequency distribution of the normalized hydrostatic stress in the LAP group displays a marked bimodal trend with peak values in the negative (−1.0) and positive (+0.67) ranges (Figure 3-2). The HAP group displays a clear peak on the negative range (−1.0), which coincides with the negative peak found in the LAP group (Figure 3-2). Frequency distributions for the von Mises stress in the LAP and HAP groups are reported in Figure 3-3. Clear unimodal and positively skewed distributions are observed for both groups. However, the LAP group displays a more concentrated and less skewed distribution than the HAP group which displays a heavier right tail.

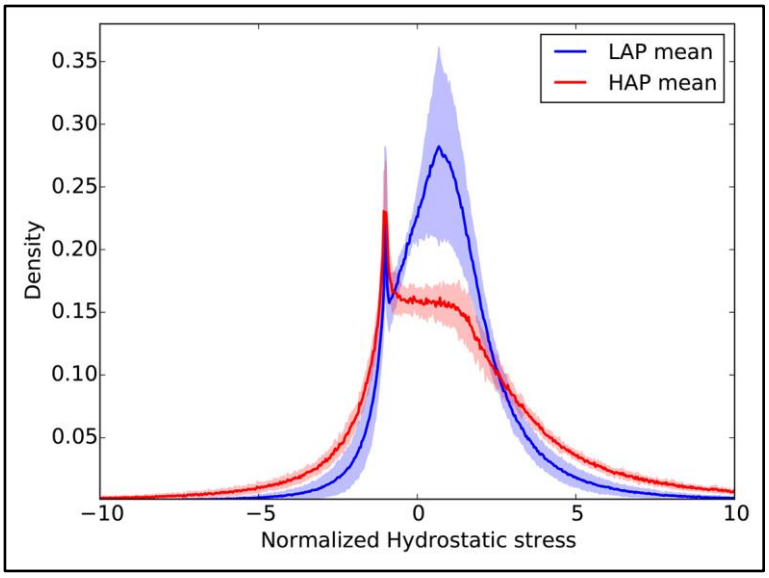

Figure 3-2. Frequency distribution of normalized hydrostatic stress for LAP and HAP group: Solid line shows the average group distribution. The lighter envelope shows the standard deviation of the group distributions. A bimodal shape is observed for the LAP group, while the positive peak is smeared in the HAP group.

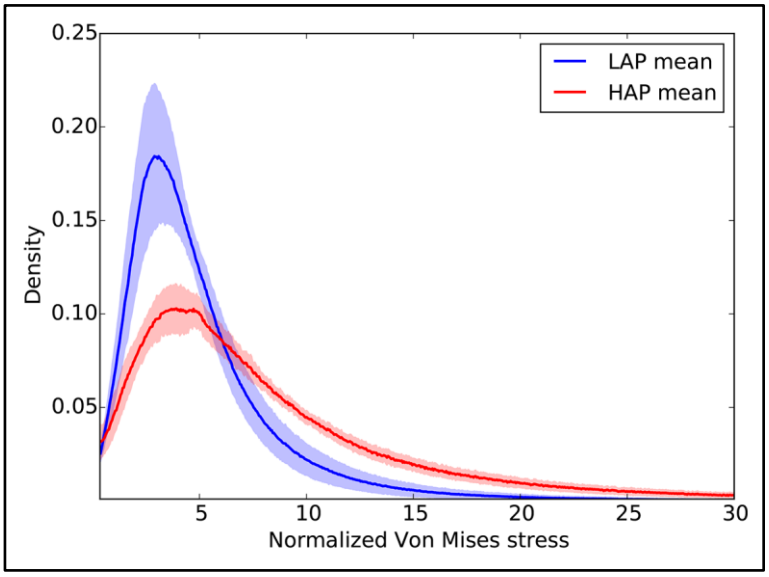

Figure 3-3. Frequency distribution of normalized Von Mises stress for LAP and HAP group: Solid line shows the average group distribution. The lighter envelope shows the standard deviation of the group distributions. Unimodal and positively skewed distributions were observed in both groups, with the HAP group displaying a higher dispersion in stresses than the LAP group.

To describe the heterogeneity of the stress measures in quantitative terms, the mean, mode, 5^{th}, and 95^{th} percentiles of normalized hydrostatic and von Mises stress measures for the LAP and HAP are reported in Supplementary material, Tables S 3-1 and S 3-2, respectively. We note that in the LAP group, the 95^{th} percentiles for the hydrostatic stress and von Mises stress were 4.5 × and 12.6 × the alveolar pressure, confirming that high-stress concentrations do arise in small regions of the RVEs. This effect is also observed in the HAP group, where the 95^{th} percentiles for the hydrostatic stress and von Mises stress were 8.4 × and 26.9 × the alveolar pressure. A comparison of group means values of normalized hydrostatic stress and normalized von Mises stress can be found in Figure 3-4. For both stress measures, the normalized stress values were found to be significantly different between the LAP and HAP groups.

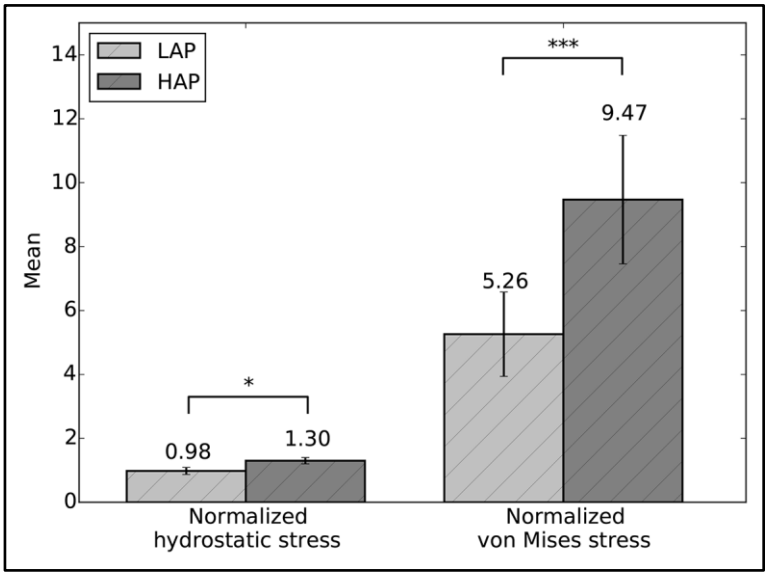

Figure 3-4. The effect of alveolar pressure on stress amplification: Comparison of group mean values of normalized hydrostatic and von Mises stresses between the LAP and HAP groups. Significant differences between groups were found for both stress measures studied. (*$p \leq 0.05$, **$p \leq 0.01$, and ***$p \leq 0.001$).

Alveolar stresses resulting from 3D stress analysis were significantly different from those obtained from the 2D analysis. The 2D normalized hydrostatic stress distribution was found to have a higher mode and more concentrated distribution than its 3D counterpart (Figure 3-5(a)). The distribution of von Mises stresses for the 2D case also resulted in a mode higher than that observed in the 3D case. Mean values for both stress measures were found to be significantly different between the 2D and 3D cases (Figure 3-6).

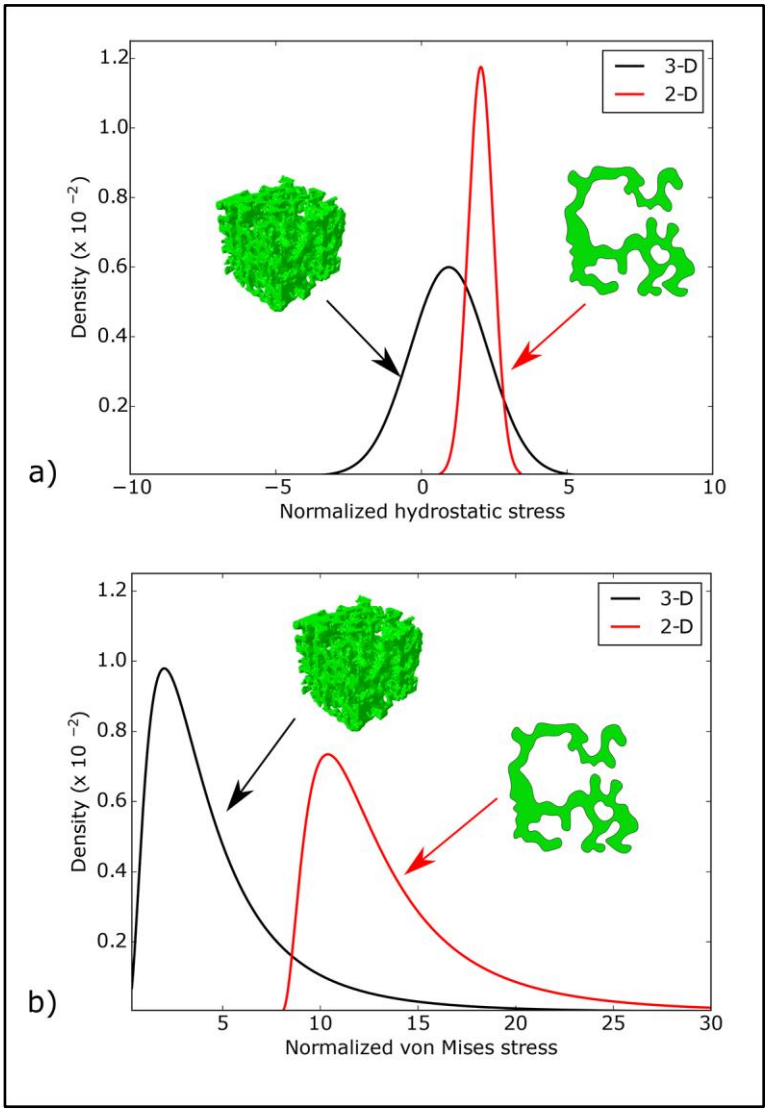

Figure 3-5. Difference between 2D and 3D analyses of alveolar stresses: Stress distributions for (a) normalized hydrostatic stress distribution, and (b) normalized von Mises stress distribution. 2D stress analysis consistently results in distributions with higher values than those obtained from 3D stress analysis, suggesting an overestimation of 2D methods.

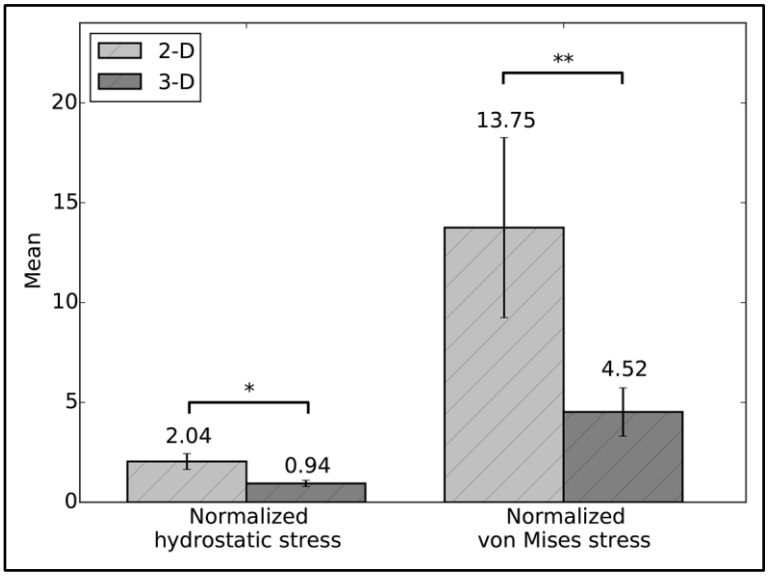

Figure 3-6. Difference in mean alveolar stresses between 2D and 3D analyses: Significant differences are found in alveolar stresses determined from 2D and 3D methods for both stress measures studied (*p≤0.05, and **p≤0.01).

3.3 DISCUSSION

In this chapter, we have assessed the 3D stress distribution in alveolar walls of rat lungs under high and low alveolar-pressure levels. While the estimation of alveolar strains and stresses has been the focus of several investigations in lung mechanics in the past (Gefen et al., 1999; S. M K Rausch, Haberthür, et al., 2011; Roth et al., 2017), the present work represents the first attempt to characterize alveolar stresses in statistical terms using realistic three–dimensional alveolar architectures under the effect of different levels of alveolar pressure.

One novel aspect of our work is the consideration of the fully 3D stress state in the alveolar wall, which is subject to realistic loading conditions acting on deformed configurations at different alveolar pressure levels. First, we note that the resulting stress tensor distributions do not significantly change when considering a non-linear constitutive relation, which supports our approach of using a linear elasticity model. Further, the stress distributions do not seem to be affected by global changes in the elastic modulus, neither by the disposition of the boundary conditions. These findings suggest that the stress tensor field in alveolar

architectures is predominantly statically determinate, *i.e.*, the stress tensor field largely depends on satisfying the differential equilibrium equations.

Another remarkable observation is that the stress component along the long axis of elongated subregions in the RVE tends to be under tension, while stress components orthogonal to this axis tend to be under compression, see Figure 3-1. Further, the magnitudes of tensile and compressive stresses are similar in range. Thus, we conclude that alveolar walls are subject to a multiaxial 3D stress state, with non-negligible levels of stress acting in directions that are orthogonal to the main direction of the tissue. This finding supports the need of fully 3D analyses when characterizing alveolar stresses, an approach that largely departs from the traditional consideration of the acinus as a network of spring (1D) elements that only carry axial stress (Cavalcante et al., 2005; Makiyama, Gibson, Harris, & Venegas, 2014; Mead et al., 1970; Perlman & Wu, 2014).

To facilitate the analysis of the distribution of stress in acinar geometries, we propose considering the hydrostatic and von-Mises stress measures of the stress tensor field, which correspond to dilatational and distortional deformation mechanisms, respectively. These stress measures have the advantage of being scalars that are invariant to changes of reference frames, and whose distribution in space can be analyzed in statistical terms (Hurtado et al., 2017). Our results show that the frequency distributions of hydrostatic and von Mises stresses cannot be represented by a normal distribution, highlighting the importance of characterizing statistical parameters other than the mean and standard deviation. Interestingly, we note that the shape of normalized stress frequency distributions depends on the applied alveolar pressure, as we observe that alveolar stresses in the HAP group result in distributions with heavier tails than those in the LAP group, *i.e.*, an increase of the applied alveolar pressure results in a larger spread in the stress magnitudes (Figures 3-2 and 3-3). This effect is further evidenced by the von Mises stress distributions when comparing the 95^{th} percentile of the normalized stress: 12.6× the applied alveolar pressure in the LAP group versus 26.9× in the HAP group. This dependence on the level of applied alveolar pressure also arises when comparing normalized mean stress magnitudes, both for hydrostatic and von Mises measures, which are in all cases significantly different (Figure 3-4). Therefore, we conclude that stress amplification in the alveolar wall cannot be characterized by a unique amplification factor, but should be related to the level of applied alveolar stress, this takes

particular relevance in lung physiology, where the concept of stress raisers in the lung tissue has been represented by an amplification factor that is independent of the level of transpulmonary pressure (Cressoni et al., 2013; Makiyama et al., 2014; Mead et al., 1970; Protti et al., 2011). An interesting avenue of research is to investigate potential changes in the composition of the underlying structural components that bear such high-stress concentrations (Toshima et al., 2004), as well as unveiling how stress concentrations drive remodeling processes in the extracellular matrix (Suki & Stamenović, 2011). Further, it is important to remark that the predominant structure carrying loads in the alveolar walls is the fiber network composed by elastin and collagen fibers embedded in the extracellular matrix (Mercer, Russell, & Crapo, 1994). Despite its relevance, the specific forces being carried by each of these structural components remain largely unknown. Future contributions should focus on how alveolar stress is resisted by these structures, which are known to protect the delicate blood-gas barrier formed by epithelial and endothelial cells, among other elements (Bachofen & Schürch, 2001).

Another novel conclusion of this work is that 2D mechanical analysis of acinar architectures tends to overestimate the stress level in alveolar walls. A direct comparison of the stress frequency distribution resulting from 2D and 3D evidences a positive shift towards higher values both for the hydrostatic and von Mises stresses (Figure 3-5), with mean values for the 2D case that are significantly larger than their 3D counterparts (Figure 3-6). The tendency to overestimate observed in 2D analysis can be attributed to the omission of out-of-plane stresses, which contribute to bearing the applied alveolar pressure and internal stresses mainly by membrane stresses. Thus they carry part of the total loading, resulting in a reduction of stresses for the in-plane stress components. This effect is readily seen when comparing the stresses generated by an internal pressure *p* acting on a thin ring (2D structure) and those arising in a thin hollow sphere (3D structure) under the same internal pressure. In the former, the resulting membrane stress is $\sigma_{ring} = \frac{pR}{e}$, whereas in the latter $\sigma_{sphere} = 0.5\,\frac{pR}{e}$, where *R* is the radius and *e* is the membrane thickness, from which we obtain that $\sigma_{ring} = 2 \times \sigma_{sphere}$, *i.e.*, a 2D analysis delivers a stress level that is twice the stress present in the 3D structure.

To further put our findings in perspective with previous results, we assume the case of an axial element under principal stresses, subject to axial stress σ_{ax} along the longitudinal direction, and to alveolar pressure p_{alv} in the transversal plane, see Supplementary material, S 3-4. From the definition of hydrostatic stress (6), we can rewrite the axial stress as

$$\sigma_{ax} = 3\sigma_H + 2P_{alv} \tag{3.1}$$

Using Eq. (3.1) we estimate equivalent axial stress from the distribution of hydrostatic stresses. We further note that in our case, lungs were scanned after being removed from the thorax cavity, which implies that, due to the absence of intrapleural pressure, the transpulmonary pressure (P_{tp}) is the same as the alveolar pressure (P_{alv}). Figure 3-7 shows the axial stress versus transpulmonary pressure obtained from this study, along with the results reported from 2D studies of alveolar stress (Gefen et al., 1999; Perlman, 2014). Once again, we observe that both 2D studies report stresses that are higher than those obtained from our 3D study, which is in line with our findings. Therefore, we conclude that the estimation of alveolar stresses is strongly influenced by the dimensionality assumed by the method of analysis and that the explicit consideration of the out-of-plane dimension will result in lower levels of alveolar stress, which can be considered closer to the actual stresses due to the explicit consideration of the three-dimensionality of the alveolar architecture. We note here that the results of Perlman and Bhattacharya (Perlman, 2014) correspond to air-filled subpleural alveolar structures, which poses essential differences in the experimental setup and the region inside the lung analyzed when compared to our methodology. While we expect that stress distributions will display variations depending on the position inside the lung and on the experimental settings, our study confirms a significant reduction of stress levels when the third dimension is explicitly considered in the mechanical analysis. This finding is paramount to future studies of lung disease mechanobiology, as stresses in the alveolar wall are believed to trigger remodeling processes in the lung tissue that give origin to respiratory diseases such as emphysema (Suki et al., 2013; Tschumperlin, Boudreault, & Liu, 2010).

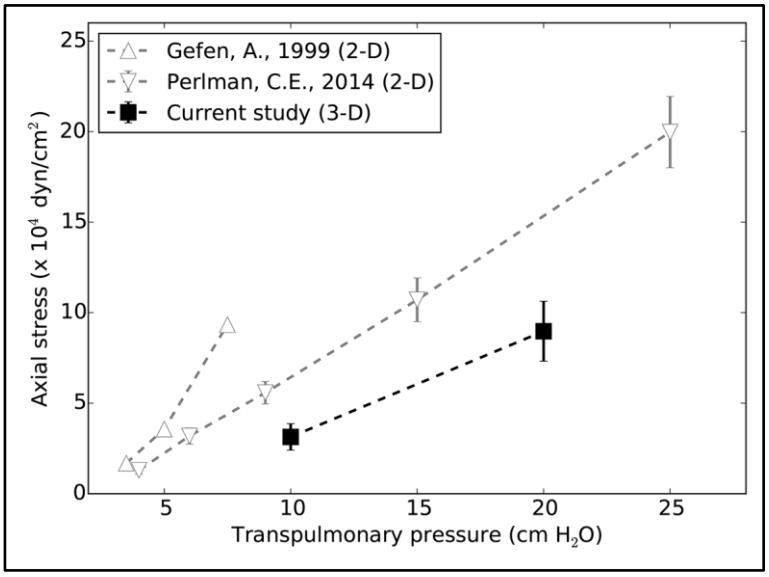

Figure 3-7. Axial stress in alveolar walls: Comparison of equivalent axial stresses computed from 3D analysis versus axial stresses determined from 2D methods reported in the literature.

Our work suffers from some limitations which we discuss next. During the construction of the finite-element models, the mechanical effect of the surface tension induced by the alveolar fluid was not included. Depending on the level of tidal volume, surface tension can result in additional stresses acting on the interalveolar septa (Gil, Bachofen, Gehr, & Weibel, 1979), a mechanical contribution that markedly impacts the global mechanics of the lung (Ghadiali & Gaver, 2008). During normal breathing, variations of surface tension can be small, and may not exceed a range of 5 mN/m. However, large volume changes induce large changes in the alveolar surface, which results in non-negligible variations in the surface tension, and therefore in the stresses that arise in the alveolar walls to resist surface tension (Bachofen & Schürch, 2001). Based on these observations, we remark that the stress distributions obtained in this work can be assumed to be accurate for the zero surface-tension limit, but necessitate corrections when the alveolar surfactant is present (Fujioka, Halpern, & Gaver, 2013). Future contributions should incorporate the effect of surface tension, which needs accurate information not only of the alveolar geometry and alveolar pressure but also of the surfactant concentration and adsorption-desorption kinetics (Otis, Ingenito, Kamm, & Johnson, 1994), which are currently challenging to assess *in-situ*. Another limitation of the

methodology is the formalin-based procedure employed for fixation, which is known to cause shrinkage and incomplete fixation of elastic fibers (Hsia, Hyde, Ochs, & Weibel, 2010). A parameter commonly used in assessing shrinkage of lung tissue samples is the alveolar surface-to-volume ratio, which in mice is in the range of 50–100 mm^{-1} for the C57Bl/6 J mouse (Kumar et al., 2013; Osmanagic et al., 2010; D. M. Vasilescu et al., 2012). The values obtained in this study fall in that range, as the average surface-to-volume ratios were 94.48 mm^{-1} and 76.42 mm^{-1} for the LAP and HAP groups, respectively.

3.4 METHODS

µ-CT imaging of rat lungs. The study protocol was approved by the Bioethics Committee of the Pontificia Universidad Católica de Chile. Healthy adult male Sprague-Dawley rats (256 ± 16 gr, N=6) were considered for this study. Animals were sacrificed according to the international guidelines given by the American Veterinary Medical Association (AVMA) (Leary et al., 2013). A tracheostomy procedure was performed to control lung formalin phosphate-buffered-saline (F-PBS) flow through a fixed cannula with a three-step valve to prevent fluid leaking. Animals were randomly allocated to either at the LAP group (N =3) or the HAP group (N =3). The F-PBS solution was slowly pumped through the cannula into the lungs until reaching the target airway pressure measured through a syringe with a pressure transducer (AG Cuffil, Hospitech Respiration Ltd.). Airway pressure was manually adjusted to target values and monitored for ten minutes, after which variations in airway pressure were below 0.1 cm H_2O within a time frame of 5 minutes. The animals were refrigerated overnight, maintaining the airway pressure constant by carefully stitching the trachea. After this first F-PBS fixation stage, lungs with trachea and cannula were carefully excised from the rat thoracic cavity, to then submerge them into an F-PBS solution for 24 hours (Parameswaran et al., 2009). Ten, the left lung was dissected and dried by following a desiccating process based on gradual ethanol baths (Bruker-MicroCT, 2016). Lastly, lungs were maintained in a 100% ethanol bath overnight (Dudak et al., 2016; Scotton et al., 2013). Previous to the scanning process, left lungs were left air drying at atmospheric conditions for 24 hours in order to evaporate the remaining ethanol.

Fixed lungs were scanned using a commercial μ-CT device (SkyScan 1272, Bruker). The X-ray source voltage and current were set to 10 kV and 250 μA, respectively. Whole-lung tomographic scans were acquired using an isotropic voxel resolution of 2.7 μm per voxel. 3D images of the lung were reconstructed using the NRecon software (Bruker), where misalignment compensation, ring artifact reduction, and hardening filters were employed to improve the image quality. 3D images were segmented using a multi-level thresholding procedure based on the Otsu method to isolate the lung parenchyma from surrounding organs, major vessels, and airways (Ford et al., 2014; Otsu, 1979). These values were in concordance with common tissue Hounsfield intensities. See Figure 3-8(a) for a representative μ-CT image.

Alveolar cubic samples, also termed here as RVE, with an edge size of 250 μm, were selected from image reconstructions of the left lung, resulting in 6 RVEs for the LAP group (airway pressure of 10 cm H_2O) and 6 RVEs for the HAP group (airway pressure of 20 cm H_2O). RVEs in the same group were chosen to have similar morphological parameters such as mean alveolar radius, surface-to-volume ratio, and porosity (Kumar et al., 2013; D. M. Vasilescu et al., 2012). Care was exercised in excluding regions that included portions of large bronchi, as well as avoiding zones close to the pleura and close to larger airways.

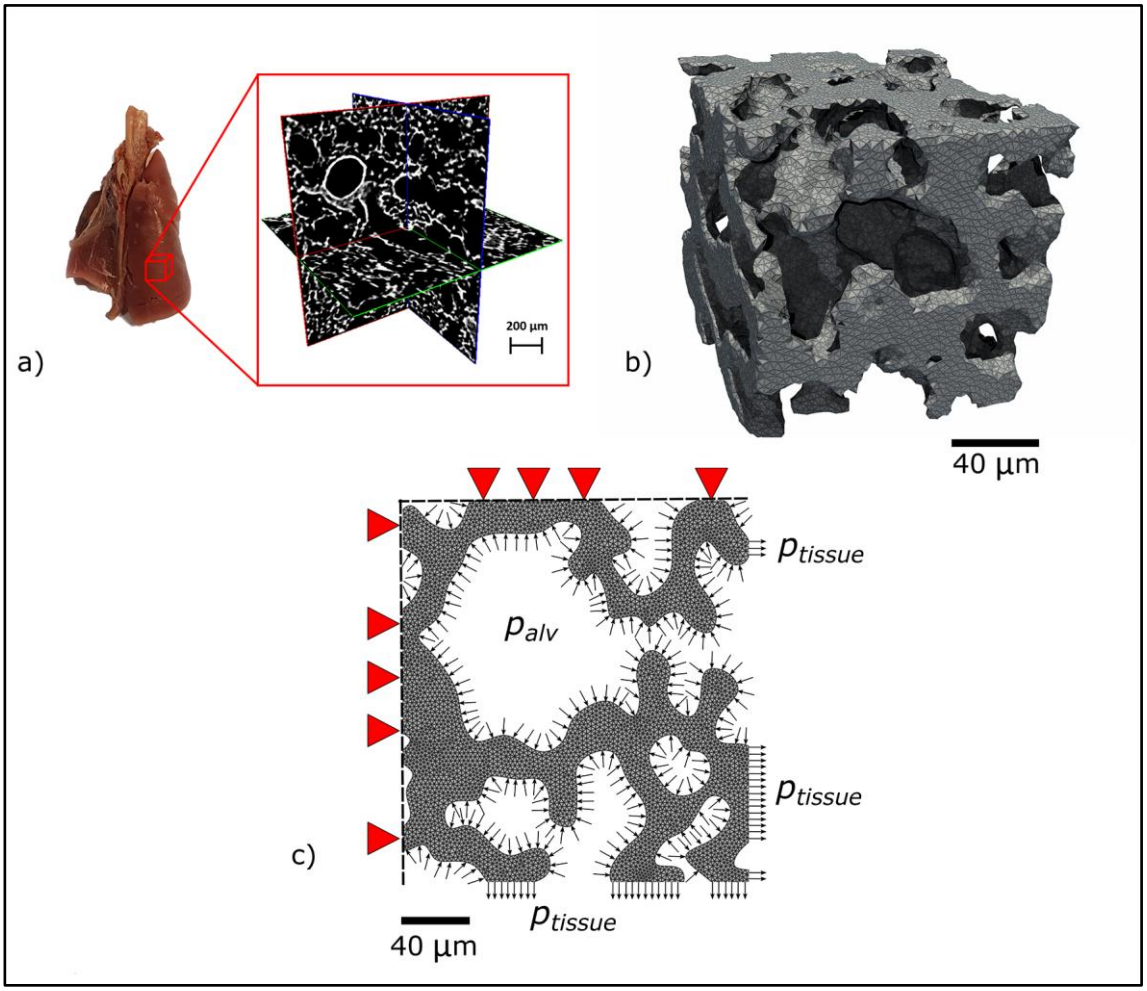

Figure 3-8. Generation of the computational model to assess 3D alveolar stresses. (a) Cuboid subdomains are selected from µ-CT whole-lung images to define the geometry of an RVE, avoiding larger airways in the sample to obtain mostly acinar tissue, (b) FE meshes are generated from acinar images to represent the alveolar architecture, (c) boundary conditions include alveolar pressures acting on the internal surfaces, displacement prescription on three bounding faces of the RVE, and orthogonal stress representing the tissue reaction acting on the remaining bounding faces of the RVE.

Figure 3-8(b) shows one representative RVE. Porosity, defined as the ratio between the air volume over the total volume of an RVE (including air and alveolar tissue) was assessed from the reconstructed masked images.

3D alveolar stress analysis. To determine the stress distribution in the alveolar walls, we considered an elasticity formulation for the alveolar tissue based on the geometry obtained

from μ-CT images. It is important to remark that alveolar stresses are in equilibrium in the deformed configuration, which in our case, is given by the acquired images. Therefore, we followed a spatial formulation of the elasticity problem, *i.e.*, the analysis was based on the deformed configuration of the tissue, which we denote by Ω. Under equilibrium, the 3D Cauchy stress tensor field σ is governed by the differential equilibrium equation.

$$div\ \sigma = 0\ in\ \Omega \tag{3.2}$$

We denote by μ the displacement field associated with the equilibrium configuration of the alveolar domain. To reduce the computational complexity of the finite-element model, we assumed a linear elastic response for the alveolar tissue. Further, we assumed the alveolar tissue maintains its volume, i.e., it behaves as an incompressible material. Under these assumptions, the constitutive law takes the form.

$$\sigma = -pI + 2\mu\varepsilon(u) \tag{3.3}$$

where μ is the elastic Lamé constant, p is the static pressure field, I is the identity tensor, and the infinitesimal strain tensor is defined as

$$\varepsilon(u) \coloneqq \frac{1}{2}\{\nabla u + \nabla u^T\} \tag{3.4}$$

We set the elastic modulus to E = 9.5×10^5 dyn/cm^2 following values reported in the literature (Perlman & Wu, 2014) and the Poisson ratio to v = 0.5, as we assume the extracellular matrix maintains its volume (incompressible material), which yields $\mu = \frac{E}{2(1+v)} = 3.17 \times 10^{\,5} dyn/cm^2$. To assess the accuracy of the linear elastic stress analysis, we also performed a non-linear finite-element analysis for one RVE case, and compared the resulting stress distributions with those obtained from linear-elastic analysis. To this end, we followed a non-linear hyperelastic formulation that allows for large deformations, and assumed that the alveolar walls behaved as an incompressible Neo-Hookean material (S. M K Rausch, Haberthür, et al., 2011).

Appealing to Pascal's law for incompressible fluids, and neglecting the effect of gravity, alveolar pressure (p_{alv}) was assumed to be equal to the pressure imposed at the airways in the experiments. Since lungs are scanned after being removed from the thoracic cage, intrapleural pressure is absent, and transpulmonary pressure can be assumed to be equal to the alveolar pressure. Alveolar pressure was applied to all surfaces exposed to air inside each RVE. Displacement boundary conditions were enforced in three orthogonal faces where zero

normal displacements were prescribed, while the remaining three bounding faces were subject to tractions representing the effect of the surrounding tissue, see Figure 3-8(c). To determine these tractions, we considered the net force equilibrium on each of the three bounding faces in the RVE independently. For a particular traction bounding face, let A_{tissue} be the area occupied by the intersection of the alveolar tissue with the bounding face, p_{tissue} be the pressure acting such tissue area representing the tractions exerted by the surrounding tissue, and A_{air} is the area of the boundary face intersected by airspace under alveolar pressure. Force balance on the bounding face implies that

$$p_{tissue} = p_{alv}\frac{A_{air}}{A_{tissue}} \tag{3.5}$$

Displacement boundary conditions were enforced in three orthogonal faces where zero normal displacements were prescribed, and uniform pressure with magnitude p_{tissue} was set as the boundary condition on each opposite face in the outward direction.

FE models were constructed using the software ABAQUS (Abaqus/CAE 2017, Dassault Systems Simulia Corp., Johnston, RI, USA). To this end, we first generated 3D tetrahedral meshes from the alveolar wall domain segmented in each RVE using the CGAL library (CGAL, 2018). The incompressible elasticity problem was approach using a mixed formulation, where P_2–P_1 Taylor-Hood tetrahedral (quadratic) elements were employed. Surface loads and boundary conditions were assigned accordingly. To assess the differences between 3D and 2D stress analyses, we performed a 2D FE simulation of a plane section obtained from a suitable RVE, assuming a plane-stress condition.

The stress distribution in the alveolar walls was studied using two classical scalar stress measures: (i) the hydrostatic stress, defined as the first invariant of the Cauchy tensor,

$$\sigma_H \coloneqq \frac{1}{3}trace(\sigma) \tag{3.6}$$

and (ii) the von Misses stress, defined as

$$\sigma_{VM} \coloneqq \sqrt{\frac{3}{2}\sigma_{dev}:\sigma_{dev}} \tag{3.7}$$

where: signifies the tensor scalar product, and the deviatoric component of the stress tensor reads

$$\sigma_{dev} \coloneqq \sigma - \sigma_H I \tag{3.8}$$

From definitions Eq. (3.6) and Eq. (3.8) we note that the hydrostatic stress and the Von Mises stress quantify two independent and orthogonal components of the Cauchy stress tensor, *i.e.*, the hydrostatic and deviatoric behavior, respectively. We also note that in isotropic solids, the hydrostatic stress can be related to changes in volume, whereas the deviatoric stress is related to shape changes.

To assess the numerical accuracy of the computational model, a mesh quality analysis based on the Joe-Liu parameter was performed (Liu & Joe, 1994), and histograms were constructed to check that the majority of elements had an acceptable parameter value. A numerical convergence analysis was also performed for one RVE case using a tetrahedral discretization with a total number of elements ranging from 70 k to 1200 k. The resulting stress distributions were contrasted through the resulting frequency distributions of the stress measures defined above. To assess the sensitivity of the stress analysis to variations in the elastic properties of the alveolar tissue, we studied the impact on the stress measure frequency distribution in one RVE case using a Lamé constant 10 × higher than the standard value adopted. The sensitivity of the stress distributions to the disposition of boundary conditions and the RVE domain size was also analyzed.

The resulting stress analyses were summarized in terms of relative frequency distributions of the two stress measures considered in this study. Stress measures were normalized by the applied alveolar pressure, to allow for a direct comparison of stress amplification and heterogeneity between experimental groups. Values are expressed as mean ± standard deviation unless noted otherwise. Significant differences between group mean values were assessed using the Mann-Whitney-Wilcoxon test for non-parametric distributions.

4. CHAPTER III: THREE-DIMENSIONAL CHARACTERIZATION OF THE REGIONAL ALVEOLAR MORPHOLOGY IN NORMAL LUNGS.

4.1 INTRODUCTION

Ventilation and perfusion are vital processes to facilitate gas exchange at the alveolar level, which is the primary function of the respiratory system. Pulmonary ventilation is defined as the process where air enters and leaves the alveolar units, which supplies with O_2 to the alveolus and removes the expired CO_2. Perfusion refers to the blood flow in the capillaries that surround the alveolar surface, which is fundamental for gas transport. The relationship between both processes is one of the cornerstones of respiratory physiology, as it not only allows us to understand the mechanisms underlying respiration but also explains the genesis and evolution of diseases such as hypoxemia and pulmonary emphysema, among others (Bajc & Jonson, 2011; Jögi, Ekberg, Jonson, Bozovic, & Bajc, 2011).

Ventilation and perfusion have long been associated with the alveolar architecture, constituting another clear example of the celebrated structure-function paradigm in physiology. To maximize gas exchange between alveoli and capillaries, the mammalian lung takes on a highly porous structure that maximizes the perfused alveolar surface and, at the same time, maximizes the alveolar airspace volume (Hsia, Hyde, & Weibel, 2016). Alterations in the balance between the alveolar surface and the alveolar airspace constitute the pathophysiological basis of chronic respiratory diseases such as pulmonary emphysema. In emphysematous lungs, the rupture of alveolar walls results in a marked decrease in the alveolar surface available for perfusion and gas exchange and in the loss of alveolar tissue recoil, ultimately deteriorating the respiratory function (Suga et al., 2010). This highlights the importance of characterizing the morphology of the alveolar tissue in the lung and elucidates how it influences lung function and pulmonary performance (Ewald R. Weibel, 2017).

From a morphological point of view, alveolar ventilation is associated with porosity, defined as the ratio between the volume of the alveolar cavity (airspace volume) divided by the nominal (reference) volume of lung tissue. Similarly, perfusion can be associated with

alveolar surface area density, defined as the ratio between the alveolar surface area over the nominal volume of lung tissue (Hsia et al., 2016). It is important to note that both definitions are independent of each other, as the alveolar cavity volume and surface are not necessarily related. Given its close relationship with the gas exchange process, the study of the spatial distribution of morphological parameters such as porosity and alveolar surface area density provides a quantitative evaluation that can be related to ventilation and perfusion with regional resolution (Clark, Burrowes, & Tawhai, 2019; Soldati et al., 2014).

To date, the quantification of alveolar morphology has been difficult due to its micrometric size and intricate architecture. Advances in micro-computed tomography (micro-CT) techniques have allowed the study of the shape and structure of pulmonary acini with high resolution and less destructively than traditional histological methods (Langheinrich et al., 2004; Dragos M Vasilescu et al., 2012). Besides, micro-CT has enabled the three-dimensional visualization of the acinar structure with high accuracy, which motivated a volumetric characterization of alveoli. Current morphometric studies of the lung tissue have analyzed the acinar morphology in terms of alveolar volume, alveolar diameter, surface-to-volume ratio, and porosity, among other parameters (Concha et al., 2018; Parameswaran et al., 2009; Sarabia-Vallejos, Zuñiga, & Hurtado, 2019; D. M. Vasilescu et al., 2012). In particular, porosity and alveolar surface area density emerge as insightful parameters in the study of diseases such as pulmonary emphysema (R. Yuan et al., 2010), as it quantifies the evolution of abnormally large airspaces produced by alveolar enlargement. In effect, septum rupture in emphysema results in higher porosity and lower density of the surface area than those found in normal lungs, which directly affects the ventilation-perfusion ratio, making it challenging to exchange gases with the bloodstream (Parameswaran et al., 2009).

While morphometric studies reported in the literature have provided vital information about the structural parameters of the lung parenchyma, current knowledge is based on a small number of micrometric samples that are randomly located in the lung. Such localized information does not provide information on the spatial distribution of alveolar structural properties throughout the organ. Based on this limitation, the scientific question that guides our work is: How is the regional distribution of morphological parameters in the whole lung? To answer this question, in this work, we combine micro-CT image acquisition, advanced image processing techniques, and computational geometry methods to unveil the three-

dimensional spatial distribution of porosity, alveolar surface area density, and surface-to-volume ratio in normal rat lungs.

4.2 MATERIAL AND METHODS

The bioethics committee of the Pontificia Universidad Católica de Chile approved the following protocol. Nine adult Sprague-Dawley rats (~ 300 g, sex-matched) were randomly assigned to three experimental groups according to the fixation method (each group with N = 3). Subjects were kept under controlled humidity, light, and temperature conditions before the lung *in situ* fixation step. Food and water were provided *ad libitum* during this period.

4.2.1 Lung sample preparation.

The preparation of lung samples consisted of three subsequent steps: *in situ* fixation of the lung, *ex vivo* fixation of the lung, and dehydration of the lung sample. For the *in situ* fixation stage of the lung, we followed the protocol described by Hausmann (Hausmann, 2007). Subjects were anesthetized with an intraperitoneal injection of ketamine and xylazine (30 mg^{-1} kg^{-1}, Drag Pharma Invetec S.A., Santiago, Chile, and 5 mg^{-1} kg^{-1}, Alfasan, Woerden, Holland, respectively). A cannula with a three-way in-line valve was introduced through the trachea of each subject in the supine position and was subsequently sealed using a cuff to instill into the lungs a formalin phosphate-buffered saline (F-PBS) solution at 4%. During the installation process, the transpulmonary pressure was maintained at 20 cm H_2O for 30 minutes using a syringe with a pressure transducer (AG Cuffil, Hospitech Respiration Ltd., Kfar Saba, Israel). Then, the three-way valve was closed to maintain pressure in the lungs, and the animal was refrigerated at 4 ° C for 8 h.

For the *ex vivo* lung fixation step, subjects were removed from the refrigerator, after which a median sternotomy was performed to remove the lungs out of the rib cage. During the whole surgery, care was exercised to avoid puncturing the organ, preventing leakage of the fixative solution. The left lung was dissected with the left bronchus clamped and then immersed into an F-PBS bath for 24 h.

For the dehydration step, three different drying methods were considered, which define the three experimental groups in this study. The drying methods were:

• Standard alcohol fixation (SAF): This method is the gold-standard in histology and pathology (Braber, Verheijden, Henricks, Kraneveld, & Folkerts, 2010; Hausmann, 2007). The sample was immersed for periods of 2 h in subsequent baths with increasing ethanol graduations (70%, 80%, and 90% ethanol in PBS), and finally in a 100% ethanol bath for 12 h. After this, the lung was removed from the last bath and left on a semi-covered plastic container to let it dry under ambient conditions for 3 h, to eliminate the remaining ethanol by evaporation.

• Modified alcohol fixation (MAF): Our research group designed this method as an alternative to the SAF method. First, the sample was immersed for 2 h in a 70% methanol-PBS solution. Subsequently, the same steps described in the SAF fixation method were performed.

• Standard alcohol fixation and HMDS (SAF-HMDS): This fixation method is recommended by the micro-CT manufacturer (Bruker-MicroCT, 2016). The sample was treated following the protocol in the SAF method. As a final and additional step, the sample was immersed in a hexamethyldisilazane solution (HMDS) for 2 h, after which the sample was allowed to dry under ambient conditions on a semi-covered plastic container for 3 h.

To characterize the volumetric change associated with the drying methods, the displaced volume of fluid was measured for each subject at the end of the dehydration stage and at the beginning of the *ex vivo* fixation stage. From these volumes, the lung volume ratio was calculated for each subject. Volume ratio values below 100% imply that the fixation and dehydration process resulted in sample shrinking.

4.2.2 Micro CT scanning protocol and 3D image reconstruction

All lung samples obtained were scanned using a commercial micro-CT (SkyScan 1272, Bruker Inc, Kontich, Belgium). During imaging, the samples were placed on the sample plate with the axial axis of the lung vertically aligned. The voltage and current of the X-ray source were set at 10 kV and 250 μA, respectively. Pulmonary tomographic images were obtained using two voxel resolutions: isotropic 15 μm (low resolution) and isotropic 4 μm (high resolution). The first low-resolution acquisition was used as a scout scan to confirm

that the sample fixation step did not introduce errors such as regions with marked alveolar collapse. The second high-resolution acquisition was used to generate images with an accurate definition of the alveolar architecture. Images were reconstructed using NRecon software (Bruker Inc., Kontich, Belgium) where misalignment compensation, ring artifact reduction, hardening, and Kuwahara filters were used to improve the signal-to-noise ratio. These were then processed using median and Wiener filters to reduce the inherent noise in the images, as well as a mix of top-hat and bottom-hat filters, along with a histogram equalization method to improve contrast, from the which were obtained 'enhanced 3D images of the lung'. For the morphological quantification of the images, 3D binary images were generated using a threshold filter on the Hounsfield unit scale based on the Otsu method (Xu, Xu, Jin, & Song, 2011).

Three-dimensional cubic domains of representative volume elements (RVE) with a border size of ~ 500 μm were selected from the enhanced images of the lung. During the selection procedure, acinar regions were targeted, and zones with large portions of bronchi or blood vessels were avoided. For each experimental group, 9 RVEs were selected per subject (3 in each region of the lung; basal, mid, and apical), resulting in a population of 27 RVEs per group. RVE images were then segmented to obtain binary masks, which were the basis for the morphological analysis.

4.2.3 Morphological analisys, and construction of 3D porosity and alveolar surface area density maps

The following morphological parameters were calculated for each RVE analyzed in this study: surface-to-volume ratio, mean alveolar diameter, alveolar wall thickness, porosity, and alveolar surface area density. Parameter quantification was carried out using an in-house code written in Matlab (MathWorks, Version R2017a, Natick, MA, USA). The determination of the alveolar diameter was performed using the SphereFit method (Jennings, 2020), which fits spheres within a point cloud using a least-squares algorithm. From the spheres obtained, an active contour algorithm based on the package "2D / 3D image segmentation toolbox" (Y. Zhang, 2020) was used to determine the surface and volume of the alveolar cavity. The ratio between these values allows us to determine the surface-to-volume ratio. The thickness of the alveolar wall was determined via the separation between

the centers of the contiguous spheres. By subtracting the alveolar radius of both spheres from this value, the minimum separation between the alveolar surfaces was obtained. For each RVE, porosity was computed as the ratio between the cavity volume and the reference volume (total RVE volume).

Convolution of a three-dimensional mask was carried out with the segmented image of the lung to determine the porosity maps. The objective of this convolution was to determine the number of airspace voxels contained within the analyzed volume, a value that was then divided by the total number of voxels in the mask to obtain the porosity for that particular sector. This process was repeated for each voxel of the segmented lung image to obtain a three-dimensional porosity image. The resulting porosity image had porosity values between 0 and 1, where 0 means that the analyzed sector contained only alveolar tissue, and 1 means that the mask only contained air.

To determine the alveolar surface area density maps, the boundary of the segmented images were detected using the Canny method (Canny, 1986), as implemented in the Image Processing Toolbox in Matlab. Based on the boundary surface, a Marching Cubes algorithm (Hammer, 2020) was used to obtain smoother surfaces. With this information, the surface area of the smoothed boundary was computed using a segmentation method based on level-set functions (Magee, Bulpitt, & Berry, 2013; D. M. Vasilescu et al., 2012) using a package implemented in Matlab (Li, Chui, Chang, & Ong, 2011). Similarly to the case of porosity maps, a three-dimensional mask was convoluted with the images of the segmented surface area to determine the total area comprised within the mask. This value was then divided by the reference volume, equal to the total volume of the mask, obtaining values of surface area density for each voxel of the lung image.

Surface-to-volume ratio maps were constructed from alveolar surface area density and porosity maps. For this purpose, let A_{alv}, $V_{airspace}$, and V_{ref} be the alveolar surface, the volume of alveolar airspace, and the reference volume of the sample to be analyzed (RVE total volume), respectively. The surface-to-volume ratio (ρ) can be expressed as:

$$\rho = \frac{A_{alv}}{V_{airspace}} = \frac{A_{alv}}{V_{ref}} \cdot \frac{V_{ref}}{V_{airspace}} = \frac{\eta}{\phi} \qquad (4.1)$$

where $\eta = \frac{A_{alv}}{V_{ref}}$ is equivalent to the definition of alveolar surface area density, and $\phi = \frac{V_{airspace}}{V_{ref}}$ corresponds to the definition of porosity. Using Equation (4.1), surface-to-volume ratio maps are constructed from the porosity and the alveolar surface area density maps in a voxel-wise way.

To assess the regional distribution of alveolar porosity, alveolar surface area density, and surface-to-volume ratio, regions of interest (ROI) were defined along the ventral-dorsal direction of each subject, following a method similar to that used in the regional characterization of lung deformation (Cruces et al., 2019; Hurtado et al., 2020). The regions of interest are connected sets of voxels selected from advancing planes in the selected direction, to achieve 10 contiguous regions with the same volume. The regional value of porosity and alveolar surface area density is obtained as the average of the values contained in each ROI.

A sensitivity analysis was performed to study the effect of the mask size used to determine the porosity and alveolar surface area density. Mask sizes of 140 μm, 105 μm, 70 μm, 35 μm, and 17.5 μm were used to generate five porosity and alveolar surface area density maps in the same axial section of the lung. Histograms for each mask size were generated to make a comparison between them.

4.2.4 Statistical Analysis

To detect significant differences in the morphological parameters between the study groups, 9 RVE samples were selected per subject from randomly chosen sectors of the lung, which generates a total of 27 RVE samples per group. The comparison between groups was performed using the Mann-Whitney two-sided U test, considering a p-value of 0.05 corrected by the Bonferroni method to allow the comparison between multiple groups.

For the inter-group comparison of regional values of porosity and alveolar surface area density, 3 sections were selected per anatomical sector (apical, mid, or basal) in each subject, which gives a total of 9 samples for each ROI per group. The comparison between the same ROI of different groups was carried out using the Mann-Whitney two-sided U test,

considering a p-value of 0.05 corrected by the Bonferroni method to allow the comparison of multiple groups. The error bars in figures show the standard deviation.

4.3 RESULTS

Values for the surface-to-volume ratio, mean alveolar diameter, alveolar wall thickness, porosity, alveolar surface area density, and lung volume ratio are reported in Table 4-1. The SAF group was significantly different than the MAF and SAF-HMDS groups for the surface-to-volume ratio, mean alveolar diameter, porosity, and lung volume ratio. Further, the mean alveolar diameter of the SAF-HMDS group resulted in significant differences when compared to the SAF and MAF groups. No significant differences were detected between the three groups for the case of the alveolar wall thickness and the alveolar surface area density.

Table 4-1. Alveolar morphological parameters for the RVE samples.

Group	Surface-to-volume ratio (mm^{-1})	Mean alveolar diameter (µm)	Alveolar wall thickness (µm)	Porosity	Alveolar surface area density ($µm^{-1}$)	Lung Volume Ratio (%)
SAF	89.5 ± 10.9*,†	29.48 ± 3.96*,†	6.92 ± 0.86	0.51 ± 0.05*,†	44.31 ± 1.91	56 ± 12*,†
MAF	67.7 ± 8.8*	40.51 ± 4.82*,#	7.09 ± 1.08	0.65 ± 0.05*	42.05 ± 0.72	87 ± 3*
SAF-HMDS	61.6 ± 5.5†	54.68 ± 5.18#,†	7.02 ± 0.45	0.65 ± 0.03†	40.83 ± 1.53	92 ± 2†

*statistical significance between SAF and MAF methods (p-value ≤ 0.05)

#statistical significance between MAF and SAF-HMDS methods (p-value ≤ 0.05)

†statistical significance between SAF and SAF-HMDS methods (p-value ≤ 0.05)

Figure 4-1 shows the results from 3D micro-CT imaging processing and the spatial morphological analysis for the whole lung of a representative subject in the SAF-HMDS group. Micro-CT images of the whole lung displayed major airway and vasculature structures at the macroscopic level, as well as delivered detailed information of bronchioli, respiratory ducts, and acinar structures, see Figure 4-1(a). The spatial distribution of porosity and alveolar surface area density were found to be homogeneous throughout the entire domain of the lung, see Figure 4-1(b) and Figure 4-1(c), respectively.

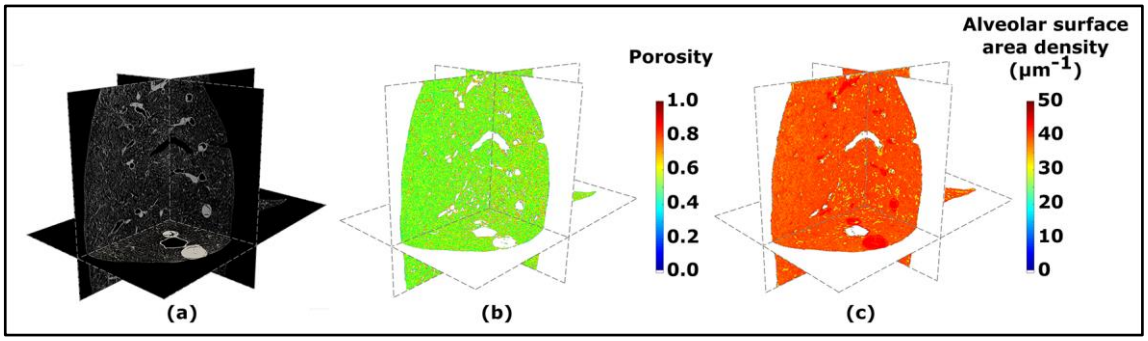

Figure 4-1. a) Micro-CT images of a lung in its axial, sagittal, and coronal views. b) Porosity and c) alveolar surface area density maps for the SAF-HMDS group in the different anatomical planes.

The regional distribution of alveolar porosity for the apical, mid, and basal zones of the lung is shown in Figure 4-2(a), Figure 4-2(b) and Figure 4-2(c), respectively. For the three areas analyzed, we found that the regional porosity values of the SAF group are significantly different (typically lower) than the values of the MAF and SAF-HMDS groups, with some exceptions in the mid and basal zones. No significant differences were found between the MAF and SAF-HMDS groups. Regarding the spatial distribution of porosity, uniform values were observed along the ventral-dorsal direction in all the areas analyzed in the MAF and SAF-HMDS groups. In contrast, a concave distribution is observed in the SAF group, with a tendency to reduce porosity towards the most ventral and dorsal areas.

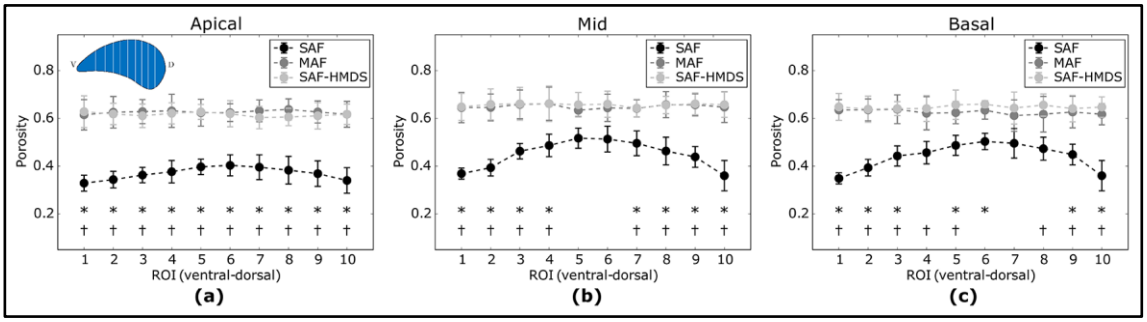

Figure 4-2. Regional distribution of porosity in the ventral-dorsal direction for three regions of the lung: (a) apical zone, (b) mid zone, and (c) basal zone. Significant differences between the SAF and MAF, SAF and SAF-HMDS, MAF, and SAF-HMDS groups are indicated by *, †, #, respectively.

The regional distribution of the alveolar surface area density for the apical, mid, and basal areas of the lung are shown in Figure 4-3(a), Figure 4-3(b), and Figure 4-3(c), respectively. For the mid and basal cases, significant differences were observed between the SAF and SAF-HMDS groups for almost all ROIs. Furthermore, significant differences between the MAF and SAF-HMDS groups are observed for half of the ROIs in the same areas. In the three groups, a uniform distribution of values is observed along the ventral-dorsal direction, for the apical, mid, and basal zones.

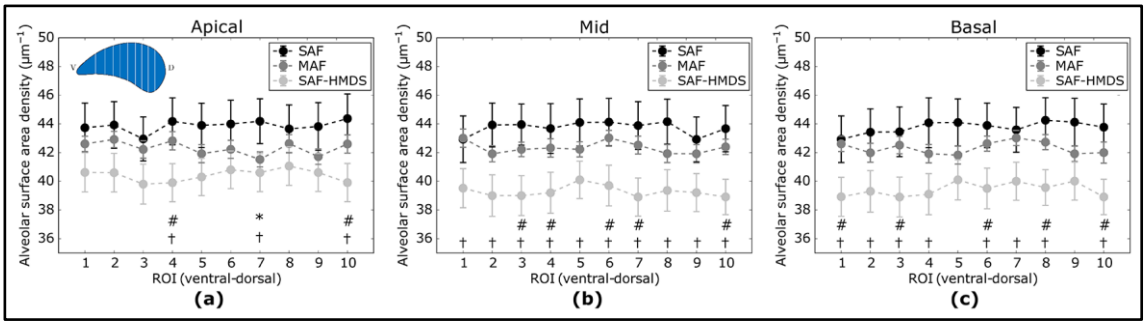

Figure 4-3. Regional distribution of alveolar surface area density in the ventral-dorsal direction for three regions of the lung: (a) apical zone, (b) mid zone, and (c) basal zone. Significant differences between the SAF and MAF, SAF and SAF-HMDS, MAF and SAF-HMDS groups are indicated by *, †, #, respectively.

The regional distribution of the surface-to-volume ratio for the apical, mid, and basal lung zones is shown in Figure 4-4(a), Figure 4-4(b), and Figure 4-4(c), respectively. With the particular exception of 2 ROIs, virtually all the regional values of the SAF group were found to be significantly different (higher) than the values of the MAF and SAF-HMDS groups. No significant differences were found between the MAF and SAF-HMDS. Furthermore, a uniform distribution of values is observed along the ventral-dorsal direction in all the areas analyzed for MAF and SAF-HMDS groups. In contrast, a convex distribution is observed in the SAF group, with a tendency to increase the surface-to-volume ratio values towards the most ventral and dorsal areas of the lung.

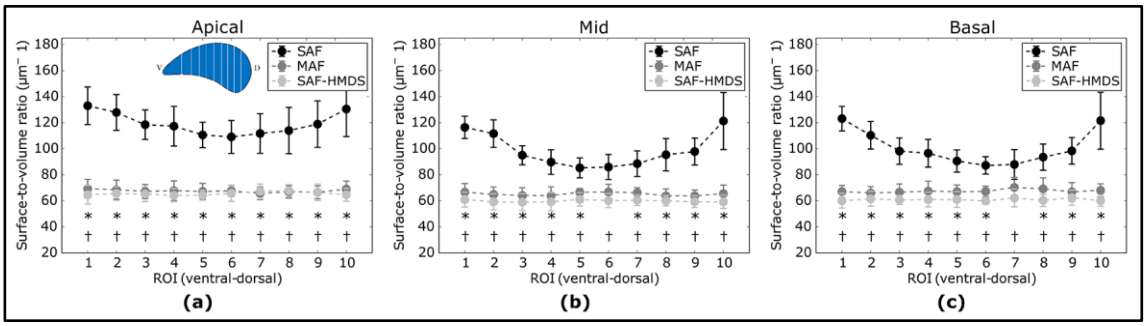

Figure 4-4. Regional distribution of surface-to-volume ratio in the ventral-dorsal direction for three regions of the lung: (a) apical zone, (b) mid zone, and (c) basal zone. Significant differences between the SAF and MAF, SAF and SAF-HMDS, MAF and SAF-HMDS groups are indicated by *, †, #, respectively.

The effects of mask size on the generation of porosity and alveolar surface area density maps are reported in Figure S 4-1 and Figure S 4-2 (supplementary material). For both parameters, we observe that mask sizes above 70 μm result in unimodal histograms with similar characteristics. In contrast, mask sizes smaller than 70 μm result in density functions that are not consistent with larger size masks, and that show oscillations in the range of smaller values.

4.4 DISCUSSION

In this work, we have studied the alveolar architecture of rat lungs using micro-CT and advanced computational geometry techniques. To the best of our knowledge, this work constitutes one of the first attempts to characterize the three-dimensional morphological parameters such as surface-to-volume ratio, porosity, and alveolar surface area density in the whole lung of Sprague-Dawley subjects. Structural studies based on micro-CT imaging have focused on C57BL/6 murine lungs, both under normal and diseased conditions (Parameswaran et al., 2009; D. M. Vasilescu et al., 2012), where the fixation procedure of the lung samples was similar to that performed in the SAF group. In 10 week-old normal mice, the mean alveolar diameter reported is 59 ± 2 μm (Parameswaran et al., 2009), which is comparable to the mean alveolar diameter found in the SAF-HMDS group in our work, and in the order of magnitude of the other two groups. Previous studies have shown that the alveolar volume and diameter in mice are smaller than in rats (Débora S Faffe, Rocco, Negri, & Zin, 2002). It is worth remarking that studies in mice use a higher tracheal pressure (30 cm H_2O) during *in situ* fixation than the pressure considered in this work (20 cm H_2O). More substantial tracheal pressures result in a larger alveolar expansion in mice, which may explain the similarity with the alveolar diameter values found in this work. The morphological analysis performed by Vasilescu *et al.* (D. M. Vasilescu et al., 2012) in the same species delivered surface-to-volume ratio values of 52 ± 3.7 and 47.7 ± 6 mm^{-1} in young (12-week old) and adult (91-week old) subjects, respectively. These values are smaller than the ones found in this study for all groups (Table 4-1) but coincide in the order of magnitude. We note that if the alveolus cavity is idealized as a sphere, then the surface-to-volume ratio is inversely proportional to the alveolar diameter. This, in turn, would imply that larger values of the surface-to-volume ratio are to be expected in mice than in rats, which is not the case. Again, we attribute these differences to the high tracheal pressure applied in mice experiments (30 cm H_2O), which results in larger alveoli dimensions. We note that in our work, the choice of applying an applied tracheal pressure of 20 cm H_2O was made to target physiological values of tidal volume, as a tracheal pressure of 30 cm H_2O typically corresponds to total lung capacity in murine subjects (Namati et al., 2006).

Three-dimensional maps displaying the distribution of porosity in the lung were successfully constructed for all subjects; see Figure 4-1(b) for a representative case. Porosity in the pulmonary parenchyma was found to be regionally uniform everywhere in the lung and locally similar in the MAF and SAF-HMDS groups, see Table 4-1 and Figure 4-2. These results suggest that the spatial distribution of regional porosity is homogeneous and is not subject to gravitational effects. This conclusion is supported by previous studies, like the one reported by Hoffman *et al.* (Mullan, Galvin, Zabner, & Hoffman, 1997; Namati et al., 2006). They estimated the air content on primate lungs in different anatomical regions, observing that air content is uniformly distributed in the lung and does not depend on the location of measurement. Another study that supports this conclusion is the work of Hogg *et al.*, where 16 parenchyma samples where randomly dissected from different regions of frozen human lungs and analyzed using micro-CT (McDonough et al., 2015). The alveolar density, defined as the number of alveoli in a reference volume, was found to be uniform regardless of their original location in the lung.

In our study, a marked reduction in porosity was observed towards the subpleural regions in the SAF group (most dorsal and ventral zones, see Figure 4-2). A careful examination of micro-CT images in those regions for a representative subject of the SAF-group revealed thickened alveolar septums, which is suggestive of alveolar collapse (micro-atelectasis), see Figure 4-5(a). In contrast, alveolar structures close to the pleura in representative subjects of the MAF and SAF-HMDS groups do not display alterations when compared to proximal acinar structures, see Figure 4-5(b) and Figure 4-5(c), respectively. These observations, along with the strong volume reductions observed in the SAF group (Table 4-1, lung volume ratio), suggest that the decrease in regional porosity in the SAF group is likely to be an artifact of the method rather than a physiological condition.

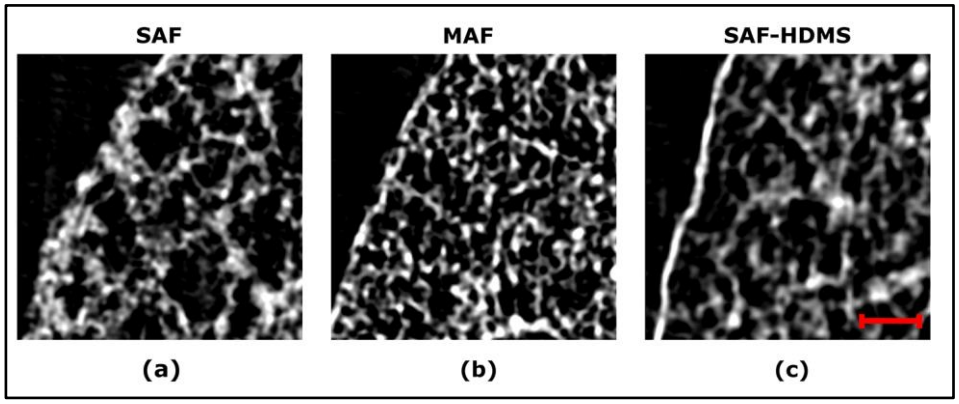

Figure 4-5. Magnifications of grayscale micro-CT images for subpleural regions of three representative subjects: (a) SAF group, (b) MAF group, and (c) SAF-HMDS group. The red scale bar corresponds to 100 μm.

Similarly to the case of porosity, three-dimensional maps of alveolar surface area density were obtained for all lung samples; see Figure 4-1(c) for a representative case. All three groups suggest that alveolar surface area density is homogeneous throughout the lung. Groups typically do differ in their assessment of ROI values. For example, significant differences between the SAF and SAF-HMDS groups were found in 21 out of 30 ROIs considered. More conclusive results were found in the study of the regional surface-to-volume ratio, where uniform distributions with similar values were found in the MAF and SAF-HMDS groups. These results suggest that the surface-to-volume ratio is homogeneous throughout the lung and does not exhibit a gravitational dependence. In contrast, the SAF group resulted in heterogenous distribution that largely deviated from the values found in the MAF and SAF-HMDS groups. We note that, since the surface-to-volume ratio is inversely proportional to the porosity, we conclude that the seemingly increasing values towards the most ventral and dorsal regions can be regarded as artifacts in the alveolar architecture induced the SAF method, based on the conclusions reached in the study of regional porosity.

Throughout this work, three methods for dehydration have been considered in the fixation of lung samples. The gold-standard and most popular method in studies involving the histological analysis and micro-CT imaging of murine lungs has been the SAF method, which employs ethanol solutions for the dehydration step (Braber et al., 2010; Hausmann,

2007; Puchtler, Waldrop, Meloan, Terry, & Conner, 1970). However, in our work, we have shown that the SAF method results in considerable lung shrinking (Table 4-1) that markedly affects the alveolar architecture in subpleural regions (Figure 4-5 (a)). An alternative method is the SAF-HMDS, which is predominantly used to prepare samples for electron microscopy, with some applications in micro-CT sample preparations. One advantage of the SAF-HMDS method is that it allows a rapid drying that has been shown to preserve the alveolar morphology without significant alterations (Bray, Bagu, & Koegler, 1993; Lee & Chow, 2012). However, the SAF-HMDS method has important operational disadvantages and risks to the user, as inhalation or skin exposure to HMDS is known to be hazardous to health (Chou & Chang, 2007). Another disadvantage is the management of HMDS residuals, as degradation results in products that can be harmful to the environment and that require special disposal procedures (Alleni, Kochs, & Chandra, 1997). Here, we propose and assess the use of the MAF method as an alternative in the dehydration of lung samples. The MAF dehydration method has been commonly employed in molecular biology to quantify the presence of biomarkers and to detect specific genetic alterations in organs/tissues (Anami et al., 2000; Noguchi, Furuya, Takeuchi, & Hirohashi, 1997). However, to the best of our knowledge, its application in the preparation of samples for micro-CT analysis is novel and has not been reported in the literature. Our results show that the application of a methanol-PBS solution before subsequent baths of ethanol solutions in lung samples preserve their volume (Table 4-1) and alveolar architecture everywhere in the lung, as most of the morphological parameters analyzed in this work do not display significant differences between the MAF and SAF-HMDS groups. We believe that the success of the MAF method is related to the ability of the methanol bath to increase cellular permeability, which then allows for enhanced diffusion properties during the ethanol bath dehydration step (Puchtler et al., 1970). We further note that methanol and PBS are safer in health terms than HMDS (lethal dose (LD_{50}) and lethal concentration (LC_{50}) values are considerably smaller for HMDS than methanol), and their disposal can be done without special requirements (the biodegradability of methanol is 99% while for HMDS is just 15.3%) (SIGMA-ALDRICH, 2019, 2020). Thus, we conclude that the proposed MAF dehydration method represents a convenient, sustainable, and safe procedure that does not alter the alveolar morphology in treated lung samples.

Several aspects of this work can be improved in future contributions. We have shown in our study that all fixation methods lead to different levels of tissue shrinking, which directly affects the alveolar architecture and the associated morphological parameters. Recently, *in vivo* micro-CT imaging of murine lungs has been reported (Lovric et al., 2017), where the acinar structure was reconstructed with high precision in living subjects. Future efforts on the morphological characterization of the lung may benefit from these *in vivo* imaging techniques, which may confirm or correct the values reported in this work. Another limitation of our study was the use of a single airway pressure level. Due to the elastic nature of the alveolar wall, the morphological values described in this work are expected to change in the event of different levels of airway pressure. Besides, our results have been obtained using only three subjects per group. While this small sample has allowed us to detect significant differences between groups, larger populations of Sprague-Dawley rats and other species should be considered in future works to confirm and extend our conclusions. Finally, in this work, we have advocated for the characterization of alveolar porosity, which is a microstructural parameter that is not commonly reported in respiratory physiology. We note, however, that porosity plays a crucial role in describing the mechanical response of porous biomaterials (Currey, 1988). A recent theoretical study shows that porosity, along with the alveolar wall elasticity, is the most relevant microstructural parameters in the mechanical response of the lung parenchyma (Concha et al., 2018). Further, the study shows that an increase of porosity, which can be directly associated with alveolar airspace enlargement, leads to a loss of parenchymal elastance, a mechanical relationship that has long been observed in lungs with pulmonary emphysema (Nagai, Yamawaki, Takizawa, & Thurlbeck, 1991). Therefore, a deep understanding of the porosity distribution in the whole lung plays a vital role in the creation of microstructurally-informed constitutive models (Eskandari, Nordgren, & O'Connell, 2019) that can predict the overall properties of the lung, as well as in informing organ-level computational models of the respiratory system (Eskandari, Kuschner, & Kuhl, 2015).

5. CHAPTER IV: QUANTIFICATION OF THE LUNG PARENCHYMA MECHANICAL PROPERTIES AND THE EFFECT OF COLLAGEN AND ELASTIN FIBERS DIGESTION.

5.1 INTRODUCTION

The local micromechanical analysis of the lung tissue is crucial to understand in-depth its relation with the mechanical response of the whole-organ (Birzle et al., 2019; Dassow et al., 2010; S. M K Rausch, Martin, et al., 2011) and to predict the evolution of some respiratory diseases (Brower et al., 2000; Gattinoni, Carlesso, & Caironi, 2012). According to Laurent *et al.* (Laurent et al., 2007), the collagen and elastin fibers are randomly distributed in the lung parenchyma with no apparent ordering in the alveolar wall structure. Also, in their report, it was mentioned that the collagen/elastin network mostly dominates the mechanical properties of the lung, both at the macro- and micro-scale (Suki & Stamenović, 2011). The physicochemical alteration of these fibers could lead to complicated diseases such as fibrosis or pulmonary emphysema (Alsafadi et al., 2017; Finlay, O'Donnell, O'Connor, Hayes, & Fitzgerald, 1996). The first one corresponds to a lung disease that occurs due to progressive tissue damage. As lung tissue remodels, it becomes thickened and stiff, making it difficult for the patient to breathe properly. In most cases, the cause of tissue damage is unknown and, it could derive from a myriad of different factors, including long-term exposure to toxins (silica dust, asbestos fibers, hard metal dust, coal dust, among others), particular medical conditions (sarcoidosis, rheumatoid arthritis, or pneumonia, among others), radiation therapies or some medications (Seger et al., 2018). However, one of the most undesirable microstructural effects of this disease is the thickening of collagen fibers, which lead to a local modification of lung parenchymal micromechanics, thus altering, in a heterogeneous way, the mechanical response of the tissue during a normal breathing cycle (Haak, Tan, & Tschumperlin, 2018).

Using the PCLS methodology, it has been possible to develop multiple and different lung models related to tissue micromechanics response (Birzle & Wall, 2019; Wall, Wiechert, Comerford, & Rausch, 2010). However, a niche has not been studied profoundly, the

mechanical tissue response after treatment with proteases like collagenase or elastase. The mentioned enzymes have the particular characteristic of breaking down the lung parenchyma's structural fibers, reducing its mechanical response to deformation. A mechanical model that could infer this effect in the lung tissue at the microscale is still pending, and even more so, a mechanical model that can predict the mechanical behavior at both micro- and macro-scale will be extremely valuable.

This work's hypothesis states that if the PCLS samples are treated with collagenase or elastase, the mechanical response at quasi-static or dynamic tests should be significantly different from the control samples. However, we are not the first group to develop these kinds of studies. Accordingly, we take as a guideline the studies carried out by Birzle *et al.* (Birzle et al., 2019), Rausch *et al.* (S. M K Rausch, Martin, et al., 2011), and Suki *et al.* (Suki & Stamenović, 2011), who have been already performed advances in this area. Our research group already optimized the fixation protocols for μ-CT imaging at different transpulmonary pressures, and they do not differ significantly from the used to obtain the PCLS at different pressures.

The data collected so-far serves as a starting point for future investigations on this topic and experimental data to compare results from novel theoretical mechanical multi-scale models. This study obtains information about the dynamic and quasi-static load curves using PCLS samples with and without protease treatment (collagenase and elastase). These treatments were done by processing the sample at room temperature or incubating it at body temperature for one hour. The main objective of this study is to obtain start-up information about the mechanic behavior of the PCLS and the variation of the energy density associated with the dynamic cyclic load of the lung parenchyma. A secondary objective is also related to obtaining data that could serve as a proof-of-concept to corroborate if the set-up and the procedures implemented by our research group are correct.

5.2 METHODOLOGY

All the experiments performed in this study were done under the authorization of the “Scientific-ethical committee for the animal care and environment” of Pontificia Universidad Catolica de Chile.

5.2.1 Animal and PCLS preparation

The samples were obtained from adult Sprague-Dawley rats (~300 gr, sex-matched, 12 - 15 weeks). The animals were maintained in humidity, light, and temperature-controlled environment before inducing anesthesia. Food and water were provided *ad libitum* during this period. The subjects were intraperitoneally injected with a mixture of ketamine and xylazine (30 mg^{-1} kg^{-1}, Drag Pharma Invetec S.A., Santiago, Chile, and 5 mg^{-1} kg^{-1}, Alfasan, Woerden, Netherland, respectively). After tracheal instillation with 1% lidocaine (Drag Pharma Invetec S.A., Santiago, Chile), the intubation was performed with a 16G BD Angiocath® catheter with an in-line three-way valve (Becton Dickinson Infusion Therapy Systems Inc., Utah, USA). This catheter was used to insert liquid agarose at 4% gently to the lungs. A syringe with a pressure transducer attached (AG Cuffil, Hospitech Respiration Ltd., Kfar Saba, Israel) was used to control the transpulmonary pressure during this process at 20 cm H_2O. Then, the animal was refrigerated at 4 °C for 30 min to ensure agarose solidification. The lungs were excised from the animal thorax through a sternotomy procedure and stored in Hank's Balanced Salt Solution (HBSS). Agarose fixation maintains almost intact the alveolar network's microarchitecture, but the samples must be used within 48 h to avoid possible decompositions of the tissue.

Then, using a dermal-punch for biopsies (Acu-punch 12 mm, Acuderm Inc., Fort Lauderdale, USA), cylinders of 12 mm in diameter were gently extracted from the left lung (gathering 3 to 4 cylinders from each lung). These tissue cylinders were then laminated into 1 mm thick PCLS slices using a vibratome (Compresstome VF-200, Precisionary Instruments, Massachusetts, USA).

The obtained PCLS were maintained in HBSS solution and refrigerated at 4 °C until posterior use. These samples were divided into five groups: without any treatment (Ctrl), treated with collagenase at room temperature (Col), incubated with collagenase at 37-38 °C (tCol), treated with elastase at room temperature (Ela), and incubated with elastase (tEla). Collagenase-H (from *Clostridium histolyticum*, > 0.15 U/mg, Sigma-Aldrich, St. Louis, Missouri, USA) was dissolved in HBSS (1 mg/mL), and it was letting it react for an hour with the samples in a sealed container. Similarly, the treatment with elastase consisted of a

solution of elastase (from porcine pancreas, > 4 U/mg, Sigma-Aldrich, St. Louis, Missouri, USA) dissolved in HBSS (0.25 mg/mL); the samples were also maintained in this solution for one hour to ensure correct digestion.

5.2.2 Mechanical tests measuring protocol

The PCLS samples were tested using a uniaxial system Electroforce 5500 from TA Instruments (Minneapolis, USA). The initial separation between the clamps (sample initial length, l_0) was always set at 2.5 mm. The samples were preconditioned following the next protocol: 20 sinusoidal cycles at 35% strain with a frequency of 0.5 Hz. Once the preconditioning was finished, the clamps move backward to the initial position; then, the PCLS was slowly stretched until finding a minimal resistance force (0.2 N). Then the sample is stretched until it reaches 110%, at a rate of 5 x 10^{-3} mm/s. A schematic description of the protocol followed to obtain the PCLS and its mechanical testing is shown in Figure 5-1.

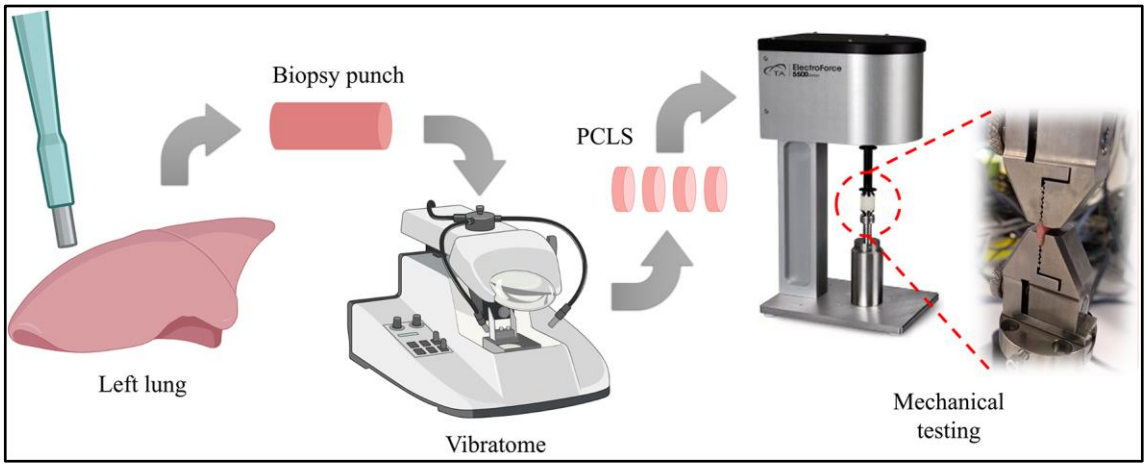

Figure 5-1. Schematic description of the protocol used to obtain and mechanically test the PCLS.

5.2.3 Data analysis and statistical tests

For each sample, raw curves of force vs. time and position vs. time were obtained for the quasi-static and dynamic tests. These data were mixed to obtain a force vs. position curve. From these curves, and using the initial cross-section and length of the sample, is it possible to obtain the nominal stress vs. strain plots. A digital Butterworth lowpass filter (order 1 and

5 Hz sampling frequency) was applied to these curves to reduce the inherent noise. Interestingly, this filter also reduces noise from lower frequency sources (like power supply and motor fan, which is approximately 25 Hz).

The PCLS samples treated with proteases were extremely delicate, particularly those treated with collagenase (Birzle et al., 2019). Accordingly, some samples fail to withstand the entire load test; these cases were not considered in the analysis, so it should not interfere with the overall results. Using the last preconditioning curve, each sample's hysteresis can be calculated with a trapezoidal integration of the stress and strain vectors. The quasi-static curves were used to compare its mechanical behavior at various strains under different treatment conditions (protease digestion).

5.3 RESULTS AND DISCUSSION

This section presents the results obtained from the mechanical testing of PCLS using different proteases to digest collagen or elastin fibers of the tissue. Only the left lung was used in each case because it is formed just by one lobe, thus avoiding the generation of incomplete or partial PCLS samples, leading to some mechanical inconsistencies during the tensile testing. This process allows us to obtain a total of 37 PCLS to study. The variable sample number in the subject pool was related to the lung size of each animal. From bigger lungs, more samples could be obtained. Besides, the PCLS damage in the process of loading or even during the manipulation could lead to sample failure, thus reducing the number of viable samples to test. Table 5-1 gives a detailed distribution of the PCLS used in each group. From the data, we realize that the number of control PCLS (Ctrl) is the largest one, almost doubling the collagenase and elastase treated samples (Col and Ela). As is it was mentioned before, this effect becomes more critical for incubated PCLS. The number of these PCLS is even lower in these cases (tCol and tEla), mainly due to the fragility of the PCLS samples treated with proteases during incubation (Birzle et al., 2019).

Kolmogorov-Smirnov tests for normality give positive results in Ctrl, Col, Ela, and tEla, but the low number of PCLS samples for tCol is not enough to affirm normality in this case.

Therefore, one of the protocol's first improvements is to obtain more PCLS samples to obtain reliable and accurate results.

Unbalanced two-way ANOVA based on a linear mixed model was performed in this case to check if the control and proteases-treated samples are statistically different between them. This particular type of statistical test was chosen due to the problem characteristics; it needs to be unbalanced due to the different group sample number; two-way because there are two main variables in the problem, subjects and treatment; and based on a linear mixed model to include the interaction between groups. Also, due to the non-normality of some groups perform a linear mixed model is the most recommendable for these cases. For the linear mixed model, the treatment variable (Ctrl, Col, tCol, Ela, tEla) was considered a fixed variable, and the subjects are treated as the random variable; besides, the interaction between the groups was also included in the model.

Table 5-1. Distribution of PCLS samples within the groups.

Rat / PCLS	S1	S2	S3	S4	**Total**
Ctrl	5	3	3	3	14
Col	2	2	1	2	7
tCol	1	1	1	1	4
Ela	2	2	2	1	7
tEla	1	1	2	1	5
Total	11	9	9	8	**37**

The protocol performed for carrying out the mechanical test gives us two main results: firstly, the hysteresis curves, obtained from the last cycle of the preconditioning step (Figure 5-2a), and secondly, the quasi-static response of the lung samples (Figure 5-2b).

In the hysteresis curves, the loading and unloading processes have a relatively high frequency, so the viscoelastic effects are predominant, thus showing a different tendency in the loading curve compared to the unloading curve. This difference occurs due to material

energy dissipation, mainly caused by internal friction between its components (collagen and elastin fibers with the rest of the ECM). As observed in Figure 5-2a, the loading or unloading curves' tendency varies when different proteases are used. This effect was expectable because the material mechanical properties change, but the data's statistical analysis does not show clear results about hysteresis changes between the groups.

As the quasi-static test was carried out with a reasonably slow speed (5 x 10^{-3} mm/s), the material's viscoelastic properties do not contribute to the overall behavior of the tissue. In Figure 5-2b, it is possible to observe tissue mechanical properties changes according to the protease used in each case. Interestingly, the samples treated with collagen (Col, blue curve) and incubated with collagen (tCol, light blue curve) present poorly mechanical properties compared to the control sample (Ctrl, red curve). In contrast, the elastin (Ela, dark green curve) and incubated elastin (tEla, green curve) show similar behavior, indicating that incubating elastase treatment is not so crucial. On the other hand, the Col sample present increased stiffness compared to the tCol curve, but both present lower stiffness than the control sample (Ctrl).

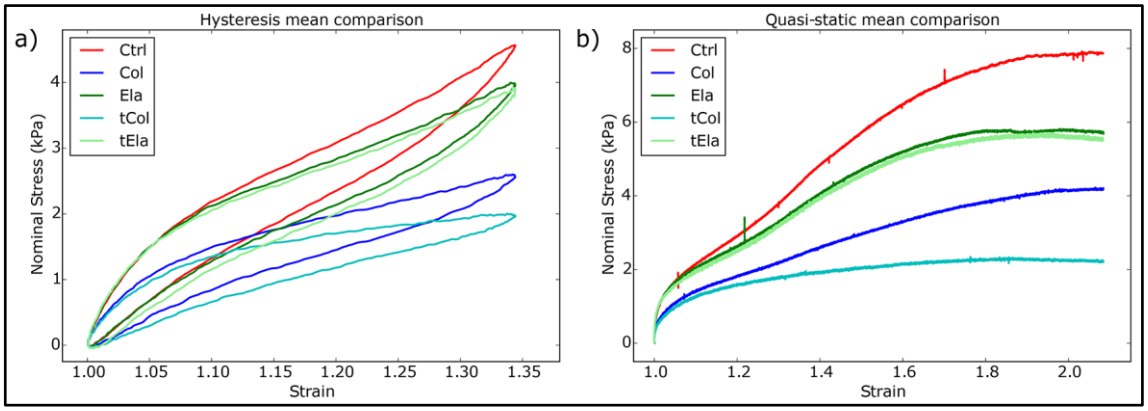

Figure 5-2. a) Hysteresis curves of the last cycle of preconditioning for control samples and treated with collagen and elastin. b) The quasi-static response of the PCLS treated with different proteases.

Firstly, to analyze this data, the hysteresis curve area was computed and statistically compared between the different groups (control or protease digestion). With the finality of obtaining a graphical representation of these values, a boxplot of the mean hysteresis values is depicted in Figure 5-3a. Similarly, the quasi-static nominal stress boxplots at 25%, 50%,

and 100% strain are depicted (Figures 5-3b, c, and d). These graphs give us a clue about the evolution of nominal stress at the same strain value for samples treated with different procedures.

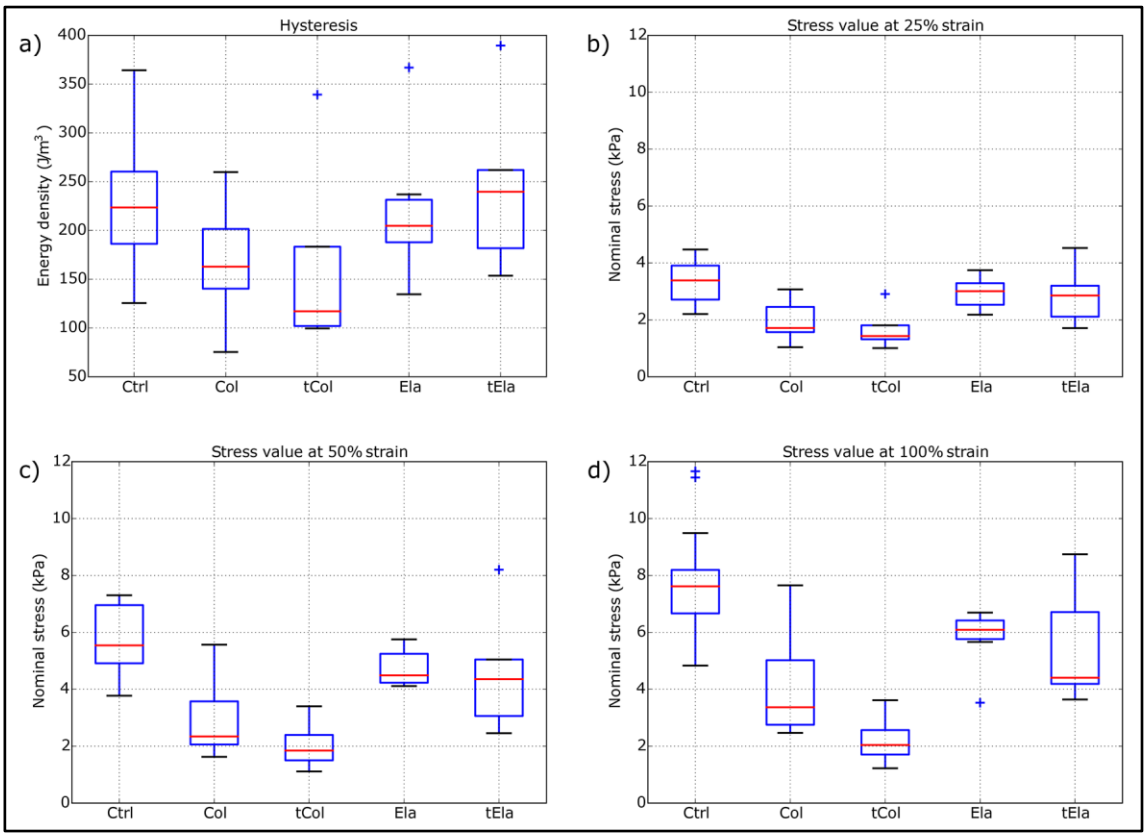

Figure 5-3. a) Boxplot of the mean hysteresis values obtained from the last cycle of the preconditioning cycle. Boxplots for nominal stress value at b) 25%, c) 50%, and d) 100% strain of the quasi-static curve.

As is possible to observe in Figure 5-3a, the hysteresis values do not seem to have a tendency, but it shows a decrease when the means of Col and Ela samples are compared with the control sample (Ctrl). This effect is expectable because, as it was mentioned previously, the hysteresis is related to the energy dissipated due to the friction produced between the fibers of collagen and elastin and the rest of the ECM components, so, if some part of the fibers is digested, a decrease in hysteresis must be expectable. A similar situation occurs when the treatment is performed under incubation; in this case, more fibers are digested, so the hysteresis must seem diminished. Interestingly, when the ANOVA test is carried out for this

data, any group shows the statistical difference from any other (F-value: 2.19, p-value: 0.092). This effect is probably related to the high dispersity of the data, which could be observed in the boxplot (Figure 5-3a).

In Figures 5-3b, 5-3c, and 5-3d, boxplots for the nominal stress at different strain ratios (25%, 50%, and 100%) are depicted. In this case, ANOVA results indicate that, for the three different strain values selected, the samples treated with collagenase or elastase (Col and Ela) are statistically different from the Ctrl samples (F-values are higher than F-critical for all of the cases), which means that the variances between the means of the groups are statistically different. Interestingly, from these results, we could also infer that when collagenase and incubated collagenase groups (Col and tCol) are compared, the mechanical properties over 50% strain are statistically different, but when Ela and tEla are compared, the statistical difference is not enough to ensure that incubation affects the mechanical properties of the tissue (Johanson & Pierce, 1972; Karlinsky et al., 1976). From this analysis, we could also indicate that there is no interaction between the subjects and treatments; the interaction coefficients in the linear mixed model are close to zero in every case. In general, the p-values of the ANOVA analysis indicates that the overall alteration of protease digestion protocol modifies the mechanical response of the tissue by resulting in p-values smaller than 0.05 (p-value for 25% strain: 0.0001, p-value for 50% strain: 2.14×10^{-6}, p-value for 100% strain: 3.26×10^{-8}).

5.4 CONCLUSIONS

The results obtained from this study corresponds to the first approach performed to carry out the mechanical tests for thin lung tissue strips (PCLS). The protocol performed to obtain these samples corresponds to an *in situ* soft fixation of the lung (inside the thorax cavity) based on agarose's insertion through the trachea. Then, small cylinders are cut from the lungs and laminated by using a vibratome. These strips (PCLS) were treated with different proteases (collagenase and elastase) to digest the fibers. These samples were used to measure the control and protease-treated lung tissue's mechanical properties in two different experiments (quasi-static and dynamic curves). The dynamic test allows us to obtain the hysteresis values from comparing the loading and unloading curves. From the quasi-static

tests, it is possible to measure the tissue's mechanical response at different strain states without considering the viscoelastic effects of the lung parenchyma. The mechanical results are satisfactory, thus showing statistical differences depending on the protease used compared to the control samples. Interestingly, hysteresis values related to the viscous energy dissipation of the tissue do not show any significant difference between the treatments. However, the tissue's mechanical response in the quasi-static regime does it, particularly at higher strains (50% and 100%).

The study has two main limitations that need to be solved in future work; the first one is to increase the number of PCLS obtained in each group (particularly the protease-treated ones) to ensure enough statistical significance. Secondly, it is crucial to modify the mechanical test procedure to avoid possible slippering of the PCLS at high strains. According to the data obtained by Birzle *et al.* (Birzle et al., 2019), Rausch *et al.* (S. M K Rausch, Martin, et al., 2011) and Suki *et al.* (Suki & Stamenović, 2011), at high strains, a mechanical hardening is observed for the lung tissue, an effect which is not observed in our data, probably related to slippering of the sample.

6. CONCLUSIONS AND FUTURE PERSPECTIVES OF THIS THESIS

The goal of this thesis was to establish a close relationship between the microstructure of the lung parenchyma and the micromechanical behavior of the pulmonary tissue. To this end, we explored several situations where the microarchitecture of the alveolar network could affect the local mechanical response of the tissue. One of the most relevant phenomena in alveolar mechanics is the so-called “stress raiser”, which corresponds to concentrations of alveolar stresses in localized regions. According to our results, these stress concentrations in normal tissue can be up to 27 times the applied alveolar pressure. Interestingly, we show that the stress amplification factor strongly depends on the alveolar pressure level, *i.e.*, stresses do not scale proportional to the applied alveolar pressure. Also, we demonstrated that alveolar walls are subject to a fully 3D state of stresses rather than to a pure axial stress state. Advanced imaging techniques were carried out to acquire reliable and accurate 3D lung microstructure images. Fixation procedures were proposed in this thesis to reduce the shrinkage level during the preparation of lung samples. By comparing the proposed method with gold-standard fixation techniques, we showed that the method used to fix and dehydrate the samples could severely impact the final microarchitecture of the lung parenchyma revealed by micro-CT imaging. Further, we showed that crucial parameters that describe the alveolated tissue's morphology could be largely affected by fixation methods that do not prevent shrinkage. Accordingly, during this thesis development, we designed and optimized a dehydration method based on methanol and ethanol baths, which has similar results compared to the gold standard used to fix and dehydrate samples for electron microscopy and micro-CT purposes.

Another objective of this thesis was to develop novel tools useful in the medical image processing field. Notably, we combined micro-CT imaging and computational geometry algorithms to study the regional distribution of key morphological parameters (porosity and alveolar surface area density maps) throughout the whole lung. This analysis corroborates that morphological parameters have a uniform spatial distribution and do not seem to be affected by gravitational effects in normal lungs in murine species.

Besides, we developed a protocol to measure the mechanical properties of lung tissue strips experimentally by using a soft fixation method via agarose intratracheal instillation in the lungs. This methodology allows us to carry out a uniaxial tensile test in small lung samples without damaging the lung parenchyma microstructure. By applying a digestion protocol of elastin and collagen, it was also possible to measure the mechanical properties of the tissue with different percentages of the connective elastic matrix. These results allow us to demonstrate that protease digestion has a profound impact on the mechanical properties of the lung when the viscoelastic effects are neglected (quasi-static tests). Parallel, the hysteresis values (obtained from dynamic curves) do not significantly differ between the groups analyzed.

The results and conclusions reported in this thesis can be extended in several directions. First, we remark that our focus has been on the mechanics and morphology of normal lung tissue, but the same techniques developed here can be used to explore the mechanics and morphology of pulmonary tissue under pathological conditions. For example, some critical morphological parameters of the lung parenchyma could change in emphysematous lungs due to alveolar wall rupture, which leads to an air compartment enlargement, thus reducing the surface-to-volume ratio (Stamenovic, 1990), and therefore, increasing lung parenchymal porosity. Using the three-dimensional surface-to-volume ratio or porosity maps, it could be possible to detect the early stages of emphysema via slight color changes in localized sectors of the lung parenchyma. The lung regional morphological analysis could also serve to inform the lung's computational models, as multi-scale models require porosity values as an input (Concha et al., 2018). The relevance of porosity in the lung parenchyma's mechanical response justifies the need to further assess this and other morphological parameters in the whole domain of diseased lungs.

Second, all imaging work has been performed in *ex vivo* samples that may not accurately represent the physiological condition. Further studies may leverage the recent introduction of *in vivo* imaging technologies (Lovric et al., 2017). Using a novel gating system and synchrotron-based micro-CT, it is possible to visualize small lung parenchyma structures with an incredible resolution using *in vivo* specimens. This technology can generate unprecedented results in this research field, unveiling physiological deformation

mechanisms not know to date, as well as providing precise and robust morphological and mechanical information about the lung.

Finally, we remark that with the micromechanical models validated in this work, together with the whole-lung characterization of morphological parameters, a natural next step is constructing whole-organ multiscale models and their validation. Eskandari *et al.* (Eskandari et al., 2019) propose a model that links the function of the pulmonary airways with his microstructure through a structurally-motivated constitutive model, augmented with biochemical analysis and histological observations, that can predict the overall properties of the lung (Eskandari et al., 2015). Our research group also performed some efforts in this direction; for example, Concha *et al.* presented a novel micromechanical model based on homogenization methods and incompressible Neo-Hookean structural elements. The model shows that porosity and the alveolar wall elasticity are the most relevant microstructural parameters in the mechanical response of the lung parenchyma (Concha et al., 2018). A whole-organ multiscale predictive model of the lung under pathological diseases remains a open avenue of research that can largely benefit from the results exposed in this thesis.

7. REFERENCES

Al-Mayah, A., Moseley, J., Velec, M., & Brock, K. (2009). Sliding characteristic and material compressibility of human lung: Parametric study and verification. *Medical Physics*, *36*(10), 4625–4633. https://doi.org/10.1118/1.3218761

Al-Mayah, A., Moseley, J., Velec, M., & Brock, K. (2011). Toward efficient biomechanical-based deformable image registration of lungs for image-guided radiotherapy. *Physics in Medicine and Biology*, *56*(15), 4701–4713. https://doi.org/10.1088/0031-9155/56/15/005

Alleni, R. B., Kochs, P., & Chandra, G. (1997). Industrial Organosilicon Materials, Their Environmental Entry and Predicted Fate (pp. 1–25). https://doi.org/10.1007/978-3-540-68331-5_1

Alsafadi, H. N., Staab-Weijnitz, C. A., Lehmann, M., Lindner, M., Peschel, B., Königshoff, M., & Wagner, D. E. (2017). An ex vivo model to induce early fibrosis-like changes in human precision-cut lung slices. *American Journal of Physiology-Lung Cellular and Molecular Physiology*, *312*(6), L896–L902. https://doi.org/10.1152/ajplung.00084.2017

Amelon, R., Cao, K., Ding, K., Christensen, G. E., Reinhardt, J. M., & Raghavan, M. L. (2011). Three-dimensional characterization of regional lung deformation. *Journal of Biomechanics*, *44*(13), 2489–2495. https://doi.org/10.1016/j.jbiomech.2011.06.009

Amin, S. D., Majumdar, A., Frey, U., & Suki, B. (2010). Modeling the dynamics of airway constriction: Effects of agonist transport and binding. *Journal of Applied Physiology*, *109*(2), 553–563. https://doi.org/10.1152/japplphysiol.01111.2009

Anami, Y., Takeuchi, T., Mase, K., Yasuda, J., Hirohashi, S., Perucho, M., & Noguchi, M. (2000). Amplotyping of microdissected, methanol-fixed lung carcinoma by arbitrarily primed polymerase chain reaction. *International Journal of Cancer*, *89*(1), 19–25. https://doi.org/10.1002/(SICI)1097-0215(20000120)89:1<19::AID-IJC4>3.0.CO;2-3

ARDS Network. (2000). Ventilation With Lower Tidal Volumes As Compared With Traditional Tidal Volumes for ALI and the ARDS. *The New England Journal of Medicine*, *342*(18), 1301–1308. https://doi.org/10.1056/NEJM200005043421801

Ashby, M. F., & Medalist, R. F. M. (1983). The mechanical properties of cellular solids. *Metallurgical Transactions A*, *14*(9), 1755–1769. https://doi.org/10.1007/BF02645546

Ask, K., Labiris, R., Farkas, L., Moeller, A., Froese, A., Farncombe, T., … Kolb, M. R. J. (2008). Comparison between conventional and "clinical" assessment of experimental lung fibrosis. *Journal of Translational Medicine*, *6*, 1–10. https://doi.org/10.1186/1479-5876-6-16

Bachofen, H., & Schürch, S. (2001). Alveolar surface forces and lung architecture. *Comparative Biochemistry and Physiology Part A: Molecular & Integrative Physiology*, *129*(1), 183–193. https://doi.org/10.1016/S1095-6433(01)00315-4

Bajc, M., & Jonson, B. (2011). Ventilation/Perfusion SPECT for Diagnosis of Pulmonary Embolism and Other Diseases. *International Journal of Molecular Imaging*, *2011*(5), 1–7. https://doi.org/10.1155/2011/682949

Bates, J. H. T. (1998). A micromechanical model of lung tissue rheology. *Annals of Biomedical Engineering*, *26*(4), 679–687. https://doi.org/10.1114/1.42

Bel-Brunon, A., Kehl, S., Martin, C., Uhlig, S., & Wall, W. A. (2014). Numerical identification method for the non-linear viscoelastic compressible behavior of soft

tissue using uniaxial tensile tests and image registration - Application to rat lung parenchyma. *Journal of the Mechanical Behavior of Biomedical Materials*, *29*, 360–374. https://doi.org/10.1016/j.jmbbm.2013.09.018

Bell, R. D., Rudmann, C., Wood, R. W., Schwarz, E. M., & Rahimi, H. (2018). Longitudinal micro-CT as an outcome measure of interstitial lung disease in TNF-transgenic mice. *PLOS ONE*, *13*(1), e0190678. https://doi.org/10.1371/journal.pone.0190678

Birzle, A. M., Hobrack, S. M. K., Martin, C., Uhlig, S., & Wall, W. A. (2019). Constituent-specific material behavior of soft biological tissue: experimental quantification and numerical identification for lung parenchyma. *Biomechanics and Modeling in Mechanobiology*, (0123456789). https://doi.org/10.1007/s10237-019-01151-3

Birzle, A. M., & Wall, W. A. (2019). A viscoelastic nonlinear compressible material model of lung parenchyma – Experiments and numerical identification. *Journal of the Mechanical Behavior of Biomedical Materials*, *94*, 164–175. https://doi.org/10.1016/j.jmbbm.2019.02.024

Braber, S., Verheijden, K. A. T., Henricks, P. A. J., Kraneveld, A. D., & Folkerts, G. (2010). A comparison of fixation methods on lung morphology in a murine model of emphysema. *American Journal of Physiology-Lung Cellular and Molecular Physiology*, *299*(6), L843–L851. https://doi.org/10.1152/ajplung.00192.2010

Bray, D. F., Bagu, J., & Koegler, P. (1993). Comparison of hexamethyldisilazane (HMDS), Peldri II, and critical-point drying methods for scanning electron microscopy of biological specimens. *Microscopy Research and Technique*, *26*(6), 489–495. https://doi.org/10.1002/jemt.1070260603

Brower, R. G., Matthay, M. A., Morris, A., Schoenfeld, D., Thompson, B. T., Wheeler, A., … Wheeler. (2000). Ventilation with lower tidal volumes as compared with traditional tidal volumes for acute lung injury and the acute respiratory distress syndrome. *The New England Journal of Medicine*, *342*(18), 1301–8. https://doi.org/10.1056/NEJM200005043421801

Bruker-MicroCT. (2016). Chemical drying of specimens to enhance contrast. *Bruker-Skyscan Method Notes*, (January), 1–8.

Budiansky, B., & Kimmel, E. (1987). Elastic moduli of lungs. *Journal of Applied Mechanics, Transactions ASME*, *54*(2), 351–358. https://doi.org/10.1115/1.3173019

Canny, J. (1986). A Computational Approach to Edge Detection. *IEEE Transactions on Pattern Analysis and Machine Intelligence*, *PAMI-8*(6), 679–698. https://doi.org/10.1109/TPAMI.1986.4767851

Cavalcante, F. S. A. A., Ito, S., Brewer, K., Sakai, H., Alencar, A. M., Almeida, M. P., … Me-, S. (2005). Mechanical interactions between collagen and proteoglycans: implications for the stability of lung tissue. *Journal of Applied Physiology*, *98*(2), 672–679. https://doi.org/10.1152/japplphysiol.00619.2004

CGAL. (2018). CGAL User and Reference Manual. CGAL editoral board.

Choi, S., Hoffman, E. A., Wenzel, S. E., Tawhai, M. H., Yin, Y., Castro, M., & Lin, C.-L. L. (2013). Registration-based assessment of regional lung function via volumetric CT images of normal subjects vs. severe asthmatics. *Journal of Applied Physiology*, *115*(5), 730–742. https://doi.org/10.1152/japplphysiol.00113.2013

Chou, M.-S., & Chang, K.-L. (2007). UV/ozone degradation of gaseous hexamethyldisilazane (HMDS). *Chemosphere*, *69*(5), 697–704. https://doi.org/10.1016/j.chemosphere.2007.05.040

Clark, A. R., Burrowes, K. S., & Tawhai, M. H. (2019). Ventilation/perfusion matching: Of myths, mice, and men. *Physiology*, *34*(6), 419–429. https://doi.org/10.1152/physiol.00016.2019

Concha, F., Sarabia-Vallejos, M., & Hurtado, D. E. (2018). Micromechanical model of lung parenchyma hyperelasticity. *Journal of the Mechanics and Physics of Solids*, *112*, 126–144. https://doi.org/10.1016/j.jmps.2017.11.021

Cook, D. N., & Nakano, H. (2015). *Comparative Biology of the Normal Lung*. *Comparative Biology of the Normal Lung*. https://doi.org/10.1016/B978-0-12-404577-4.00033-3

Cressoni, M., Cadringher, P., Chiurazzi, C., Amini, M., Gallazzi, E., Marino, A., … Gattinoni, L. (2013). Lung Inhomogeneity in Patients with Acute Respiratory Distress Syndrome. *American Journal of Respiratory and Critical Care Medicine*, *189*(2), 131121141258006. https://doi.org/10.1164/rccm.201308-1567OC

Cressoni, M., Chiumello, D., Algieri, I., Brioni, M., Chiurazzi, C., Colombo, A., … Gattinoni, L. (2017). Opening pressures and atelectrauma in acute respiratory distress syndrome. *Intensive Care Medicine*, *43*(5), 603–611. https://doi.org/10.1007/s00134-017-4754-8

Cressoni, M., Chiurazzi, C., Gotti, M., Amini, M., Brioni, M., Algieri, I., … Gattinoni, L. (2015). Lung Inhomogeneities and Time Course of Ventilator-induced Mechanical Injuries. *Anesthesiology*, *123*(3), 618–627. https://doi.org/10.1097/ALN.0000000000000727

Cruces, P., Erranz, B., Lillo, F., Sarabia-Vallejos, M. A., Iturrieta, P., Morales, F., … Hurtado, D. E. (2019). Mapping regional strain in anesthetised healthy subjects during spontaneous ventilation. *BMJ Open Respiratory Research*, *6*(1), e000423. https://doi.org/10.1136/bmjresp-2019-000423

Currey, J. D. (1988). The effect of porosity and mineral content on the Young's modulus of elasticity of compact bone. *Journal of Biomechanics*, *21*(2), 131–139. https://doi.org/10.1016/0021-9290(88)90006-1

Dale, P. J., Matthews, F. L., & Schroter, R. C. (1980). Finite element analysis of lung alveolus. *Journal of Biomechanics*, *13*(10), 865–873. https://doi.org/10.1016/0021-9290(80)90174-8

Dassow, C., Wiechert, L., Martin, C., Schumann, S., Müller-Newen, G., Pack, O., … Uhlig, S. (2010). Biaxial distension of precision-cut lung slices. *Journal of Applied Physiology*, *108*(3), 713–721. https://doi.org/10.1152/japplphysiol.00229.2009

Deng, L., Xiao, S. M., Qiang, J. W., Li, Y. A., & Zhang, Y. (2017). Early Lung Adenocarcinoma in Mice: Micro-Computed Tomography Manifestations and Correlation with Pathology. *Translational Oncology*, *10*(3), 311–317. https://doi.org/10.1016/j.tranon.2017.02.003

Dreyfuss, D., & Hubmayr, R. (2016). What the concept of VILI has taught us about ARDS management. *Intensive Care Medicine*, *42*(5), 811–813. https://doi.org/10.1007/s00134-016-4287-6

Dudak, J., Zemlicka, J., Karch, J., Patzelt, M., Mrzilkova, J., Zach, P., … Krejci, F. (2016). High-contrast X-ray micro-radiography and micro-CT of ex-vivo soft tissue murine organs utilizing ethanol fixation and large area photon-counting detector. *Scientific Reports*, *6*, 30385. https://doi.org/10.1038/srep30385

Ehling, J., Theek, B., Gremse, F., Baetke, S., Möckel, D., Maynard, J., … Lammers, T. (2014). Micro-CT Imaging of Tumor Angiogenesis. *The American Journal of*

Pathology, *184*(2), 431–441. https://doi.org/10.1016/j.ajpath.2013.10.014

Eskandari, M., Kuschner, W. G., & Kuhl, E. (2015). Patient-Specific Airway Wall Remodeling in Chronic Lung Disease. *Annals of Biomedical Engineering*, *43*(10), 2538–2551. https://doi.org/10.1007/s10439-015-1306-7

Eskandari, M., Nordgren, T. M., & O'Connell, G. D. (2019). Mechanics of pulmonary airways: Linking structure to function through constitutive modeling, biochemistry, and histology. *Acta Biomaterialia*, *97*, 513–523. https://doi.org/10.1016/j.actbio.2019.07.020

Ethier, C. R., & Simmons, C. A. (2007). *Introductory Biomechanics*. *Introductory Biomechanics - from Cells to Organisms*. Cambridge: Cambridge University Press. https://doi.org/10.1017/CBO9780511809217

Faffe, D. S., D'Alessandro, E. S., Xisto, D. G., Antunes, M. A., Romero, P. V., Negri, E. M., … Rocco, P. R. M. (2006). Mouse strain dependence of lung tissue mechanics: Role of specific extracellular matrix composition. *Respiratory Physiology & Neurobiology*, *152*(2), 186–196. https://doi.org/10.1016/j.resp.2005.08.008

Faffe, D. S., Rocco, P. R. M., Negri, E. M., & Zin, W. a. (2002). Comparison of rat and mouse pulmonary tissue mechanical properties and histology. *Journal of Applied Physiology (Bethesda, Md. : 1985)*, *92*, 230–234. https://doi.org/10.1152/japplphysiol.01214.2000

Finlay, G. A., O'Donnell, M. D., O'Connor, C. M., Hayes, J. P., & Fitzgerald, M. X. (1996). Elastin and collagen remodeling in emphysema: A scanning electron microscopy study. *American Journal of Pathology*, *149*(4), 1405–1415.

Fish, J., & Fan, R. (2008). Mathematical homogenization of nonperiodic heterogeneous media subjected to large deformation transient loading. *International Journal for Numerical Methods in Engineering*, *76*(7), 1044–1064. https://doi.org/10.1002/nme.2355

Ford, N. L., Jeklin, A., Yip, K., Yohan, D., Holdsworth, D. W., & Drangova, M. (2014). Optimization of Image Quality in Retrospective Respiratory-Gated Micro-CT for Quantitative Measurements of Lung Function in Free-Breathing Rats. *Journal of Biomedical Science and Engineering*, *07*(04), 157–172. https://doi.org/10.4236/jbise.2014.74020

Ford, N. L., McCaig, L., Jeklin, A., Lewis, J. F., Veldhuizen, R. A. W., Holdsworth, D. W., & Drangova, M. (2017). A respiratory-gated micro-CT comparison of respiratory patterns in free-breathing and mechanically ventilated rats. *Physiological Reports*, *5*(2), e13074. https://doi.org/10.14814/phy2.13074

Fujioka, H., Halpern, D., & Gaver, D. P. (2013). A model of surfactant-induced surface tension effects on the parenchymal tethering of pulmonary airways. *Journal of Biomechanics*, *46*(2), 319–328. https://doi.org/10.1016/j.jbiomech.2012.11.031

Fukaya, H., Martin, C. J., Young, A. C., & Katsura, S. (1968). Mechanical properties of alveolar walls. *Journal of Applied Physiology*, *25*(6), 689–695.

Fung, Y. C. (1988). A model of the lung structure and its validation. *Journal of Applied Physiology*, *64*(5), 2132–2141. https://doi.org/10.1152/jappl.1988.64.5.2132

Gattinoni, L., Carlesso, E., & Caironi, P. (2012). Stress and strain within the lung. *Current Opinion in Critical Care*, *18*(1), 42–47. https://doi.org/10.1097/MCC.0b013e32834f17d9

Gattinoni, L., Tonetti, T., & Quintel, M. (2018). Intensive care medicine in 2050: ventilator-

induced lung injury. *Intensive Care Medicine*, *44*(1), 76–78. https://doi.org/10.1007/s00134-017-4770-8

Gefen, A., Elad, D., & Shiner, R. J. (1999). Analysis of stress distribution in the alveolar septa of normal and simulated emphysematic lungs. *Journal of Biomechanics*, *32*(9), 891–897. https://doi.org/10.1016/S0021-9290(99)00092-5

Gefen, A., Halpern, P., Shiner, R. J., Schroter, R. C., & Elad, D. (2001). Analysis of mechanical stresses within the alveolar septa leading to pulmonary edema. *Technology and Health Care : Official Journal of the European Society for Engineering and Medicine*, *9*(3), 257–267.

Gehr, P., Bachofen, M., & Weibel, E. R. (1978). The normal human lung: ultrastructure and morphometric estimation of diffusion capacity. *Respiration Physiology*, *32*(2), 121–140. https://doi.org/10.1016/0034-5687(78)90104-4

Ghadiali, S. N., & Gaver, D. P. (2008). Biomechanics of liquid–epithelium interactions in pulmonary airways. *Respiratory Physiology & Neurobiology*, *163*(1–3), 232–243. https://doi.org/10.1016/j.resp.2008.04.008

Gibson, L. J., & Ashby, M. F. (1982). Mechanics of Three-Dimensional Cellular Materials. *Proceedings of The Royal Society of London, Series A: Mathematical and Physical Sciences*, *382*(1782), 43–59. https://doi.org/10.1098/rspa.1982.0088

Gibson, L. J., & Ashby, M. F. (1999). *Cellular Solids*. Cambridge University Press. https://doi.org/10.1017/CBO9781139878326

Gil, J., Bachofen, H., Gehr, P., & Weibel, E. R. (1979). Alveolar volume-surface area relation in air- and saline-filled lungs fixed by vascular perfusion. *Journal of Applied Physiology: Respiratory, Environmental and Exercise Physiology*, *47*(5), 990–1001. https://doi.org/10.1152/jappl.1979.47.5.990

Haak, A. J., Tan, Q., & Tschumperlin, D. J. (2018). Matrix biomechanics and dynamics in pulmonary fibrosis. *Matrix Biology*, *73*, 64–76. https://doi.org/10.1016/j.matbio.2017.12.004

Hammer, P. (2020). Marching Cubes. MathWorks Central File Exchange. Retrieved from https://www.mathworks.com/matlabcentral/fileexchange/32506-marching-cubes

Hausmann, R. (2007). Methods of Lung Fixation. In *Forensic Pathology Reviews* (Vol. 4, pp. 437–451). Totowa, NJ: Humana Press. https://doi.org/10.1007/978-1-59259-921-9_15

Hildebrandt, J. (1970). Pressure-volume data of cat lung interpreted by a plastoelastic, linear viscoelastic model. *Journal of Applied Physiology*, *28*(3), 365–372. https://doi.org/10.1152/jappl.1970.28.3.365

Hoppin, F. G., Lee, G. C., & Dawson, S. V. (1975). Properties of lung parenchyma in distortion. *Journal of Applied Physiology*, *39*(5), 742–751. https://doi.org/10.1152/jappl.1975.39.5.742

Hsia, C. C. W., Hyde, D. M., Ochs, M., & Weibel, E. R. (2010). An Official Research Policy Statement of the American Thoracic Society/European Respiratory Society: Standards for Quantitative Assessment of Lung Structure. *American Journal of Respiratory and Critical Care Medicine*, *181*(4), 394–418. https://doi.org/10.1164/rccm.200809-1522ST

Hsia, C. C. W., Hyde, D. M., & Weibel, E. R. (2016). Lung structure and the intrinsic challenges of gas exchange. *Comprehensive Physiology*, *6*(2), 827–895. https://doi.org/10.1002/cphy.c150028

Hurtado, D. E., Erranz, B., Lillo, F., Sarabia-Vallejos, M., Iturrieta, P., Morales, F., … Cruces, P. (2020). Progression of regional lung strain and heterogeneity in lung injury: assessing the evolution under spontaneous breathing and mechanical ventilation. *Annals of Intensive Care*, *10*(1), 107. https://doi.org/10.1186/s13613-020-00725-0

Hurtado, D. E., Villarroel, N., Andrade, C., Retamal, J., Bugedo, G., & Bruhn, A. (2017). Spatial patterns and frequency distributions of regional deformation in the healthy human lung. *Biomechanics and Modeling in Mechanobiology*, *16*(4), 1413–1423. https://doi.org/10.1007/s10237-017-0895-5

Hurtado, D. E., Villarroel, N. N., Retamal, J., Bugedo, G., & Bruhn, A. (2016). Improving the Accuracy of Registration-Based Biomechanical Analysis: A Finite Element Approach to Lung Regional Strain Quantification. *IEEE Transactions on Medical Imaging*, *35*(2), 580–588. https://doi.org/10.1109/TMI.2015.2483744

Jardins, T. Des. (2008). *Cardiopulmonary Anatomy & Physiology: Essentials for Respiratory Care* (Fifth Edit). Delmar, CENGAGE Learning.

Jennings, A. (2020). MATLAB SphereFit (least squared). MathWorks Central File Exchange. Retrieved from https://www.mathworks.com/matlabcentral/fileexchange/34129-sphere-fit-least-squared

Jögi, J., Ekberg, M., Jonson, B., Bozovic, G., & Bajc, M. (2011). Ventilation/perfusion SPECT in chronic obstructive pulmonary disease: An evaluation by reference to symptoms, spirometric lung function and emphysema, as assessed with HRCT. *European Journal of Nuclear Medicine and Molecular Imaging*, *38*(7), 1344–1352. https://doi.org/10.1007/s00259-011-1757-5

Johanson, W. G., & Pierce, A. K. (1972). Effects of Elastase, Collagenase, and Papain on Structure and Function of Rat Lungs In Vitro. *Journal of Clinical Investigation*, *51*(2), 288–293. https://doi.org/10.1172/JCI106813

Jones, E., Oliphant, T., & Peterson, P. (2001). SciPy: open source scientific tools for Python. Retrieved from http://www.scipy.org/

Karakaplan, A. D., Bieniek, M. P., & Skalak, R. (1980). A mathematical model of lung parenchyma. *Journal of Biomechanical Engineering*, *102*(2), 124–136. https://doi.org/10.1115/1.3138208

Karlinsky, J. B., Catanese, A., Honeychurch, C., Sherter, C. B., Hoppin, F. G., & Snider, G. L. (1976). In vitro effects of elastase and collagenase on mechanical properties of hamster lungs. *Chest*, *69*(2), 275–276. https://doi.org/10.1378/chest.69.2.275

Kimmel, E., & Budiansky, B. (1990). Surface tension and the dodecahedron model for lung elasticity. *Journal of Biomechanical Engineering*, *112*(2), 160–167. https://doi.org/10.1115/1.2891167

Kononov, S., Brewer, K., Sakai, H., Cavalcante, F. S. A., Sabayanagam, C. R., Ingenito, E. P., & Suki, B. (2001). Roles of mechanical forces and collagen failure in the development of elastase-induced emphysema. *American Journal of Respiratory and Critical Care Medicine*, *164*(10 I), 1920–1926. https://doi.org/10.1164/rccm2101083

Kowe, R., Schroter, R. C., Matthews, F. L., & Hitchings, D. (1986). Analysis of elastic and surface tension effects in the lung alveolus using finite element methods. *Journal of Biomechanics*, *19*(7), 541–549. https://doi.org/10.1016/0021-9290(86)90127-2

Kriete, A., Breithecker, A., & Rau, W. D. (2001). 3D imaging of lung tissue by confocal microscopy and micro-CT. In D. D. Duncan, S. L. Jacques, & P. C. Johnson (Eds.),

Laser-Tissue Interaction XII: Photochemical, Photothermal, and Photomechanical (Vol. 4257, p. 469). https://doi.org/10.1117/12.434736

Kumar, H., Vasilescu, D. M., Yin, Y., Hoffman, E. A., Tawhai, M. H., & Lin, C.-L. C.-L. (2013). Multiscale imaging and registration-driven model for pulmonary acinar mechanics in the mouse. *Journal of Applied Physiology*, *114*(8), 971–978. https://doi.org/10.1152/japplphysiol.01136.2012

Lahellec, N., & Suquet, P. (2007). On the effective behavior of nonlinear inelastic composites: I. Incremental variational principles. *Journal of the Mechanics and Physics of Solids*, *55*(9), 1932–1963. https://doi.org/10.1016/j.jmps.2007.02.003

Langheinrich, A. C., Leithäuser, B., Greschus, S., von Gerlach, S., Breithecker, A., Matthias, F. R., … Bohle, R. M. (2004). Acute Rat Lung Injury: Feasibility of Assessment with Micro-CT. *Radiology*, *233*(1), 165–171. https://doi.org/10.1148/radiol.2331031340

Laurent, G. J., Chambers, R. C., Hill, M. R., & McAnulty, R. J. (2007). Regulation of matrix turnover: fibroblasts, forces, factors and fibrosis. *Biochemical Society Transactions*, *35*(4), 647–651. https://doi.org/10.1042/BST0350647

Leary, S., Underwood, W., Anthony, R., & Cartner, S. (2013). *AVMA Guidelines for the Euthanasia of Animals: 2013 Edition*. *American Veterinary Medical Association*. https://doi.org/10.1016/B978-012088449-0.50009-1

Lee, J. T. Y., & Chow, K. L. (2012). SEM sample preparation for cells on 3D scaffolds by freeze-drying and HMDS. *Scanning*, *34*(1), 12–25. https://doi.org/10.1002/sca.20271

Li, B. N., Chui, C. K., Chang, S., & Ong, S. H. (2011). Integrating spatial fuzzy clustering with level set methods for automated medical image segmentation. *Computers in Biology and Medicine*, *41*(1), 1–10. https://doi.org/10.1016/j.compbiomed.2010.10.007

Litzlbauer, H. D., Neuhaeuser, C., Moell, A., Greschus, S., Breithecker, A., Franke, F. E., … Rau, W. S. (2006). Three-dimensional imaging and morphometric analysis of alveolar tissue from microfocal X-ray-computed tomography. *American Journal of Physiology. Lung Cellular and Molecular Physiology*, *291*(3), L535–L545. https://doi.org/10.1152/ajplung.00088.2005

Liu, A., & Joe, B. (1994). Relationship between tetrahedron shape measures. *BIT*, *34*(2), 268–287. https://doi.org/10.1007/BF01955874

Lovric, G., Mokso, R., Arcadu, F., Vogiatzis Oikonomidis, I., Schittny, J. C., Roth-Kleiner, M., & Stampanoni, M. (2017). Tomographic in vivo microscopy for the study of lung physiology at the alveolar level. *Scientific Reports*, *7*(1), 1–10. https://doi.org/10.1038/s41598-017-12886-3

Ma, B., & Bates, J. H. T. (2010). Modeling the complex dynamics of derecruitment in the lung. *Annals of Biomedical Engineering*, *38*(11), 3466–3477. https://doi.org/10.1007/s10439-010-0095-2

Magee, D., Bulpitt, A., & Berry, E. (2013). Combining 3D Deformable Models and Level Set Methods for the Segmentation of Abdominal Aortic Aneurysms, 35.1-35.9. https://doi.org/10.5244/c.15.35

Makiyama, A. M., Gibson, L. J., Harris, R. S., & Venegas, J. G. (2014). Stress concentration around an atelectatic region: A finite element model. *Respiratory Physiology & Neurobiology*, *201*, 101–110. https://doi.org/10.1016/j.resp.2014.06.017

McDonough, J. E., Knudsen, L., Wright, A. C., Mark Elliott, W., Ochs, M., & Hogg, J. C. (2015). Regional differences in alveolar density in the human lung are related to lung

height. *Journal of Applied Physiology*, *118*(11), 1429–1434. https://doi.org/10.1152/japplphysiol.01017.2014

Mead, J., Takishima, T., & Leith, D. (1970). Stress distribution in lungs: a model of pulmonary elasticity. *Journal of Applied Physiology (Bethesda, Md. : 1985)*, *28*(5), 596–608. https://doi.org/10.1152/jappl.1970.28.5.596

Mercer, R. R., Russell, M. L., & Crapo, J. D. (1994). Alveolar septal structure in different species. *Journal of Applied Physiology*, *77*(3), 1060–1066. https://doi.org/10.1152/jappl.1994.77.3.1060

Mortola, J. P. (2013). Lung Viscoelasticity. *Clinical Pulmonary Medicine*, *20*(3), 144–148. https://doi.org/10.1097/CPM.0b013e31828fc9d6

Mullan, B. F., Galvin, J. R., Zabner, J., & Hoffman, E. A. (1997). Evaluation of in Vivo Total and Regional Air Content and Distribution in Primate Lungs with High-Resolution CT. *Academic Radiology*, *4*(10), 674–679. https://doi.org/10.1016/S1076-6332(97)80138-9

Nagai, A., Yamawaki, I., Takizawa, T., & Thurlbeck, W. M. (1991). Alveolar attachments in emphysema of human lungs. *American Review of Respiratory Disease*, *144*(4), 888–891. https://doi.org/10.1164/ajrccm/144.4.888

Namati, E., Chon, D., Thiesse, J., Hoffman, E. A., De Ryk, J., Ross, A., & McLennan, G. (2006). In vivo micro-CT lung imaging via a computer-controlled intermittent iso-pressure breath hold (IIBH) technique. *Physics in Medicine and Biology*, *51*(23), 6061–6075. https://doi.org/10.1088/0031-9155/51/23/008

NIH, & NHLBI. (2012). Fact Book Fiscal Year 2012. *NHLBI Fact Book, Fiscal Year 2012*, 33–52.

Noguchi, M., Furuya, S., Takeuchi, T., & Hirohashi, S. (1997). Modified formalin and methanol fixation methods for molecular biological and morphological analyses. *Pathology International*, *47*(10), 685–691. https://doi.org/10.1111/j.1440-1827.1997.tb04442.x

Osmanagic, E., Sukstanskii, A. L., Quirk, J. D., Woods, J. C., Pierce, R. A., Conradi, M. S., … Yablonskiy, D. A. (2010). Quantitative assessment of lung microstructure in healthy mice using an MR-based 3He lung morphometry technique. *J Appl Physiol (1985)*, *109*(6), 1592–1599. https://doi.org/10.1152/japplphysiol.00736.2010

Otis, D. R., Ingenito, E. P., Kamm, R. D., & Johnson, M. (1994). Dynamic surface tension of surfactant TA: experiments and theory. *Journal of Applied Physiology*, *77*(6), 2681–2688. https://doi.org/10.1152/jappl.1994.77.6.2681

Otsu, N. (1979). A Threshold Selection Method from Gray-Level Histograms. *IEEE Transactions on Systems, Man, and Cybernetics*, *9*(1), 62–66. https://doi.org/10.1109/TSMC.1979.4310076

Parameswaran, H., Bartolák-Suki, E., Hamakawa, H., Majumdar, A., Allen, P. G., & Suki, B. (2009). Three-dimensional measurement of alveolar airspace volumes in normal and emphysematous lungs using micro-CT. *Journal of Applied Physiology*, *107*(2), 583–592. https://doi.org/10.1152/japplphysiol.91227.2008

Perlman, C. E. (2014). On modeling edematous alveolar mechanics. *Journal of Applied Physiology*, *117*(8), 937–937. https://doi.org/10.1152/japplphysiol.00696.2014

Perlman, C. E., & Bhattacharya, J. (2007). Alveolar expansion imaged by optical sectioning microscopy. *Journal of Applied Physiology (Bethesda, Md. : 1985)*, *103*(3), 1037–1044. https://doi.org/10.1152/japplphysiol.00160.2007

Perlman, C. E., & Wu, Y. (2014). In situ determination of alveolar septal strain, stress and effective Young's modulus: an experimental/computational approach. *AJP: Lung Cellular and Molecular Physiology*, *307*(4), L302–L310. https://doi.org/10.1152/ajplung.00106.2014

Powell, M. J. D. (1964). An efficient method for finding the minimum of a function of several variables without calculating derivatives. *The Computer Journal*, *7*(2), 155–162. https://doi.org/10.1093/comjnl/7.2.155

Protti, A., Cressoni, M., Santini, A., Langer, T., Mietto, C., Febres, D., … Gattinoni, L. (2011). Lung Stress and Strain during Mechanical Ventilation. *American Journal of Respiratory and Critical Care Medicine*, *183*(10), 1354–1362. https://doi.org/10.1164/rccm.201010-1757OC

Puchtler, H., Waldrop, F. S., Meloan, S. N., Terry, M. S., & Conner, H. M. (1970). Methacarn (methanol-Carnoy) fixation. *Histochemie*, *21*(2), 97–116. https://doi.org/10.1007/BF00306176

Rajapakse, C. S., Bashoor-Zadeh, M., Li, C., Sun, W., Wright, A. C., & Wehrli, F. W. (2015). Volumetric Cortical Bone Porosity Assessment with MR Imaging: Validation and Clinical Feasibility. *Radiology*, *276*(2), 526–35. https://doi.org/10.1148/radiol.15141850

Rausch, S. M. K. (2012). Computational and Experimental Modeling of Lung Parenchyma.

Rausch, S. M. K., Haberthür, D., Stampanoni, M., Schittny, J. C., & Wall, W. A. (2011). Local strain distribution in real three-dimensional alveolar geometries. *Annals of Biomedical Engineering*, *39*(11), 2835–2843. https://doi.org/10.1007/s10439-011-0328-z

Rausch, S. M. K., Martin, C., Bornemann, P. B., Uhlig, S., & Wall, W. A. (2011). Material model of lung parenchyma based on living precision-cut lung slice testing. *Journal of the Mechanical Behavior of Biomedical Materials*, *4*(4), 583–592. https://doi.org/10.1016/j.jmbbm.2011.01.006

Retamal, J., Hurtado, D., Villarroel, N., Bruhn, A., Bugedo, G., Amato, M. B. P., … Borges, J. B. (2018). Does Regional Lung Strain Correlate With Regional Inflammation in Acute Respiratory Distress Syndrome During Nonprotective Ventilation? An Experimental Porcine Study. *Critical Care Medicine*, *46*(6), e591–e599. https://doi.org/10.1097/CCM.0000000000003072

Ritman, E. L. (2011). Current Status of Developments and Applications of Micro-CT. *Annual Review of Biomedical Engineering*, *13*(1), 531–552. https://doi.org/10.1146/annurev-bioeng-071910-124717

Roth, C. J., Yoshihara, L., & Wall, W. A. (2017). A simplified parametrised model for lung microstructures capable of mimicking realistic geometrical and mechanical properties. *Computers in Biology and Medicine*, *89*, 104–114. https://doi.org/10.1016/j.compbiomed.2017.07.017

Ruscitti, F., Ravanetti, F., Essers, J., Ridwan, Y., Belenkov, S., Vos, W., … Stellari, F. F. (2017). Longitudinal assessment of bleomycin-induced lung fibrosis by Micro-CT correlates with histological evaluation in mice. *Multidisciplinary Respiratory Medicine*, *12*(1), 8. https://doi.org/10.1186/s40248-017-0089-0

Sarabia-Vallejos, M. A., Zuñiga, M., & Hurtado, D. E. (2019). The role of three-dimensionality and alveolar pressure in the distribution and amplification of alveolar stresses. *Scientific Reports*, *9*(1), 8783. https://doi.org/10.1038/s41598-019-45343-4

Scotton, C. J., Hayes, B., Alexander, R., Datta, A., Forty, E. J., Mercer, P. F., … Chambers, R. C. (2013). Ex vivo micro-computed tomography analysis of bleomycin-induced lung fibrosis for preclinical drug evaluation. *European Respiratory Journal*, *42*(6), 1633–1645. https://doi.org/10.1183/09031936.00182412

Seger, S., Stritt, M., Vezzali, E., Nayler, O., Hess, P., Groenen, P. M. A., & Stalder, A. K. (2018). A fully automated image analysis method to quantify lung fibrosis in the bleomycin-induced rat model. *PLOS ONE*, *13*(3), e0193057. https://doi.org/10.1371/journal.pone.0193057

Setnikar, I. (1955). Origin and significance of the mechanical property of the lung. *Archivio Di Fisiologia*, *55*(4), 349–74. Retrieved from http://www.ncbi.nlm.nih.gov/pubmed/13314863

SIGMA-ALDRICH. (2019). SDS Methanol.

SIGMA-ALDRICH. (2020). SDS Hexamethyldisilazane.

Slutsky, A. S., & Ranieri, V. M. (2013). Ventilator-Induced Lung Injury, (4), 699–700. https://doi.org/10.1056/NEJMra1208707

Soldati, G., Smargiassi, A., Inchingolo, R., Sher, S., Nenna, R., Valente, S., … Corbo, G. M. (2014). Lung ultrasonography may provide an indirect estimation of lung porosity and airspace geometry. *Respiration*, *88*(6), 458–468. https://doi.org/10.1159/000368086

Solomonov, I., Talmi-Frank, D., Milstein, Y., Addadi, S., Aloshin, A., & Sagi, I. (2015). Introduction of correlative light and airSEM microscopy imaging for tissue research under ambient conditions. *Scientific Reports*, *4*(1), 5987. https://doi.org/10.1038/srep05987

Stamenovic, D. (1990). Micromechanical foundations of pulmonary elasticity. *Physiological Reviews*, *70*(4), 1117–1134. https://doi.org/10.1152/physrev.1990.70.4.1117

Stamenovic, D., & Wilson, T. A. (1985). A strain energy function for lung parenchyma. *Journal of Biomechanical Engineering*, *107*(1), 81–86. https://doi.org/10.1115/1.3138525

Suga, K., Kawakami, Y., Koike, H., Iwanaga, H., Tokuda, O., Okada, M., & Matsunaga, N. (2010). Lung ventilation-perfusion imbalance in pulmonary emphysema: Assessment with automated V/Q quotient SPECT. *Annals of Nuclear Medicine*, *24*(4), 269–277. https://doi.org/10.1007/s12149-010-0369-7

Suki, B., Jesudason, R., Sato, S., Parameswaran, H., Araujo, A. D., Majumdar, A., … Bartolák-Suki, E. (2012). Mechanical failure, stress redistribution, elastase activity and binding site availability on elastin during the progression of emphysema. *Pulmonary Pharmacology and Therapeutics*, *25*(4), 268–275. https://doi.org/10.1016/j.pupt.2011.04.027

Suki, B., Sato, S., Parameswaran, H., Szabari, M. V., Takahashi, A., & Bartolak-Suki, E. (2013). Emphysema and Mechanical Stress-Induced Lung Remodeling. *Physiology*, *28*(6), 404–413. https://doi.org/10.1152/physiol.00041.2013

Suki, B., & Stamenović, D. (2011). Lung Parenchymal Mechanics. In *Comprehensive Physiology*. Hoboken, NJ, USA: John Wiley & Sons, Inc. https://doi.org/10.1002/cphy.c100033

Sullivan, R. M., Ghosn, L. J., & Lerch, B. A. (2008). A general tetrakaidecahedron model for open-celled foams. *International Journal of Solids and Structures*, *45*(6), 1754–

1765. https://doi.org/10.1016/j.ijsolstr.2007.10.028

Suquet, P. M. (1987). Elements of Homogenization for Inelastic Solid Mechanics. In *Homogenization Techniques for Composite Media* (pp. 193–278). Berlin, Heidelberg: Springer Berlin Heidelberg. https://doi.org/10.1007/3-540-17616-0_15

Toshima, M., Ohtani, Y., & Ohtani, O. (2004). Three-dimensional architecture of elastin and collagen fiber networks in the human and rat lung. *Archives of Histology and Cytology*, *67*(1), 31–40. https://doi.org/10.1679/aohc.67.31

Tschumperlin, D. J., Boudreault, F., & Liu, F. (2010). Recent advances and new opportunities in lung mechanobiology. *Journal of Biomechanics*, *43*(1), 99–107. https://doi.org/10.1016/j.jbiomech.2009.09.015

Tsuda, A., Filipovic, N., Haberthür, D., Dickie, R., Matsui, Y., Stampanoni, M., & Schittny, J. C. (2008). Finite element 3D reconstruction of the pulmonary acinus imaged by synchrotron X-ray tomography. *Journal of Applied Physiology*, *105*(3), 964–976. https://doi.org/10.1152/japplphysiol.90546.2008

Vasilescu, D. M., Gao, Z., Saha, P. K., Yin, L., Wang, G., Haefeli-Bleuer, B., … Hoffman, E. A. (2012). Assessment of morphometry of pulmonary acini in mouse lungs by nondestructive imaging using multiscale microcomputed tomography. *Proceedings of the National Academy of Sciences*, *109*(42), 17105–17110. https://doi.org/10.1073/pnas.1215112109

Vasilescu, D. M., Klinge, C., Knudsen, L., Yin, L., Wang, G., Weibel, E. R., … Hoffman, E. a. (2013). Stereological assessment of mouse lung parenchyma via nondestructive, multiscale micro-CT imaging validated by light microscopic histology. *J Appl Physiol*, *114*(6), 716–24. https://doi.org/10.1152/japplphysiol.00855.2012

Vasilescu, D. M., Knudsen, L., Ochs, M., Weibel, E. R., & Hoffman, E. A. (2012). Optimized murine lung preparation for detailed structural evaluation via micro-computed tomography. *Journal of Applied Physiology*, *112*(1), 159–166. https://doi.org/10.1152/japplphysiol.00550.2011

Wall, W. A., Wiechert, L., Comerford, A., & Rausch, S. (2010). Towards a comprehensive computational model for the respiratory system. *International Journal for Numerical Methods in Biomedical Engineering*, *26*(7), 807–827. https://doi.org/10.1002/cnm.1378

Wang, Y., & Cuitiño, A. M. (2000). Three-dimensional nonlinear open-cell foams with large deformations. *Journal of the Mechanics and Physics of Solids*, *48*(5), 961–988. https://doi.org/10.1016/S0022-5096(99)00060-5

Warren, W. E., & Kraynik, A. M. (1991). The nonlinear elastic behavior of open-cell foams. *Journal of Applied Mechanics, Transactions ASME*, *58*(2), 376–381. https://doi.org/10.1115/1.2897196

Warren, W. E., & Kraynik, A. M. (1997). Linear elastic behavior of a low-density kelvin foam with open cells. *Journal of Applied Mechanics, Transactions ASME*, *64*(4), 787–794. https://doi.org/10.1115/1.2788983

Watz, H., Breithecker, A., Rau, W. S., & Kriete, A. (2005). Micro-CT of the Human Lung: Imaging of Alveoli and Virtual Endoscopy of an Alveolar Duct in a Normal Lung and in a Lung with Centrilobular Emphysema—Initial Observations. *Radiology*, *236*(3), 1053–1058. https://doi.org/10.1148/radiol.2363041142

Weibel, E. R. (1983). How does lung structure affect gas exchange? *Chest*, *83*(4), 657–665. https://doi.org/10.1378/chest.83.4.657

Weibel, E. R. (2017). Lung morphometry: the link between structure and function. *Cell and Tissue Research*, *367*(3), 413–426. https://doi.org/10.1007/s00441-016-2541-4

West, J. B. (2012). *Respiratory Physiology: The Essentials* (8th Editio). Alphen aan den Rijn, Netherlands: Wolters Kluwer.

West, J. B., & Matthews, F. L. (1972). Stresses, strains, and surface pressures in the lung caused by its weight. *Journal of Applied Physiology*, *32*(3), 332–345. https://doi.org/10.1152/jappl.1972.32.3.332

Wiechert, L., Comerford, A., Rausch, S., & Wall, W. A. (2011). Advanced Multi-scale Modelling of the Respiratory System. In *Fundamental Medical and Engineering Investigations on Protective Artificial Respiration* (pp. 1–32). https://doi.org/10.1007/978-3-642-20326-8_1

Wu, Y., & Perlman, C. E. (2012). In situ methods for assessing alveolar mechanics. *Journal of Applied Physiology*, *112*(3), 519–526. https://doi.org/10.1152/japplphysiol.01098.2011

Xu, X., Xu, S., Jin, L., & Song, E. (2011). Characteristic analysis of Otsu threshold and its applications. *Pattern Recognition Letters*, *32*(7), 956–961. https://doi.org/10.1016/j.patrec.2011.01.021

Yuan, H., Kononov, S., Cavalcante, F. S., Lutchen, K. R., Ingenito, E. P., & Suki, B. (2000). Effects of collagenase and elastase on the mechanical properties of lung tissue strips. *Journal of Applied Physiology (Bethesda, Md. : 1985)*, *89*(1), 3–14. https://doi.org/10.1114/1.28

Yuan, R., Nagao, T., Paré, P. D., Hogg, J. C., Sin, D. D., Elliott, M. W., … Coxson, H. O. (2010). Quantification of lung surface area using computed tomography. *Respiratory Research*, *11*, 1–9. https://doi.org/10.1186/1465-9921-11-153

Zeng, Y. J., Yager, D., & Fung, Y. C. (1987). Measurement of the mechanical properties of the human lung tissue. *Journal of Biomechanical Engineering*, *109*(2), 169–174. https://doi.org/10.1115/1.3138661

Zhang, T. (2008). A general constitutive relation for linear elastic foams. *International Journal of Mechanical Sciences*, *50*(6), 1123–1132. https://doi.org/10.1016/j.ijmecsci.2008.01.007

Zhang, Y. (2020). 2D/3D image segmentation toolbox. MathWorks Central File Exchange. Retrieved from https://www.mathworks.com/matlabcentral/fileexchange/24998-2d-3d-image-segmentation-toolbox

Zhu, H. X., Knott, J. F., & Mills, N. J. (1997). Analysis of the elastic properties of open-cell foams with tetrakaidecahedral cells. *Journal of the Mechanics and Physics of Solids*, *45*(3), 319–343. https://doi.org/10.1016/S0022-5096(96)00090-7

8. SUPPLEMENTARY MATERIAL

S 2-1 Kinematic and symmetry

Nodal coordinates used for the TKDr correspond to:

$$\boldsymbol{Y}_1 = \begin{bmatrix} 0 & \frac{1}{3} & \frac{2}{3} \end{bmatrix}^T \quad \boldsymbol{Y}_2 = \begin{bmatrix} \frac{1}{3} & 0 & \frac{2}{3} \end{bmatrix}^T \quad \boldsymbol{Y}_3 = \begin{bmatrix} \frac{2}{3} & 0 & \frac{1}{3} \end{bmatrix}^T \tag{A.1}$$

$$\boldsymbol{Y}_4 = \begin{bmatrix} \frac{2}{3} & \frac{1}{3} & 0 \end{bmatrix}^T \quad \boldsymbol{Y}_5 = \begin{bmatrix} \frac{1}{3} & \frac{2}{3} & 0 \end{bmatrix}^T \quad \boldsymbol{Y}_6 = \begin{bmatrix} 0 & \frac{2}{3} & \frac{1}{3} \end{bmatrix}^T \tag{A.2}$$

$$\boldsymbol{Y}_7 = \begin{bmatrix} 0 & \frac{1}{2} & \frac{5}{6} \end{bmatrix}^T \quad \boldsymbol{Y}_8 = \begin{bmatrix} \frac{-1}{6} & \frac{1}{6} & \frac{2}{3} \end{bmatrix}^T \quad \boldsymbol{Y}_9 = \begin{bmatrix} \frac{1}{6} & \frac{-1}{6} & \frac{2}{3} \end{bmatrix}^T \tag{A.3}$$

$$\boldsymbol{Y}_{10} = \begin{bmatrix} \frac{1}{2} & 0 & \frac{5}{6} \end{bmatrix}^T \quad \boldsymbol{Y}_{11} = \begin{bmatrix} \frac{2}{3} & \frac{-1}{6} & \frac{1}{6} \end{bmatrix}^T \quad \boldsymbol{Y}_{12} = \begin{bmatrix} \frac{5}{6} & 0 & \frac{1}{2} \end{bmatrix}^T \tag{A.4}$$

$$\boldsymbol{Y}_{13} = \begin{bmatrix} \frac{2}{3} & \frac{1}{6} & \frac{-1}{6} \end{bmatrix}^T \quad \boldsymbol{Y}_{14} = \begin{bmatrix} \frac{5}{6} & \frac{1}{2} & 0 \end{bmatrix}^T \quad \boldsymbol{Y}_{15} = \begin{bmatrix} \frac{1}{2} & \frac{5}{6} & 0 \end{bmatrix}^T \tag{A.5}$$

$$\boldsymbol{Y}_{16} = \begin{bmatrix} \frac{1}{6} & \frac{2}{3} & \frac{-1}{6} \end{bmatrix}^T \quad \boldsymbol{Y}_{17} = \begin{bmatrix} 0 & \frac{5}{6} & \frac{1}{2} \end{bmatrix}^T \quad \boldsymbol{Y}_{18} = \begin{bmatrix} \frac{-1}{6} & \frac{2}{3} & \frac{1}{6} \end{bmatrix}^T \tag{A.6}$$

With previous nodal coordinates, vectors used to represent the TKDr elements are listed below for the reference (left) and current (right) configuration

$$\boldsymbol{Q}_1 = \boldsymbol{Y}_2 - \boldsymbol{Y}_1 \qquad \boldsymbol{q}_1 = (\boldsymbol{Y}_2 + \boldsymbol{u}_2) - (\boldsymbol{Y}_1 + \boldsymbol{u}_1) \tag{A.7}$$

$$\boldsymbol{Q}_2 = \boldsymbol{Y}_3 - \boldsymbol{Y}_2 \qquad \boldsymbol{q}_2 = (\boldsymbol{Y}_3 + \boldsymbol{u}_3) - (\boldsymbol{Y}_2 + \boldsymbol{u}_2) \tag{A.8}$$

$$\boldsymbol{Q}_3 = \boldsymbol{Y}_4 - \boldsymbol{Y}_3 \qquad \boldsymbol{q}_3 = (\boldsymbol{Y}_4 + \boldsymbol{u}_4) - (\boldsymbol{Y}_3 + \boldsymbol{u}_3) \tag{A.9}$$

$$\boldsymbol{Q}_4 = \boldsymbol{Y}_5 - \boldsymbol{Y}_4 \qquad \boldsymbol{q}_4 = (\boldsymbol{Y}_5 + \boldsymbol{u}_5) - (\boldsymbol{Y}_4 + \boldsymbol{u}_4) \tag{A.10}$$

$$\boldsymbol{Q}_5 = \boldsymbol{Y}_6 - \boldsymbol{Y}_5 \qquad \boldsymbol{q}_5 = (\boldsymbol{Y}_6 + \boldsymbol{u}_6) - (\boldsymbol{Y}_5 + \boldsymbol{u}_5) \tag{A.11}$$

$$\boldsymbol{Q}_6 = \boldsymbol{Y}_1 - \boldsymbol{Y}_6 \qquad \boldsymbol{q}_6 = (\boldsymbol{Y}_1 + \boldsymbol{u}_1) - (\boldsymbol{Y}_6 + \boldsymbol{u}_6) \tag{A.12}$$

$$\boldsymbol{Q}_7 = \boldsymbol{Y}_7 - \boldsymbol{Y}_1 \qquad \boldsymbol{q}_7 = (\boldsymbol{Y}_7 + \boldsymbol{u}_7) - (\boldsymbol{Y}_1 + \boldsymbol{u}_1) \tag{A.13}$$

$$\boldsymbol{Q}_8 = \boldsymbol{Y}_8 - \boldsymbol{Y}_1 \qquad \boldsymbol{q}_8 = (\boldsymbol{Y}_8 + \boldsymbol{u}_8) - (\boldsymbol{Y}_1 + \boldsymbol{u}_1) \tag{A.14}$$

$$\boldsymbol{Q}_9 = \boldsymbol{Y}_9 - \boldsymbol{Y}_2 \qquad \boldsymbol{q}_9 = (\boldsymbol{Y}_9 + \boldsymbol{u}_9) - (\boldsymbol{Y}_2 + \boldsymbol{u}_2) \tag{A.15}$$

$$\boldsymbol{Q}_{10} = \boldsymbol{Y}_{10} - \boldsymbol{Y}_2 \qquad \boldsymbol{q}_{10} = (\boldsymbol{Y}_{10} + \boldsymbol{u}_{10}) - (\boldsymbol{Y}_2 + \boldsymbol{u}_2) \tag{A.16}$$

$$\boldsymbol{Q}_{11} = \boldsymbol{Y}_{11} - \boldsymbol{Y}_3 \qquad \boldsymbol{q}_{11} = (\boldsymbol{Y}_{11} + \boldsymbol{u}_{11}) - (\boldsymbol{Y}_3 + \boldsymbol{u}_3) \tag{A.17}$$

$$\boldsymbol{Q}_{12} = \boldsymbol{Y}_{12} - \boldsymbol{Y}_3 \qquad \boldsymbol{q}_{12} = (\boldsymbol{Y}_{12} + \boldsymbol{u}_{12}) - (\boldsymbol{Y}_3 + \boldsymbol{u}_3) \tag{A.18}$$

$$\boldsymbol{Q}_{13} = \boldsymbol{Y}_{13} - \boldsymbol{Y}_4 \qquad \boldsymbol{q}_{13} = (\boldsymbol{Y}_{13} + \boldsymbol{u}_{13}) - (\boldsymbol{Y}_4 + \boldsymbol{u}_4) \tag{A.19}$$

$$\boldsymbol{Q}_{14} = \boldsymbol{Y}_{14} - \boldsymbol{Y}_4 \qquad \boldsymbol{q}_{14} = (\boldsymbol{Y}_{14} + \boldsymbol{u}_{14}) - (\boldsymbol{Y}_4 + \boldsymbol{u}_4) \tag{A.20}$$

$$\boldsymbol{Q}_{15} = \boldsymbol{Y}_{15} - \boldsymbol{Y}_5 \qquad \boldsymbol{q}_{15} = (\boldsymbol{Y}_{15} + \boldsymbol{u}_{15}) - (\boldsymbol{Y}_5 + \boldsymbol{u}_5) \tag{A.21}$$

$$\boldsymbol{Q}_{16} = \boldsymbol{Y}_{16} - \boldsymbol{Y}_5 \qquad \boldsymbol{q}_{16} = (\boldsymbol{Y}_{16} + \boldsymbol{u}_{16}) - (\boldsymbol{Y}_5 + \boldsymbol{u}_5) \tag{A.22}$$

$$\boldsymbol{Q}_{17} = \boldsymbol{Y}_{17} - \boldsymbol{Y}_6 \qquad \boldsymbol{q}_{17} = (\boldsymbol{Y}_{17} + \boldsymbol{u}_{17}) - (\boldsymbol{Y}_6 + \boldsymbol{u}_6) \tag{A.23}$$

$$\boldsymbol{Q}_{18} = \boldsymbol{Y}_{18} - \boldsymbol{Y}_6 \qquad \boldsymbol{q}_{18} = (\boldsymbol{Y}_{18} + \boldsymbol{u}_{18}) - (\boldsymbol{Y}_6 + \boldsymbol{u}_6) \tag{A.24}$$

where $\boldsymbol{u}_i, i \in \{1 \dots 18\}$ are nodal displacements. To compute them, several kinematic relations can be formulated as previously explained and computed as detailed in the next. Axial symmetry of the TKD with respect to plane defined by X = 0 leads to the following assumptions about nodal displacements

$$u_{1x} = u_{6x} = 0 \tag{A.25}$$

$$u_{8x} = \frac{-u_{2x}}{2} \tag{A.26}$$

$$u_{9x} = \frac{u_{2x}}{2} \tag{A.27}$$

$$u_{10x} = \frac{u_{2x+}u_{3x}}{2} \tag{A.28}$$

$$u_{12x} = u_{3x} + \frac{u_{3x-}u_{2x}}{2} \tag{A.29}$$

Axial symmetry with respect to the plane defined by Y = 0 leads to

$$u_{2y} = u_{3y} = 0 \tag{A.30}$$

$$u_{8y} = \frac{u_{1y}}{2} \tag{A.31}$$

$$u_{9y} = \frac{-u_{1y}}{2} \tag{A.32}$$

$$u_{11y} = \frac{-u_{4y}}{2} \tag{A.33}$$

$$u_{13y} = \frac{u_{4y}}{2} \tag{A.34}$$

Finally, axial symmetry with respect to Z = 0 implies that

$$u_{4z} = u_{5z} = 0 \tag{A.35}$$

$$u_{10z} = u_{2z} + \frac{u_{2z} - u_{3z}}{2} \tag{A.36}$$

$$u_{11z} = \frac{u_{3z}}{2} \tag{A.37}$$

$$u_{12z} = \frac{u_{3z} + u_{2z}}{2} \tag{A.38}$$

$$u_{13z} = \frac{-u_{3z}}{2} \tag{A.39}$$

Furthermore, kinematic constraint about that nodes in rhomboid faces lie in a common plane implies that, for face with normal axis X,

$$u_{3x} = u_{4x} = u_{11x} = u_{13x} \tag{A.40}$$

For face with normal axis Y

$$u_{5y} = u_{6y} = u_{16y} = u_{18y} \tag{A.41}$$

And for face with normal axis Z,

$$u_{1z} = u_{2z} = u_{8z} = u_{9z} \tag{A.42}$$

Finally, since $\boldsymbol{F}^C$ is a principal deformation state, Dirichlet boundary conditions can be considered as constraints between certain degrees of freedom according to the following relations

$$\begin{aligned}
&\boldsymbol{u_7} = \boldsymbol{u}_{11+}(\boldsymbol{F}^C - I)\boldsymbol{b}_x \\
&\boldsymbol{u_{10}} = \boldsymbol{u}_{18+}(\boldsymbol{F}^C - I)\boldsymbol{b}_y \\
&\boldsymbol{u_{12}} = \boldsymbol{u}_{16+}(\boldsymbol{F}^C - I)\boldsymbol{b}_y \\
&\boldsymbol{u_{14}} = \boldsymbol{u}_{9+}(\boldsymbol{F}^C - I)\boldsymbol{b}_z \\
&\boldsymbol{u_{15}} = \boldsymbol{u}_{8+}(\boldsymbol{F}^C - I)\boldsymbol{b}_z \\
&\boldsymbol{u_{17}} = \boldsymbol{u}_{13+}(\boldsymbol{F}^C - I)\boldsymbol{b}_x
\end{aligned} \tag{A.43}$$

Thus, nodal displacements $\boldsymbol{u}_i, i \in \{1 \dots 18\}$ are given by the following expressions

$$u_1 = \left[0, \quad u_{1y}, \quad \frac{-2}{3}(1 - \lambda_3^C)\right]^T \tag{A.44}$$

$$u_2 = \left[u_{2x}, \quad 0, \quad \frac{-2}{3}(1-\lambda_3^C)\right]^T \tag{A.45}$$

$$u_3 = \left[\frac{-2}{3}(1-\lambda_1^C), \quad 0, \quad u_{3z}\right]^T \tag{A.46}$$

$$u_4 = \left[\frac{-2}{3}(1-\lambda_1^C), \quad -u_{1y} - \frac{2}{3}(1-\lambda_2^C), \quad 0\right]^T \tag{A.47}$$

$$u_5 = \left[-u_{2x} - \frac{2}{3}(1-\lambda_1^C), \quad \frac{-2}{3}(1-\lambda_2^C), \quad 0\right]^T \tag{A.48}$$

$$u_6 = \left[0, \quad \frac{-2}{3}(1-\lambda_2^C), \quad -u_{3z} - \frac{2}{3}(1-\lambda_3^C)\right]^T \tag{A.49}$$

$$u_7 = \left[0, \quad \frac{1}{2}u_{1y} - \frac{1}{3}(1-\lambda_2^C), \quad \frac{1}{2}u_{3Z} - \frac{2}{3}(1-\lambda_3^C)\right]^T \tag{A.50}$$

$$u_8 = \left[\frac{-1}{2}u_{2x}, \quad \frac{1}{2}u_{1y}, \quad \frac{-2}{3}(1-\lambda_3^C)\right]^T \tag{A.51}$$

$$u_9 = \left[\frac{1}{2}u_{2x}, \quad \frac{-1}{2}u_{1y}, \quad \frac{-2}{3}(1-\lambda_3^C)\right]^T \tag{A.52}$$

$$u_{10} = \left[\frac{1}{2}u_{2x} - \frac{1}{3}(1-\lambda_1^C), \quad 0, \quad \frac{-1}{2}u_{3Z} - (1-\lambda_3^C)\right]^T \tag{A.53}$$

$$u_{11} = \left[\frac{-2}{3}(1-\lambda_1^C), \quad \frac{1}{2}u_{1y} + \frac{1}{3}(1-\lambda_2^C), \quad \frac{1}{2}u_{3z}\right]^T \tag{A.54}$$

$$u_{12} = \left[\frac{-1}{2}u_{2x} - (1-\lambda_1^C), \quad 0, \quad \frac{1}{2}u_{3Z} - \frac{1}{3}(1-\lambda_3^C)\right]^T \tag{A.55}$$

$$u_{13} = \left[\frac{-2}{3}(1-\lambda_1^C), \quad \frac{-1}{2}u_{1y} - \frac{1}{3}(1-\lambda_2^C), \quad \frac{-1}{2}u_{3z}\right]^T \tag{A.56}$$

$$u_{14} = \left[\frac{1}{2}u_{2x} - \frac{2}{3}(1-\lambda_1^C), \quad \frac{-1}{2}u_{1y} - \frac{2}{3}(1-\lambda_2^C), \quad 0\right]^T \tag{A.57}$$

$$u_{15} = \left[\frac{-1}{2}u_{2x} - \frac{2}{3}(1-\lambda_1^C), \quad \frac{1}{2}u_{1y} - \frac{2}{3}(1-\lambda_2^C), \quad 0\right]^T \tag{A.58}$$

$$u_{16} = \left[\frac{-1}{2}u_{2x} - \frac{1}{3}(1-\lambda_1^C), \quad \frac{-2}{3}(1-\lambda_2^C), \quad \frac{1}{2}u_{3z} + \frac{1}{3}(1-\lambda_3^C)\right]^T \tag{A.59}$$

$$u_{17} = \left[0, \quad \frac{-1}{2}u_{1y} - (1-\lambda_2^C), \quad \frac{-1}{2}u_{3z} - \frac{2}{3}(1-\lambda_3^C)\right]^T \tag{A.60}$$

$$u_{18} = \left[\frac{1}{2}u_{2x} + \frac{1}{3}(1-\lambda_1^C), \quad \frac{-2}{3}(1-\lambda_2^C), \quad \frac{-1}{2}u_{3z} - \frac{1}{3}(1-\lambda_3^C)\right]^T \tag{A.61}$$

With previous expressions axial elastic potentials can be immediately computed. Nevertheless, for the case of the rotational potentials, it remains to know the pairs of struts that define the rotational springs deformation. For this purpose, vector $\mathcal{J}$ set pairs of strut used, according to:

$\mathcal{J}$ = { (1, 6); (1, 7); (1, 8); (7, 6); (7, 8); (8, 6); . . .
(2, 1); (2, 9); (2, 10); (9, 1); (9, 10); (10, 1); . . .
(3, 2); (3, 11); (3, 12); (11, 2); (11, 12); (12, 2); . . .
(4, 3); (4, 13); (4, 14); (13, 3); (13, 14); (14, 3);. . .
(5, 4); (5, 15); (5, 16); (15, 4); (15, 16); (16, 4);. . .
(6, 5); (6, 17); (6, 18); (17, 5); (17, 18); (18, 5) }

S 3-1 Table Sup. 3-1

Table Sup. 3-1. LAP group (p_{alv} = 10 cm H_2O): Statistics for porosity, normalized hydrostatic stress (5%, mode, mean, 95%), and normalized von Mises stress (5%, mode, mean, 95%).

RVE	**Porosity**	**Normalized Hydrostatic stress**				**Normalized Von Mises**			
		5%	**Mean**	**Mode**	**95%**	**5%**	**Mean**	**Mode**	**95%**
1	0.61	-1.19	0.81	1.17	3.32	1.09	4.09	2.48	9.39
2	0.63	-1.24	0.94	1.10	3.74	1.10	4.52	2.40	10.52
3	0.63	-1.39	1.11	1.08	4.39	1.32	5.19	3.69	12.06
4	0.62	-2.48	0.91	0.99	5.50	1.34	6.41	4.26	15.99
5	0.63	-1.29	1.03	0.90	4.01	1.21	4.84	3.24	10.85
6	0.67	-2.27	1.07	0.95	5.90	1.18	6.51	3.41	16.97
Mean	0.63	-1.64	0.98	1.03	4.48	1.21	5.26	3.25	12.63
Std.	0.02	0.57	0.11	0.10	1.02	0.11	1.00	0.71	3.12

S 3-2 Table Sup. 3-2

Table Sup. 3-2. HAP group (p_{alv} = 20 cm H_2O): Statistics for porosity, normalized hydrostatic stress (5%, mode, mean, 95%), and normalized von Mises stress (5%, mode, mean, 95%).

RVE	**Porosity**	**Normalized Hydrostatic stress**				**Normalized Von Mises**			
		5%	**Mean**	**Mode**	**95%**	**5%**	**Mean**	**Mode**	**95%**
1	0.71	-3.62	1.29	-0.96	8.59	0.82	8.96	6.49	24.90
2	0.71	-5.22	1.39	-0.92	10.59	1.46	12.13	5.38	38.33
3	0.71	-4.76	1.11	-0.89	9.05	1.11	10.89	5.15	32.04
4	0.71	-3.15	1.63	-0.92	8.62	1.49	9.21	5.27	24.46
5	0.69	-3.08	1.15	-0.96	7.23	0.98	8.19	5.18	22.88
6	0.70	-2.39	1.23	-0.94	6.47	1.02	7.41	5.28	18.68
Mean	0.70	-3.70	1.30	-0.93	8.43	1.15	9.47	5.46	26.88
Std.	0.01	1.08	0.19	0.03	1.44	0.27	1.75	0.51	7.08

S 3-3 Figure Sup. 3-1

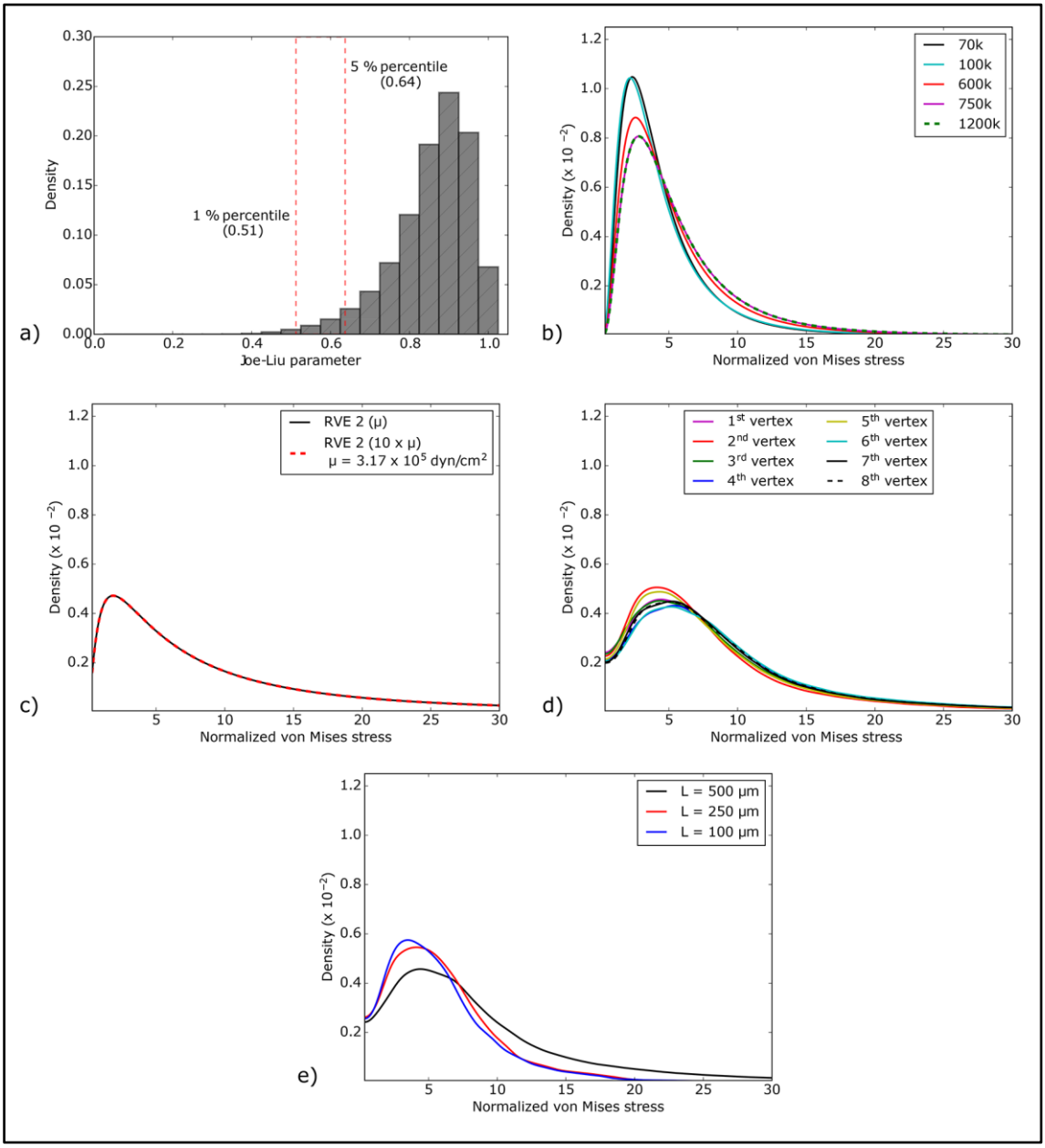

Figure Sup. 3-1. Convergence and sensitivity analyses: a) Mesh-quality analysis based on Joe-Liu parameter histogram, b) Mesh convergence analysis, c) Sensitivity of stress distribution to strong variations in the elastic modulus, d) Sensitivity of the stress distribution to changes in boundary conditions, e) Sensitivity of the stress distribution to RVE domain size.

S 3-4 Figure Sup. 3-2

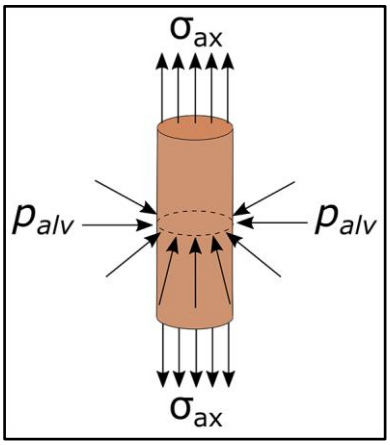

Figure Sup. 3-2. Idealization of alveolar wall under multiaxial stress state.

S 4-1 Figure Sup. 4-1

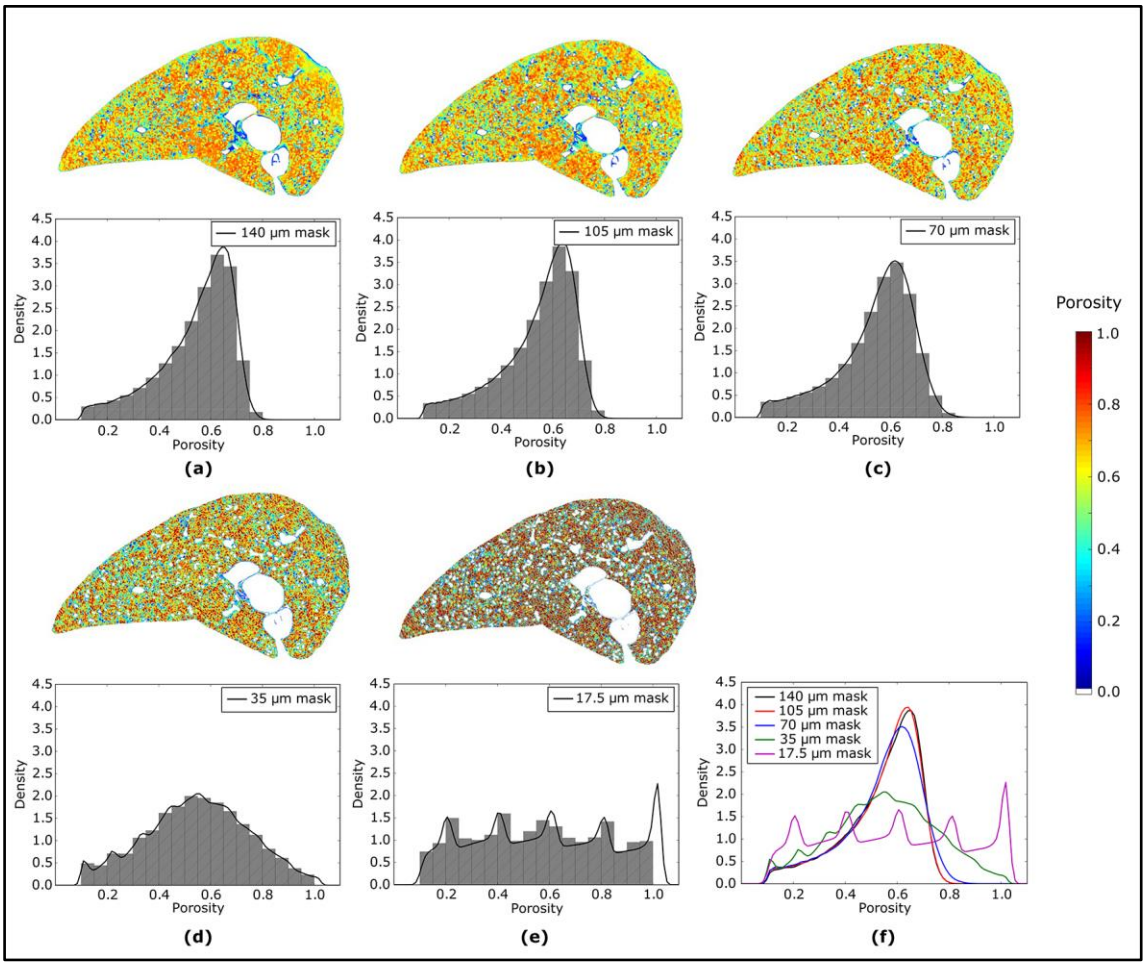

Figure Sup. 4-1. Sensitivity analysis of the mask size in the generation of porosity maps. Histograms for the medium zone of a representative subject from the MAF group were constructed from porosity maps that employed a mask size of (a) 140 µm, (b) 105 µm, (c) 70 µm, (d) 35 µm, and (e) 17.5 µm. Density functions fitted to histograms for all cases are shown in (f) for comparison purposes

S 4-2 Figure Sup. 4-2

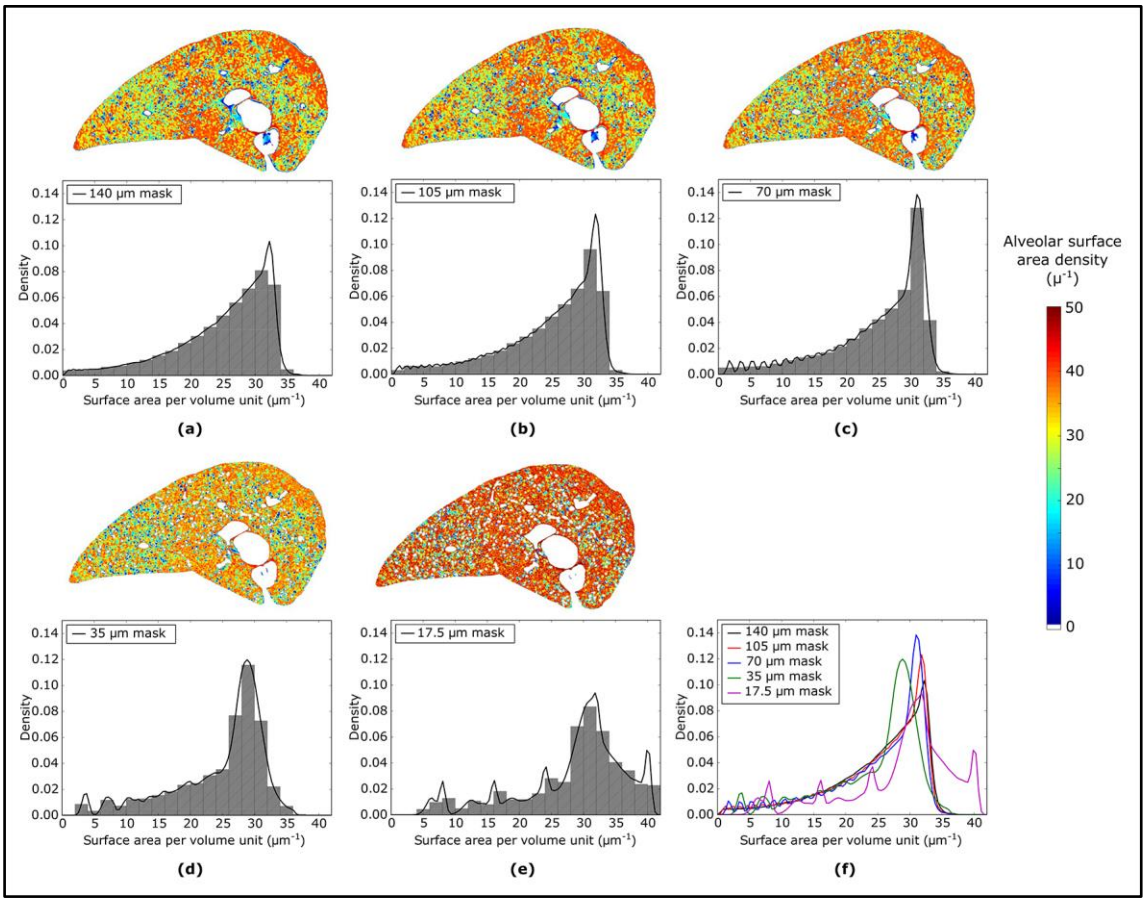

Figure Sup. 4-2. Sensitivity analysis of the mask size in the generation of alveolar surface area density maps. Histograms for the medium zone of a representative subject from the MAF group were constructed from alveolar surface area density maps that employed a mask size of (a) 140 µm, (b) 105 µm, (c) 70 µm, (d) 35 µm, and (e) 17.5 µm. Density functions fitted to histograms for all cases are shown in (f) for comparison purposes.